DEPARTAMENTO DE ASTROFISICA

Universidad de La Laguna

QUIJOTE-MFI: Optics Characterisation and Polarisation Measurements of CMB Foregrounds

Memoria que presenta
D. Riccardo Vignaga
para optar al grado de
Doctor en Ciencias Físicas.

Trabajo dirigido por el
Dr. Ricardo Génova Santos
Dr. Rafael Rebolo López

INSTITUTO Đ ASTROFISICA Đ CANARIAS
julio de 2018

Examination date: July 2018
Thesis supervisor: Ricardo Génova Santos, Rafael Rebolo López

ISBN: xx-xxx-xxxx-x
Depósito legal: TF-xxxx/2018

Abstract

The study of the Cosmic Microwave Background (CMB) anisotropies is one of the key tools of Modern Cosmology. The most important limitations of the experiments aimed at measuring both the intensity and the polarisation of the CMB are the systematics and the foregrounds, i.e. the Milky Way diffuse emission. This thesis will be devoted to the characterisation of these two aspects, with particular regard to the Multi-Frequency Instrument (MFI) of the QUIJOTE (Q-U-I JOint TEnerife) experiment.

The MFI consists of four horns that can measure intensity and polarisation between 10 and 20 GHz at angular resolutions between 40' and 57'. It has been operative almost continuously since November 2012, providing data of several calibrators, Galactic sources and extended fields for cosmological analyses. The first part of this thesis consists in the full characterisation of the optics of the MFI. The main beams are obtained through geostationary satellites observations and the results are confirmed with simulations and Cassiopeia A observations. We measure ellipticities > 0.92 and beam efficiencies > 0.90 in all horns. We estimate the level of the first sidelobe at -40 dB at 11 GHz, and the far sidelobes are found at a level of -70 dB, which is unprecedented for a microwave experiment. The Müller matrices formalism is used to analyse the polarisation response of the instrument. The main contaminant to CMB observation is the intensity-to-polarisation leakage, which is below 1% at 11 GHz in the MFI.

The major contaminants to the CMB polarisation are the synchrotron radiation and the dust emission of our Galaxy. The MFI is specifically designed to characterise the former type of emission, which is found mainly along the Galactic plane and in a region around the Galactic centre called Haze but can be found also at higher Galactic latitudes. In the second part of thesis we analyse ≈ 1300 hours of MFI data, covering four fields: W44, W49, W63 and the Haze. We produce the spectral energy distributions of 13 compact sources and adjust

them with physical parameters that model the synchrotron, free-free and thermal dust emission. Also, a phenomenological model is used for the anomalous microwave emission, which has been found in 11 sources. The diffuse emission is studied in the Haze region. We found that its main component is free-free at low Galactic latitudes and synchrotron at $b \approx 8^{\rm o}$. In polarisation, we measure a spectral index of -2.54 in temperature, which is in agreement with the Haze spectrum measured by Planck.

Resumen

El estudio de las anisotropías de la Radiación Cósmica de Microondas (RCM) es uno de las herramientas clave de la cosmología moderna. Las principales limitaciones en los experimentos dedicados a las medidas tanto de intensidad como de polarización de la RCM son los errores sistemáticos de la instrumentación y los contaminantes en el cielo, principalmente la emisión difusa de nuestra Galaxia. Esta tesis es dedicada a la caracterización de estos dos aspectos en relación con el Instrumento MultiFrequencia (MFI) del experimento QUIJOTE (Q-U-I JOint TEnerife).

El MFI consta de cuatro bocinas que miden intensidad y polarización entre 10 y 20 GHz con una resolución entre 40 y 57 minutos de arco. Está operativo desde noviembre de 2012 habiendo proporcionado datos de varios calibradores, fuentes Galácticas y campos extensos para análisis cosmológico. La primera parte de esta tesis consiste en la completa caracterización de los haces del MFI. Los haces principales son medidos a través de observaciones de satélites geoestacionarios, y los resultados son confirmados con simulaciones y observaciones de Cassiopeia A. Se han medido ellipticidades > 0.92 y eficiencias del haz > 0.90 en todas las bocinas. La estimación del nivel del primer lóbulo lateral es de -40 dB a 11 GHz, mientras los lóbulos laterales lejanos se encuentran a un nivel de -70 dB, lo cual no tiene antecedentes en experiementos de microondas. La respuesta en polarización del instrumento es estudiada con el formalismo de las matrices de Müller. El principal contaminante a las observaciones de la RCM es constituido por las pérdidas de intensidad a polarización, que están por debajo del 1% a 11 GHz en el MFI.

Los mayores contaminantes en polarización de la RCM son la radiación de sincrotrón y la emisión del polvo de nuestra Galaxia. El MFI está especialmente diseñado para caracterizar el primer tipo de radiación que, aunque se encuentra principalmente a lo largo del plano de la Galaxia y en una zona cercana al centro Galáctico llamada “Haze”, puede alcanzar latitudes Galácticas bastante

elevadas. En la segunda parte de esta tesis se analizan $\approx$ 1300 horas de datos del MFI, repartidos en cuatro campos: W44, W49, W63 y el Haze. Se producen las distribuciones espectrales de energia de 13 fuentes compactas y se ajustan con parámetros físicos que modelan la emisión de sincrotrón, de libre-libre y de polvo térmico. Un modelo fenomenológico es usado para la emisión anómala de microondas, que ha sido encontrada en 11 fuentes. La emisión difusa es estudiada en la región del Haze. Su componente principal es libre-libre a bajas latitudes Galácticas y sincrotrón a $b \approx 8^{o}$. En polarisación, se mide un índice espectral de -2.54 en temperatura, lo cual está en acuerdo con el espectro del Haze que midió Planck.

Contents

1

Introduction

1.1 The Hot Big Bang Model

The Hot Big Bang Model (HBB) is the most known and well-established theory to explain the beginning of the Universe. It was first introduced by George Gamow in 1946 (Gamow, 1946) as a mechanism to build up nuclei heavier than ^{1}H in the early Universe. In fact, in this model, the primordial nucleosynthesis[1] could happen only at temperatures of the order of $10^9 - 10^{10}$ K and it was already known that the Universe was expanding since Edwin Hubble's observations in the twenties of the last century[2]. Combining these two aspects, Gamow postulated that the Universe began in a very hot and dense state from which it expanded and cooled down. The first detailed calculations gave an estimated temperature for the radiation of about 5 K, which was discovered in 1964 (Penzias & Wilson, 1965). This diffuse radiation is now called Cosmic Microwave Background (CMB) and it is one of the three pillars of the HBB model, together with the expansion of the Universe and the cosmic abundances coming from the primordial nucleosynthesis. The CMB (see Section 1.2) is also an essential element of theoretical and observational cosmology. In fact, its statical properties provide information over the whole composition of the Universe, and in particular it is one of the main probes of the existence of dark energy. In addition, the polarisation of the CMB contains information on the gravitational waves produced during the inflation epoch (more details below).

Another key ingredient of the HBB model is the Cosmological Principle. It

[1] See subsection 1.1.2 for details.

[2] The first article which mentioned the expansion of the Universe was Hubble (1929).

states that the Universe is isotropic and homogeneous at large scales. Mathematically, it leads to the Robertson-Walker metric described in Eq. (1.1) in which the isotropy is evident for the use of spherical coordinates (r, θ, ϕ) and the expansion is factorized through the scale factor $a(t)$, so that the comoving coordinate r does not depend on it[3]. The parameter k is the curvature and can only adopt values +1,0,-1 in case of a close, flat or open Universe respectively.

$$ds^2 = c^2dt^2 - a^2(t)\left[\frac{dr^2}{1-kr^2} + r^2(d\theta^2 + \sin^2\theta d\phi^2)\right] \tag{1.1}$$

The evolution of the Universe is then described by the Einstein equation of General Relativity. When applied to the whole Universe with the assumption of the Cosmological Principle, this equation leads to the Friedmann equations:

$$H^2 \equiv \frac{\dot{a}^2}{a^2} = \frac{8\pi G\rho}{3} + \frac{\Lambda c^2}{3} - \frac{kc^2}{a^2} \tag{1.2}$$

$$\frac{\ddot{a}}{a} = -\frac{4\pi G}{3}\left(\rho + \frac{3p}{c^2}\right) + \frac{1}{3}\Lambda c^2 \tag{1.3}$$

where we introduced also the Cosmological Constant Λ, the total density ρ and pressure p. However, it is more common to use a scaled density $\Omega = \rho/\rho_{\text{critical}}$ where $\rho_{\text{critical}} = 3H/(8\pi G)$ is the matter density of a spatially-flat Universe. It is also useful to introduce another variable, the redshift z that is the change in wavelength of the radiation due to the Universe expansion: if the emitted wavelength is λ then we observe it at $\lambda' = a(t)\lambda$ and the change $z = (\lambda - \lambda')/\lambda = (1 - a(t))/a(t)$ so $a(t) = (1+z)^{-1}$. This way we have a direct relationship between time since the Big Bang and the observational quantity z.[4]

An illustrative picture of the first important happenings in the early Universe can be found in Fig. 1.1, but the most important will be explained here a little more into detail: Inflation, Primordial Nucleosynthesis and Recombination.

1.1.1 Inflation

Inflation is a very short period of time in which the Universe expanded exponentially. This period is the best explanation to three well known facts: the absence of magnetic monopoles, the flatness of the Universe and the horizon

[3]The real distance $d(t)$ from the centre of reference is given by $d(t) = a(t)r$, while r does not depend on time through the metric.

[4]Actually, since the $a(t)$ depends on the instant, we should have integrated along the light path to account for the different enlargements of the wavelengths.

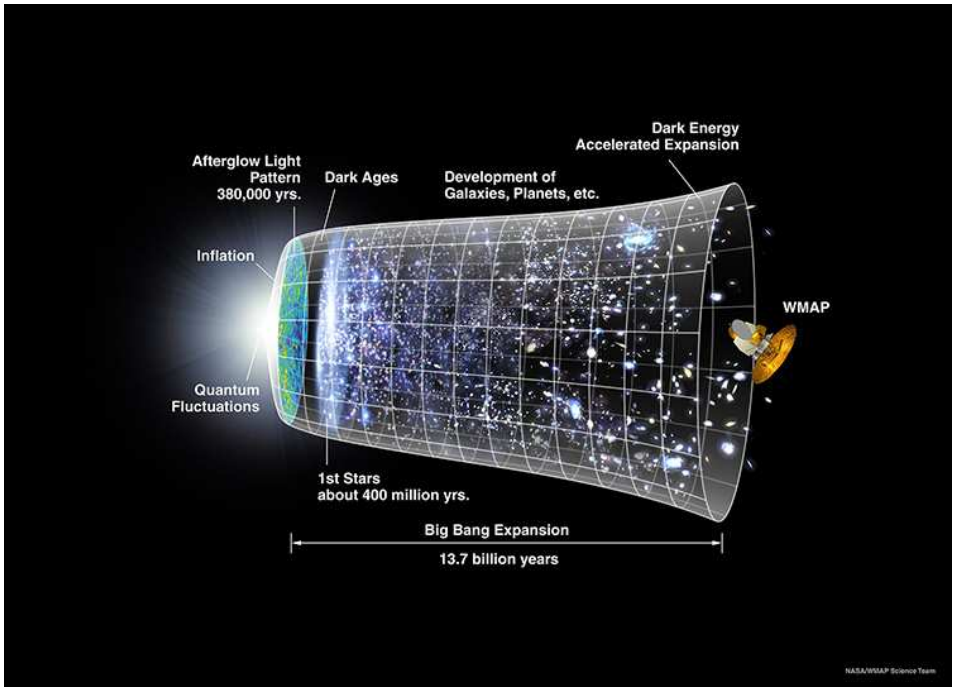

FIGURE 1.1— A representation of the evolution of the Universe. The size of the Universe, represented by the vertical axis, is represented against the time (horizontal axis). The "inflation epoch", a period of exponential growth of the Universe, is represented in the far left. The Cosmic Microwave Background is marked as "Afterglow Light Pattern" and was emitted about 380,000 years after inflation. Its radiation has traversed the Universe largely unimpeded since then, so that the initial conditions of the Universe are imprinted on this radiation and propagated until now. Credit: NASA / *WMAP* Science Team *http://wmap.gsfc.nasa.gov/media/060915/index.html*.

problem. The first is a well known fact so it will not be discussed it here, but, historically, this was the first problem solved with inflation (see Guth 1981, Linde 1982 and Albrecht & Steinhardt 1988 for details).

The second problem refers to the fact that if we measure the curvature of the Universe on large scales, it results to be always compatible with 0, that also means that the density of the Universe has to be very close to a particular value, named critical density, that is $\Omega_0 = \Omega_{\text{critical}} = 1$ (the subscript 0 means the actual value). The problem arises from the fact that if the initial value of Ω were slightly different from the critical value, it would diverge very rapidly at later epochs, but it is still very close to unity today. Therefore, we need a mechanism that guarantees a *fine-tuning* of the initial value of the total density to set it to unity in at least one part over 10^{60}.

The horizon problem is related with the fact that very far -very young- portions of the sky have similar properties. This poses a problem because, if information can be transmitted with the speed of light, such portions of Universe could not have exchanged neither energy nor matter, because the particle horizon goes as $r \approx ct$. For example, the CMB is generated at $z \approx 1100$, so we expect that regions at angular distances greater then 2^{o} could not have been in causal connection, but we measure their temperature to be equal[5] within one part over 10^5.

The theory of inflation is able to give an explanation for all these problems because that rapid expansion stretched the curvature away and permitted those portions of the Universe to be in contact without any conflict with General Relativity. Moreover it gives a very important bonus: it provides an explanation for the generation of primordial anisotropies.

1.1.2 Primordial Nucleosynthesis

After inflation, the Universe continued expanding and cooling. When temperature fell to an energy scale of 10^2 keV, a few minutes after the Big Bang, at a redshift of $z \approx 10^8 - 10^9$ and temperature of 10^9 K, nucleosynthesis, the period of light elements formation, started. With those temperatures and densities, radiation is rapidly thermalised to a perfect blackbody, thus fixing the number of photons to $n_\gamma \propto T^3$. Apart from annihilation processes, the ratio between the number of photons and baryons $\eta = n_\gamma / n_b$ remains constant. Now we estimate it to be of the order of $\approx 10^9$. Moreover, with thermal equilibrium, we can estimate the relative abundances of light elements because baryons follow a Maxwell-Boltzmann distribution. The relative abundances of all light elements have been predicted with this theory and observational data strongly agree with

[5] After the subtraction of the dipole, see Sect. 1.2.

it.

1.1.3 Recombination Epoch

With the word "recombination" we refer to the period in the Early Universe in which temperature is low enough that protons and electrons can combine to form atoms of hydrogen. However, the equilibrium in the reaction $e+p \rightarrow H+\gamma$ is not reached at the temperature of 13.6 eV (the ionisation temperature of hydrogen) but at a much lower temperature, since radiation dominates over recombination because there are many more photons than protons (recall $\eta = n_\gamma/n_b \approx 10^9$). From the Saha's equation (see for example Rubiño-Martin et al. 2009) we can find that the equilibrium is reached at a temperature of 0.26 eV (around 3000 K).

The observational importance of this period relies on the fact that before recombination the temperature is too high to have neutral atoms, so the electrons are free to interact with the photons and the Universe is opaque to electromagnetic radiation. However, after recombination there are no sufficient free electrons, thus the Universe became transparent to radiation. This phenomenon is known as the matter-radiation decoupling[6]. This means that all photons emitted just after this period are the oldest that can be observable now since the interactions with matter are much less than before recombination. This electromagnetic radiation that is "behind" all other sources is what we called Cosmic Microwave Background (CMB).

1.2 CMB Anisotropies and the Angular Power Spectrum

1.2.1 General Features

Because of the thermal equilibrium due to Thomson scattering before recombination, the CMB spectrum is expected to follow a black body and initial calculations gave an estimated temperature of 5 K in the present epoch. Observations confirmed that it is a perfect blackbody (deviations are measured to be of order of 0.003%) with an average temperature of 2.728±0.004 K(Fixsen et al., 1996). Therefore, we get immediately that the last scattering surface for CMB photons is at redshift $z \approx 1100$ because $(1+z) = T_{\text{emitted}}/T_{\text{observed}}$.

Moreover, there is a measured anisotropy with an amplitude of 3.4 mK on large scales with a dipole shape, due to the motion of the Solar System with respect to the CMB rest frame. Other spatial anisotropies are found to have an amplitude of the order of the tens of μK (one part in 10^5), thus confirming

[6] Actually, the interactions between photons and electrons restarted during the reionisation epoch, but at a much lower rate.

the need of inflation to resolve the horizon problem discussed above. Figure 1.2 shows a full-sky map of the CMB with and without subtraction of the monopole and of the dipole, as observed by COBE in 1992. These small anisotropies are of fundamental importance for cosmology. For example, they allow us to measure the cosmological parameters and to choose between or to discard different models of the Universe.

1.2.2 The Angular Power Spectrum of the CMB Anisotropies

The standard formalism used to analyse the CMB consists of the two-point correlation function and its Fourier transformation, the angular power spectrum. For temperature-only maps, this formalism is quite simple because the temperature field is scalar[7]. The deviation from the mean temperature, T_0, is $\Delta T(\hat{n}) = T(\hat{n}) - T_0$ and is usually expanded in the spherical harmonics basis, as

$$\frac{\Delta T}{T_0}(\hat{n}, \vec{x}) = \sum_{l=1}^{\infty} \sum_{m=-l}^{l} a_{lm}(\vec{x}) Y_{lm}(\hat{n}) \tag{1.4}$$

where $\hat{n}$ is the line of sight, $\vec{x}$ the position of the observer and Y_{lm} the spherical harmonics with the condition $|m| \leq l$ where $l \in \mathbb{N}$. We note that in this decomposition large l corresponds to small angular scales. An approximate relation is $\theta \approx \frac{180^{\circ}}{l}$ as one can find in Rubiño-Martin (2002) and references therein.

The cosmological principle states that the Universe is homogeneous and isotropic at large scales. This implies that the ensemble average of the a_{lm} is zero. If we assume Gaussian initial conditions[8], we can define the angular power spectrum C_l as

$$\langle a^*_{lm} a_{l'm'} \rangle = C_l \delta_{ll'} \delta_{mm'} \tag{1.5}$$

where the quantities C_l do not depend on m because of statistical isotropy. If we want to go back to real space, we obtain the equation

$$C(\theta) = \langle \frac{\Delta T}{T_0}(\hat{n}_1) \frac{\Delta T}{T_0}(\hat{n}_2) \rangle = \sum_l \frac{2l+1}{4\pi} C_l P_l(\cos\theta) \tag{1.6}$$

where $C(\theta)$ is the two point correlation function between all the lines of sight $\hat{n}_1$ and $\hat{n}_2$, separated an angular distance θ, ΔT is the deviation of the temperature from the average T_0, $\langle\rangle$ denotes an ensemble average, C_l are the coefficients of the angular power spectrum and P_l are the Legendre polynomials. When we

[7] We will see how this changes for other quantities

[8] This is predicted by many models and allows to limit the study in the real space to only the 2-point correlation function.

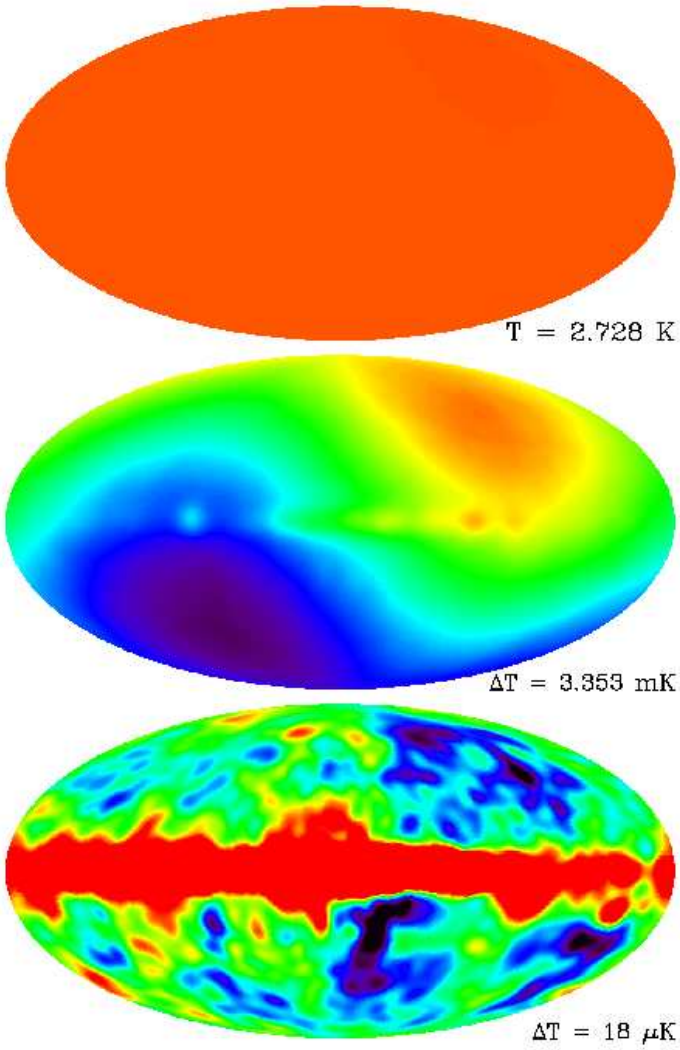

FIGURE 1.2— Full sky CMB maps obtained by the COBE satellite (Mather et al., 1990) for different dynamic ranges. The top panel represents the monopole, with a temperature T=2.728 K (Fixsen et al., 1996). The central panel is the map after subtraction of the monopole. Only the dipole pattern (with a temperature difference $\Delta T = 3.4\,\mathrm{mK}$) and a few Galactic structures are recognisable. In the bottom panel the dipole has been subtracted and the other anisotropies and the Galactic plane are visible. The amplitude of these anisotropy is of the order of $18\,\mu\mathrm{K}$. Credit: *https://lambda.gsfc.nasa.gov/product/cobe/cobe_images/m_d_53s_1111.gif.*

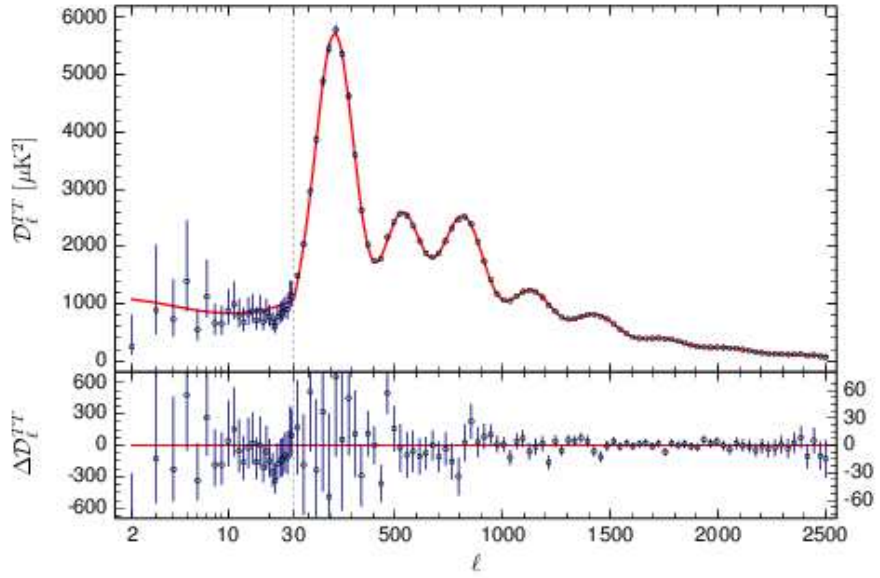

FIGURE 1.3— CMB temperature angular power spectrum derived from Planck 2015 data Planck Collaboration et al. (2016c). The acoustic peaks are clearly visible. The scatter at low multipoles is due to cosmic variance (see section 1.2.3). The red curve is the best-fit ΛCDM model. The bottom panel shows the residuals. The grey line at $l = 30$ marks the two different approaches used by the Planck collaboration to compute the angular power spectrum.

plot the C_l, we usually represent the quantity $TT \equiv \frac{l(l+1)C_l}{2\pi}$ instead[9], in order to highlight the features of the spectrum at $l > 100$ (the C_l depend on l as $C_l \approx \frac{1}{l(l+1)}$ at first order, thus the tail of the spectrum is flattened to the l axis, while the tail of the TT is not).

Fig. 1.3 shows the angular power spectrum measured with the Planck satellite and the best fit with a ΛCDM model. The peaks, usually called acoustic peaks, are due to harmonic oscillations that occurred when radiation and matter were in equilibrium. In fact, matter tends to collapse due to its own gravitational attraction, but this effect is compensated by radiation pressure, leading to oscillations of the matter-radiation fluid similar to what happens in acoustic waves, hence the name.

1.2.3 Cosmic Variance

A typical estimator of the C_l is given by the last approximation in:

$$C_l \equiv \langle |a_{lm}|^2 \rangle = \langle |a_{lm}|^2 \rangle_{\text{spatial}} = \frac{\sum_m \langle |a_{lm}|^2 \rangle_{\text{spatial}}}{2l+1} \approx \frac{\sum_m |a_{lm}|^2}{2l+1} \tag{1.7}$$

in which we have used ergodicity in the first equality (implied by Gaussianity) and isotropy in the second one. Given that each of this C_l is obtained from squaring $2l+1$ independent Gaussian numbers, they will be distributed following a χ^2 distribution with $2l+1$ degrees of freedom. Therefore, the intrinsic variance for each mode ("cosmic variance") is given by

$$\text{Var}(C_l) = \frac{2C_l^2}{2l+1} \tag{1.8}$$

which is larger for low l. Another way to understand the cosmic variance is the following: when we measure the angular power spectrum, we have an intrinsic error due to the fact that we are observing only one *realisation* of the Universe, that is, only a particular configuration of the position of the anisotropies. However, our analysis does not take into account the position of those anisotropies, but only the number of anisotropies with a given size, thus the error associated to each size (each l) depends on the number of observed anisotropies of that size.

An additional way to compute the cosmic variance is with simulations, since we are not bound to a particular realisation but only to the initial power spectrum. Fig. 1.4 shows the power spectra of four realisations of a simulated power spectrum. While at high l the four curves are almost superimposed, they are

[9] In the Planck notation, this is called D_l^{TT}.

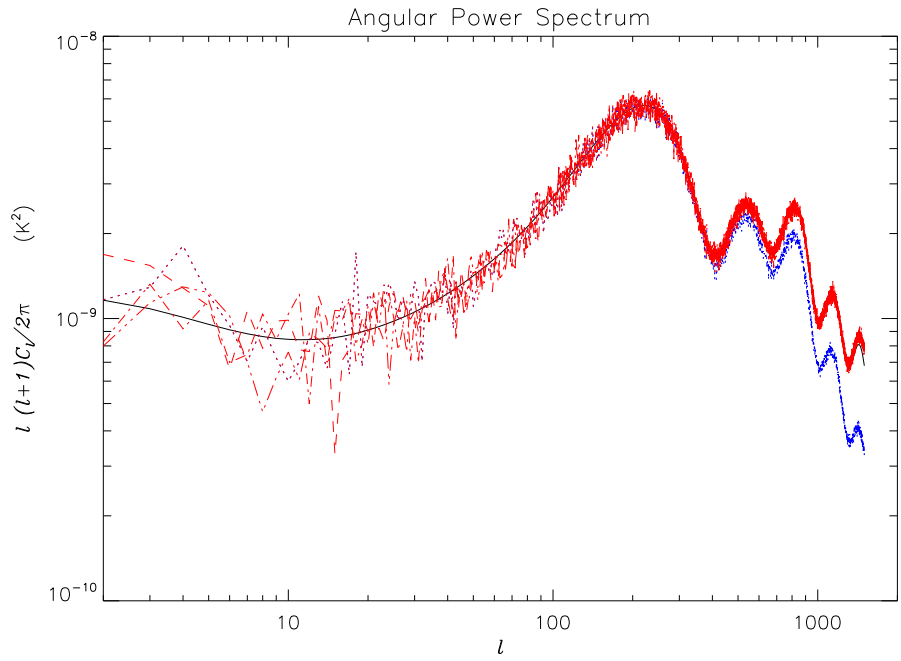

FIGURE 1.4— CMB power spectrum for standard cosmological values (black) and power spectra of four realisations of the CMB (red). Large differences are shown at low multipoles due to the cosmic variance. The effect of the beam of the observing telescope is not simulated. The effect of the pixelisation of the map is shown in the blue curve and affects only large multipoles. One can retrieve the unaffected power spectrum by dividing for the HEALPIx (Górski et al., 2005) window function (see the next subsection 1.2.4).

not at low l due to cosmic variance. We intentionally left one realisation uncorrected by the HEALPix (Górski et al., 2005) window function, which represents the effect of the pixelisation of the map over the angular power spectrum.

Finally, in the case of ground experiments, only a fraction of the sky is visible and large scales anisotropies (low l) cannot be measured.

1.2.4 Window Function

When we measure the temperature of the CMB in the sky we are selecting a set of angular scales to which the used instrument is sensitive. If $R(\hat{n}_1, \hat{n}_2)$ is the response of the experiment pointing toward $\hat{n}_2$ to a signal from $\hat{n}_1$, we have the following temperature

$$\frac{\Delta T_{\rm obs}}{T_0}(\hat{n}_2) = \int d\hat{n}_1 R(\hat{n}_1, \hat{n}_2) \frac{\Delta T}{T_0}(\hat{n}_1) \tag{1.9}$$

that is, the observed temperature pattern is the convolution of the real pattern with $R(\hat{n}_1, \hat{n}_2)$, that is also called "beam" or Point-Spread Function (PSF). With the definition (1.9) we can compute the power spectrum and obtain

$$\langle \frac{\Delta T_{\rm obs}}{T_0}(\hat{n}_1) \frac{\Delta T_{\rm obs}}{T_0}(\hat{n}_2) \rangle = \int d\hat{n}_1' \int d\hat{n}_2' R(\hat{n}_1, \hat{n}_1') R(\hat{n}_2, \hat{n}_2') \langle \frac{\Delta T}{T_0}(\hat{n}_1') \frac{\Delta T}{T_0}(\hat{n}_2') \rangle = \sum_l \frac{2l+1}{4\pi} C_l W_l P_l(\cos\theta) \quad (1.10)$$

where the W_l, if evaluated at $\hat{n}_1 = \hat{n}_2$, is what is commonly known as the window function. The simplest way to compute it is observing the response to a point source. In this thesis we use a Gaussian PSF, that is

$$R(\hat{n}_1, \hat{n}_2) = \exp\left(-\frac{1}{2}\frac{\theta^2}{\sigma^2}\right) \qquad \cos\theta = \hat{n}_1 \cdot \hat{n}_2 \quad (1.11)$$

where $\sigma = \theta_{\rm FWHM}/\sqrt{8\pi \ln 2}$ being $\theta_{\rm FWHM}$ the Full Width at Half Maximum of the beam of the experiment. The Gaussian approximation is typical for most experiments and will be verified in chapter 3. Moreover, it simplifies the calculations since the Fourier transform of a Gaussian is a Gaussian, thus we have a window function of the form $\mathrm{e}^{-\sigma^2 l(l+1)}$ and we can restore the original C_l by dividing by the same quantity, as shown in Fig. 1.5.

1.3 CMB Polarisation

As well as the intensity, the polarisation of the CMB is directly related to the Thompson scattering before and during recombination, since its cross-section depends on the scalar product between the incident and the scattered directions (Chandrasekhar, 1960). If the radiation field is isotropic, no net polarisation results since the orthogonal polarisation states balance completely. Conversely, if the incident radiation field has a quadrupolar variation in temperature, the scattered radiation will be linearly polarised (see Fig. 1.6). Thus, the observed polarisation depends on the existence of a quadrupole moment in the radiation field. However, if Thomson scattering is rapid, then the randomisation of photon directions destroys any quadrupole anisotropy and consequently the polarisation. Temperature perturbations have 3 geometrically distinct sources (Hu & White, 1997): the scalar (compressional), vector (vortical) and tensor (gravitational wave) perturbations that correspond to the three m associated to $l = 2$ (the quadrupole).

In particular, large scale polarisation is expected from the overall quadrupole ($l = 2$), which will have imprinted information from the inflationary epoch as it

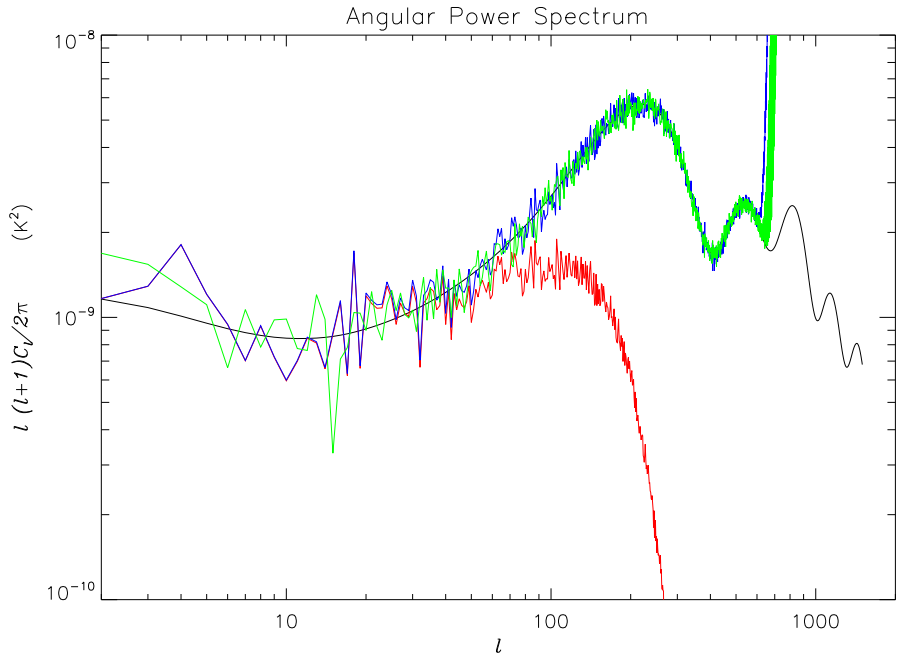

FIGURE 1.5— Simulation of a CMB power spectrum and some realisations with various random seeds and a 1°-beam. The red line that falls down at $l \approx 180$ is obtained without the beam correction (remember that $\theta \approx 180^\circ/l$). The blue and green lines are two realisations and the feature at $l \approx 800$ is due to the numerical precision of the computer. The black line is the original simulated power spectrum.

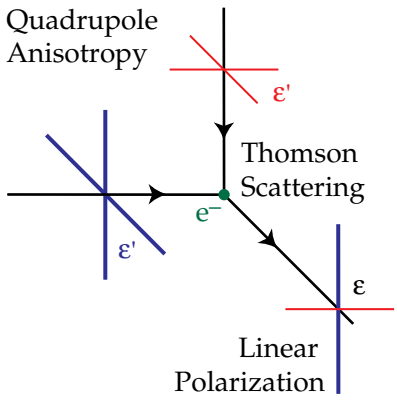

FIGURE 1.6— Thompson scattering: the two photons of different energy hit the electron from perpendicular directions. The result is a linearly polarised photon perpendicular to either of them. See text for details. Credit: Hu & White (1997).

occurs at scales larger than the causal horizon on the surface of last scattering. Also, if we separate the pure[10] polarisation fluctuations into a component with zero curl (E-modes, see below for a formal definition) and another one with non-zero curl (B-modes), it can be demonstrated that the latter can be produced only by tensor modes[11], which are the gravitational waves predicted by many inflationary scenarios. The detection of large-scale B-modes will be a definite probe of inflation and the amplitude of the B-modes will be directly related to the energy scale associated to inflation. For example, if we introduce the tensor-to-scalar ratio r, which is a measure of the relative power in the initial tensor perturbations compared to scalar perturbations, for many inflationary models we will have (Lyth, 1997):

$$r = 0.067\Big(\frac{V}{10^{16}\,\mathrm{GeV}}\Big)^4 \tag{1.12}$$

and a detection of r will give us the measure of the inflation potential V.

Apart from the B-modes, CMB polarisation data have been proven useful to measure the cosmological parameters, since some of the parameters fitted with the intensity power spectrum present degeneracies that we need to disentangle. For example, the relative amplitude of the E-modes to the intensity power spectrum at large angular scales gives an independent measure of the optical depth of reionisation, which is a degenerate parameter with the spectral index of scalar fluctuations (Rubiño-Martin et al., 2009). The first detection of the E-modes was achieved with the Degree Angular Scale Interferometer (DASI) in 2002 (Leitch et al., 2002).

1.3.1 Definition of the Stokes Parameters

Polarisation is a physical property of all transversal waves. The classical way of studying it is through the Stokes parameters. In fact, an electromagnetic monochromatic plane wave propagating in vacuum along the z-axis can be described by:

$$E_x(t) = E_1\cos(\omega t - \phi_1) = \mathrm{Re}(\epsilon_1 e^{-i\omega t}) \qquad E_y(t) = E_2\cos(\omega t - \phi_2) = \mathrm{Re}(\epsilon_2 e^{-i\omega t}) \tag{1.13}$$

[10] Since both intensity and polarisation come from the same physical process (the Thompson scattering of the photons by free electrons) we expect some correlation between intensity and polarisation, especially at low angular scales where the power spectrum is dominated by the acoustic peaks.

[11] Actually, there is an exception: the B-modes from lensing, but these occur only at smaller angular scales (see Fig. 1.7). Their first direct detection can be found in The Polarbear Collaboration: P. A. R. Ade et al. (2014).

where, for the sake of the simplicity, we used the two standard notations for the electromagnetic field: the first one with real amplitudes E_1, E_2 and real phases ϕ_1, ϕ_2, and the second one, with complex amplitudes ϵ_1, ϵ_2. The trajectory in the plane $z = 0$ is an ellipse and we can use the following combinations to parametrise it:

$$P_I = E_1^2 + E_2^2 = \epsilon_1^* \epsilon_1 + \epsilon_2^* \epsilon_2 \tag{1.14}$$

$$P_Q = E_1^2 - E_2^2 = \epsilon_1^* \epsilon_1 - \epsilon_2^* \epsilon_2 \tag{1.15}$$

$$P_U = 2E_1 E_2 \cos(\phi_1 - \phi_2) = \epsilon_1^* \epsilon_2 + \epsilon_2^* \epsilon_1 \tag{1.16}$$

$$P_V = 2E_1 E_2 \sin(\phi_1 - \phi_2) = i(\epsilon_1^* \epsilon_2 - \epsilon_2^* \epsilon_1) \tag{1.17}$$

With these parameters one can easily describe any kind of polarisation and the properties of the ellipse: for example linear polarisation is obtained by setting $P_V = 0$ and left-handed circular polarisation setting $P_V = -P_I$, $P_Q = P_U = 0$.

If the wave is not monochromatic, all the definitions stated above can be generalised taking the average over the statistical distribution of the wave-packets in the above equations. The condition

$$P_I^2 \geq P_Q^2 + P_U^2 + P_V^2 \tag{1.18}$$

is always true and the equal sign holds only for monochromatic and fully polarised beams.

However, the Stokes parameters are defined operatively. First, we have to choose a reference direction, possibly the x-axis of the electric field. Then we put a linear polariser along this axis and we measure the value of the intensity after the polariser, I_0. After that, we rotate the polariser in the counter-clockwise direction in steps of 45^o and we measure again the values. In this way we have the four measurements at angles of 45^o, 90^o and 135^o, thus obtaining I_{45}, I_{90}, I_{135}. Finally, the polariser is substituted by an ideal filter for right-handed circular polarisation and, afterwards, by one for left-handed polarisation obtaining the values I_R and I_L. This way, we have the operative definition of the Stokes parameters:

$$I = I_0 + I_{90} = I_{45} + I_{135} = I_R + I_L = kP_I \tag{1.19}$$

$$Q = I_0 - I_{90} = kP_Q \tag{1.20}$$

$$U = I_{45} - I_{135} = kP_U \tag{1.21}$$

$$V = I_R - I_L = kP_V \tag{1.22}$$

where k is an adimensional constant whose value is irrelevant for the determination of the parameters.

1.3.2 E and B modes

As we have just seen, the measurement of the Stokes parameters depends on the reference system in which we measure the intensity. If we rotate the reference system by an angle ϕ, the electric field transforms as

$$\begin{bmatrix} \epsilon_1' \\ \epsilon_2' \end{bmatrix} = \begin{pmatrix} \cos\phi & \sin\phi \\ -\sin\phi & \cos\phi \end{pmatrix} \begin{bmatrix} \epsilon_1 \\ \epsilon_2 \end{bmatrix} \tag{1.23}$$

and the corresponding Stokes parameters as

$$\begin{bmatrix} I' \\ Q' \\ U' \\ V' \end{bmatrix} = \begin{pmatrix} 1 & 0 & 0 & 0 \\ 0 & \cos 2\phi & -\sin 2\phi & 0 \\ 0 & \sin 2\phi & \cos 2\phi & 0 \\ 0 & 0 & 0 & 1 \end{pmatrix} \begin{bmatrix} I \\ Q \\ U \\ V \end{bmatrix} \tag{1.24}$$

A compact way to view the transformation of Q, U is

$$Q' \pm iU' = \mathrm{e}^{\pm 2i\phi}(Q \pm iU) \tag{1.25}$$

that is, the quantity $(Q \pm iU)$ transforms like spin-2 variables with a magnetic quantum number ± 2 under rotation along the $\hat{n}$ axis (Zaldarriaga & Seljak, 1997; Kamionkowski et al., 1997; Durrer, 2008). Therefore, we can make use of the spin weighted spherical harmonics ${}_sY_{lm}(\hat{n})$ defined as

$$\begin{aligned} {}_sY_{lm}(\hat{n}) = (-1)^m \sqrt{\frac{2l+1}{4\pi}\frac{(l+m)!(l-m)!}{(l+s)!(l-s)!}} (\sin\frac{\theta}{2})\mathrm{e}^{im\phi} \cdot \\ \sum_r \binom{l-s}{r} \binom{l+s}{r+s-m} (-1)^{l-r-s} (\cot\theta/2)^{2r+s-m} \end{aligned} \tag{1.26}$$

for each integer s with $|s| \leq l$ because they transform exactly as ${}_sY'_{lm}(\hat{n}) = \mathrm{e}^{\pm is\phi}$ ${}_sY_{lm}(\hat{n})$. We need to take into account two other aspects: the dimensionless Stokes parameters, simply given by renormalisation with the total intensity, and the elliptical basis, obtained setting

$$e^{\pm} = \frac{1}{\sqrt{2}}(e_\theta \pm ie_\phi) \tag{1.27}$$

where e_θ and e_ϕ are the canonical basis. Now, we can write:

$$(Q \pm iU)(\hat{n}) = \sum_{l=2}^{\infty} \sum_{m=-l}^{l} a_{lm}^{\pm 2} \, {}_{\pm 2}Y_{lm}(\hat{n}) = \sum_{l=2}^{\infty} \sum_{m=-l}^{l} (e_{lm} \pm ib_{lm}) \, {}_{\pm 2}Y_{lm}(\hat{n}) \tag{1.28}$$

where

$$e_{lm} = \frac{1}{2}(a_{lm}^{+2} + a_{lm}^{-2}) \qquad b_{lm} = \frac{-i}{2}(a_{lm}^{+2} - a_{lm}^{-2}) \tag{1.29}$$

From these, we can define the scalar quantities

$$E(\hat{n}) = \sum_{l=2}^{\infty} \sum_{m=-l}^{l} e_{lm} \, {}_{\pm 2}Y_{lm}(\hat{n}) \tag{1.30}$$

$$B(\hat{n}) = \sum_{l=2}^{\infty} \sum_{m=-l}^{l} b_{lm} \, {}_{\pm 2}Y_{lm}(\hat{n}) \tag{1.31}$$

or the rotationally invariant spectra

$$C_l^{EE} = \langle |e_{lm}|^2 \rangle \tag{1.32}$$

$$C_l^{BB} = \langle |b_{lm}|^2 \rangle \tag{1.33}$$

and also some mixed spectra, like $C_l^{TE} = \langle a_{lm}^* e_{lm} \rangle$.

Finally, we name TT, EE, BB, TE, TB, EB the spectra just defined multiplied by $\frac{l(l+1)}{2\pi}$. This removes the $\approx 1/l^2$ dependence and allows for a better visualisation. We note that, incidentally, parity imposes the last two, TB and EB, to be always zero.

There is no need to define a spectrum for the V Stokes parameter in this context because Thompson scattering does not produce circular polarisation, thus for purely CMB, $V = 0$.

The theoretical prediction for the non-zero power spectra are shown in Fig. 1.7, in which we separate the contribution from scalar-only (left panel) and tensor-only perturbations (right panel). The most interesting result for CMB science will be the detection of the large-scale B-modes, which cannot be produced by the scalar component of the perturbations. Therefore, it will be a direct proof of inflation, and its amplitude will constrain the inflationary models.

1.3.3 Observational Status

The current observational status of CMB polarisation remarkably differs between E-modes and B-modes. The formers have been detected since 2002 by the aforementioned DASI (Leitch et al., 2002), only two years after the detection of the first peak of the intensity power spectrum. After that, the measurement has been improved and the TE correlation power spectrum has also been detected. Fig. 1.8 shows one of the most recent measurements of the EE and TE power spectra as detected by the Planck satellite (Planck Collaboration et al., 2016c).

The detection of the primordial B modes has been more challenging due to their much lower amplitude and only upper limits have been put at the moment

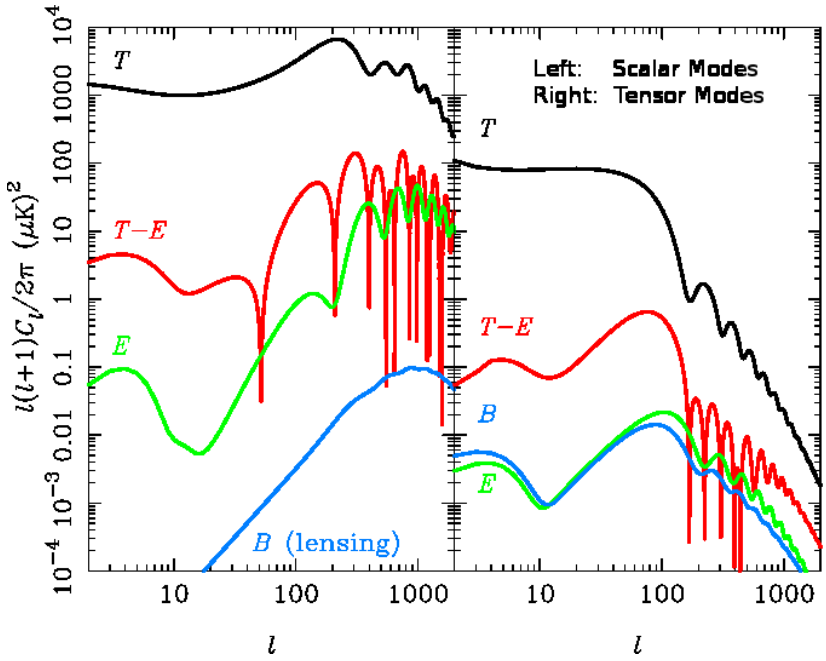

FIGURE 1.7— CMB angular power spectra predicted for purely scalar modes (left panel) and for purely tensor modes (right panel). The black line represents the temperature power spectra, or TT. The polarisation power spectra are represented in green (EE), blue (BB) and red (TE cross-correlation) for a model with $r = 0.24$. Scalar perturbations indirectly produce B-modes through weak gravitational lensing which are visible in the left panel at high l. The detection of primordial gravitational waves is equivalent to the detection at low l of the bump in the BB. Credit: Challinor (2013).

of writing of this thesis, although experiments aimed at their detection were designed since the beginning of the century. One of the first upper limits was put by DASI itself, followed by the results by CAPMAP, QUIET and BICEP. However, the first claim of a detection came in 2014 by BICEP2 (BICEP2 Collaboration et al., 2014), thanks to the advance in technology that allowed to fit 512 detectors in the same focal plane and the improvement in its sensitivity. However data from Planck showed that polarised emission from Galactic dust was responsible for the bulk of the measured polarisation and the detection of the primordial B-modes was finally rejected. Thus, the quest for the primordial B-modes detection is still open. Fig. 1.9 shows the observational status of the B-modes updated to 2016. At the moment of the writing of this thesis, the best constraint on r is $r < 0.12$ (95% CL), from the joint BICEP2/Keck/Planck collaboration (BICEP2/Keck Collaboration et al., 2015).

The current ground-based experiments can be grouped in two classes:

- Those aimed to detect the CMB polarisation at low frequency, between 10 and 50 GHz, with usually HEMT detectors at large angular scales
- Those focused on observations mainly at 150 GHz or above, use several hundreds of small bolometers that can be located in the same focal plane and can observe at smaller angular scales.

In fact, the best frequency for CMB polarisation observations is around 70 GHz in order to avoid Galactic contamination (see section 1.4), but it is impossible to achieve from the ground because of atmospheric contamination. The second class has given the best results until now due to the sensitivities achievable combining a very high number of detectors but it is limited by a good characterisation of the foregrounds and the lensing B-modes at high l (see Fig. 1.7). For this reason, almost all experiments after BICEP2 observe at several frequencies to properly estimate the contamination from the foregrounds and are located at high, very dry sites (Atacama desert, South Pole) to minimise the atmospheric contribution. Table 1.1 shows a summary of the active and some of the future CMB polarisation experiments.

In this thesis, we will consider data from the QUIJOTE experiment, located at the Teide Observatory, that belongs to the first class of experiments (10-50 GHz frequency range and 1 degree angular resolution).

1.4 External Contaminants to the CMB

When observing a region in the sky, not only we see the object of interest but also every emitting or absorbing object along the line of sight. In cosmology,

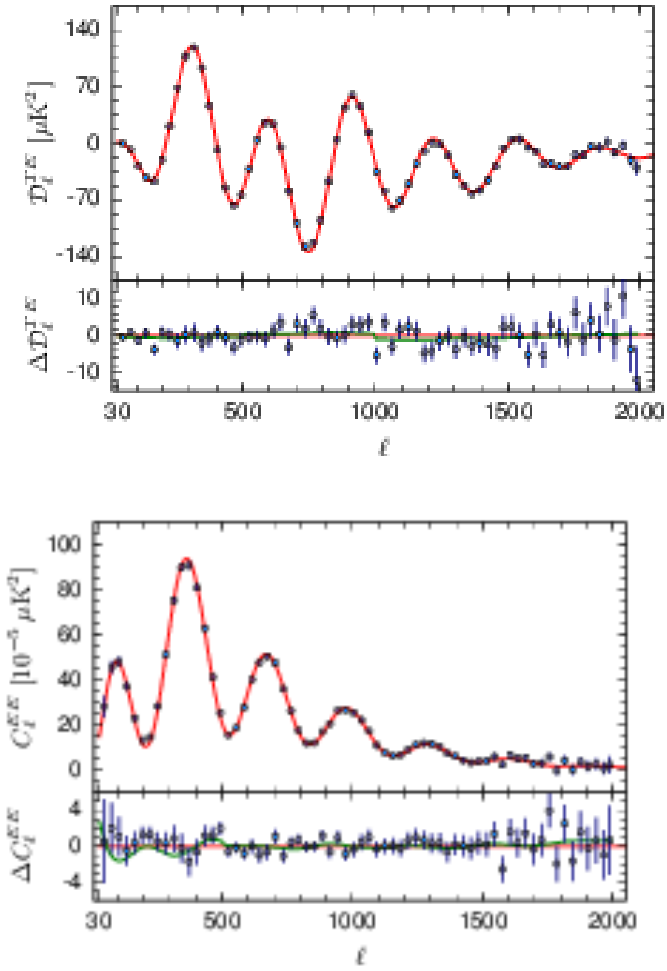

FIGURE 1.8— Planck measurements of the TE (top panel) and EE (bottom panel). The red curves represent the ΛCDM model. Credit: Planck Collaboration et al. (2016c).

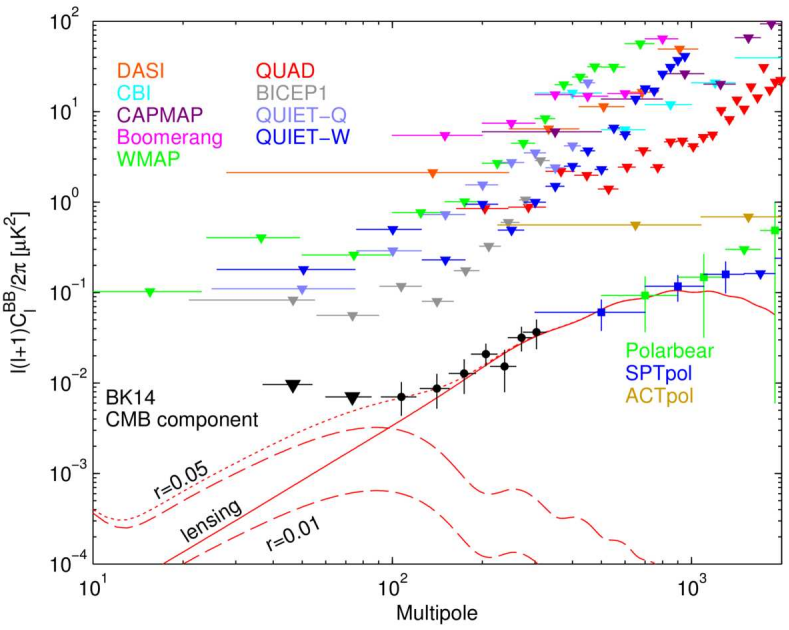

FIGURE 1.9— Observational status of the BB modes with existing data from BICEP II (BICEP2 Collaboration et al., 2016) and other CMB polarisation experiments: Leitch et al 2005 (DASI), Sievers et al 2007 (CBI), Bischoff et al 2008 (CAPMAP), Montroy et al 2006 (BOOMERANG), Bennett et al 2013 (WMAP), Brown et al 2009 (QUaD), Barkats et al 2014 (BICEP1), QUIET Collaboration 2011 (QUIET-Q), QUIET Collaboration 2012 (QUIET-W), POLARBEAR Collaboration 2014 (POLARBEAR), Keisler et al 2015 (SPTpol), Naess et al 2014 (ACTpol), Ade et al 2014 (BK14). The most stringent upper limits up-to-date are from BICEP2/Keck Collaboration et al. (2015) which give r is $r < 0.12$ (95% CL). Credits: BICEP2 Collaboration et al. (2016)

Name	Year	$l_{\min} - l_{\max}$	Frequency (GHz)	Detectors
POLARBEAR	2012	50-2000	150	Bolometer
Keck Array	2010	21-335	95,150,220	Bolometer
SPIDER	2015	10-300	90,150,280	Bolometer
ACTPol	2013	225-8725	90,146	Bolometer
SPTPol	2012	501-5000	95,150	Bolometer
QUIJOTE	2012	15-200	11,13,17,19,30,40	Polariser+OMT
COMPASS	2003	200-600	26-36	HEMT
MBI-B	Future	360-16000	90	Bolometer
BEAST	2000	10-1000	100,150	HEMT
EBEX	Future	25-1000	150-450	Bolometer
KUPID	2003	100-600	12-18	HEMT
ABS	2011	25-200	145	Bolometer
CLASS	2016	2-200	40,90,150,220	Bolometer
LiteBIRD	Future	2-200	60,78,100,140,195,280	Bolometer/MKID

TABLE 1.1— Summary of the active and future CMB polarisation experiments. All experiments are ground based, apart from BEAST and EBEX that are mounted on balloons and LiteBIRD, which is a satellite. Source: *https://lambda.gsfc.nasa.gov/product/expt/*.

since we are interested in the CMB, all other contributions are called "foregrounds". A first distinction is between the atmospheric contamination, the Galactic foregrounds and the extragalactic foregrounds.

1.4.1 Atmosphere

The atmospheric contribution is one of the strongest contaminants to CMB observations for ground-based experiments. In fact, observations are possible only through some frequency windows, as illustrated in Fig. 1.10.

In this work we are concerned with only radio telescopes, located at Teide observatory, thus the atmospheric contamination is quite low. More precisely, we used the ATM model by J. Pardo and J. Cernicharo[12] to determine the temperature of the atmosphere at our frequencies at an altitude of 2.4 km and an atmospheric pressure of 777 mbar (typical values at the Teide observatory). The median precipitable water vapour (PWV) at the Teide observatory is 3.7 mm, as measured by the GPS monitor of the AEMET[13] and confirmed with sky-dips observations (see section 2.3). Castro-Almazán et al. (2016) claims a lower value of 3.5 mm, but in any case both values are compatible with the median value

[12]The ATM code can be found at *http://cab.inta-csic.es/users/jrpardo/atm.html*. We refer to the references in the webpage for the detailed description of the model.

[13]Spain's National Meteorological Agency. This GPS monitor is located 1 km away from the Teide Observatory, at the same altitude. The data have been kindly provided by the director of the observatory, Dr. Emilio Cuevas.

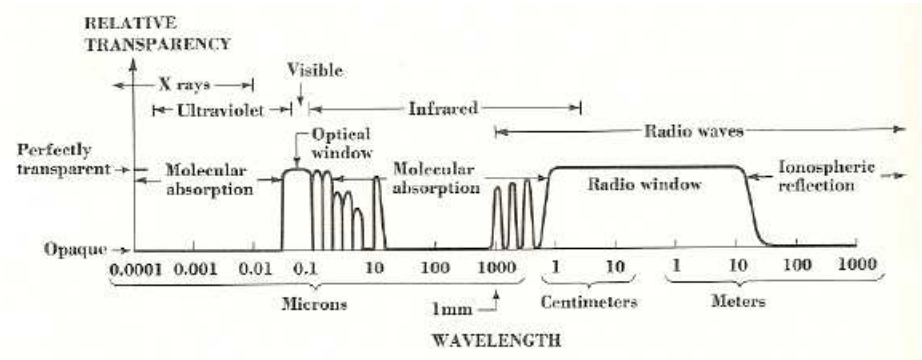

FIGURE 1.10— Transparency of the atmosphere as a function of wavelength. The two largest windows are in the radio and in the optical. Credit: Kraus (1966).

over the Roque de los Muchachos Observatory[14] of 3.8 mm (García-Lorenzo et al., 2010). The PWV changes quite considerably with the humidity and presents a seasonal variation. For this reason, we show the estimated temperature of the atmosphere for several PWV (from 1 mm in the lowest curve to 6 mm in the higher) in Fig. 1.11, where we also show the three frequency bands covered by the QUIJOTE instruments with colour bands. For the Multi-Frequency Instrument, the contribution to the temperature (at PWV=4 mm) varies from 1.8 K at 11 GHz to 4.2 K at 19 GHz, which is sufficiently smaller compared to the nominal system temperature of 25 K. The effect of the atmosphere in the data is mainly manifested as a higher system temperature, as it increases the thermal load of the instrument. Since the atmosphere emission is unpolarised[15], it affects the polarisation data only for the white noise component, without introducing any 1/f noise (see subsection 2.6.5).

1.4.2 Extragalactic Foregrounds

Almost all extragalactic sources are point sources for the aims of this thesis because of the great distance from which they are seen as compared with the beam size of the instrument[16]. Hence, they affect the study of the CMB mainly in the large l tail of the power spectrum in the form of a noise contribution (Battye et al., 2011). The standard method to remove this effect is through surveys and source catalogues aimed to detect all source with flux densities

[14]This observatory is located at almost the same altitude level of the Teide Observatory and usually presents similar meteorological conditions.

[15]Battistelli et al. (2012) puts upper limits on the polarisation fraction of 0.2% for circular polarisation and of 0.1% for linear polarisation.

[16]In this thesis the angular resolution of the data is 1 degree or is degraded to that.

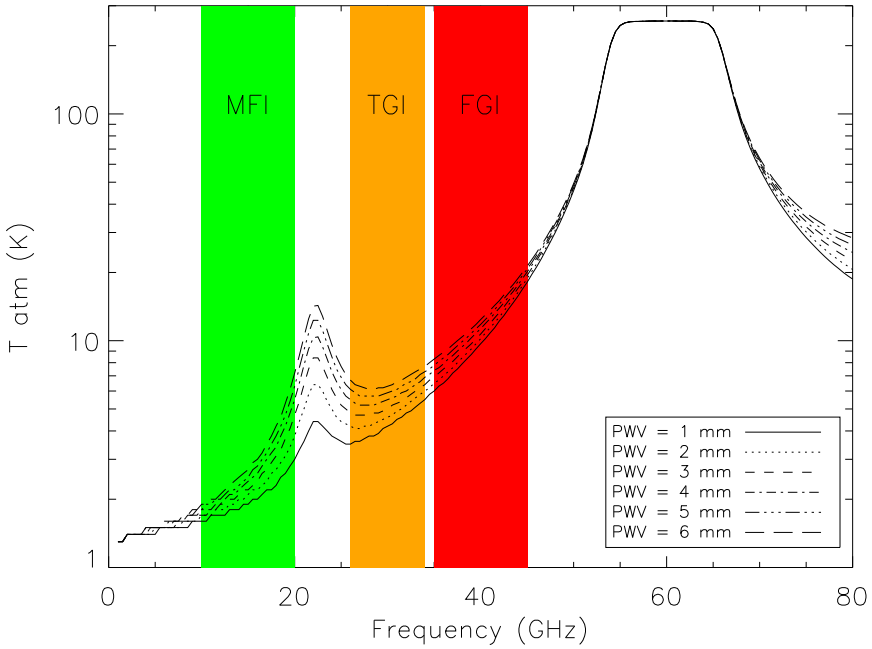

FIGURE 1.11— Atmospheric temperature as seen in radio frequencies for various values of the precipitable water vapour (from 1 mm in the lowest curve to 6 mm in the higher). The peak at 60 GHz is the estimated temperature of the atmosphere (the opacity is ≈ 1). We represent with colours the three frequency bands of the QUIJOTE instruments: green for the MFI, orange for the TGI and red for the FGI (see chapter 2).

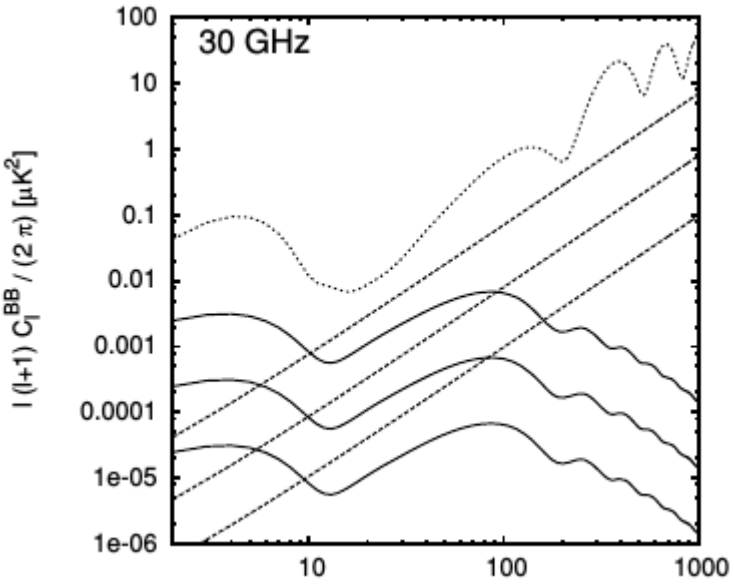

FIGURE 1.12— The projected noise spectrum at 30 GHz from a distribution of point sources below three different flux limits (1 Jy, 0.1 Jy, and 0.01 Jy) is plotted with straight dashed lines. A typical CMB EE spectrum is shown with the dotted line. The BB mode for $r = 0.1$, 0.01 and 0.001 are also plotted for comparison. Credit: Battye et al. (2011).

above a given threshold. The contribution to the power spectrum from all sources below 1 Jy at $l = 100$ is of the order of $10^{-1}\,\mu\mathrm{K}^2$ (see Fig. 1.12), which would allow the detection of the EE, but strongly hinder the detection of the B-modes for values of the tensor-to-scalar ratio below $r = 0.1$. QUIJOTE (the telescope used in this work) is focused on large angular scales and therefore will measure the power spectrum at low multipoles (typically between $l \approx 15$ and $l \approx 200$), where the contamination induced by point sources is not so critical. However, the maps produced with the QUIJOTE telescopes will be corrected with dedicated observations of point sources above ≈ 0.75 Jy with the Very Large Array.The interested reader can find more information in the already mentioned Battye et al. (2011) and in Tucci et al. (2004) or in Tucci & Toffolatti (2012).

1.4.3 Galactic Foregrounds

Galactic foregrounds are the main contaminants for radiocosmology. They are produced by different mechanisms, thus we proceed to classify the main processes that contribute to the continuum emission. The typical spectral depen-

dence of the continuum processes is shown in Fig. 1.13 for some of the brightest sources in the Sky. Fig. 1.14 shows the contribution of Galactic foregrounds to the RMS brightness temperature of the CMB maps from Planck. The estimation covers also the full frequency range of the QUIJOTE experiment. The detection of the B-modes is strongly limited by the contamination introduced by the polarised foregrounds. However, synchrotron emission is also important: Krachmalnicoff et al. (2016) estimated that the contamination from synchrotron emission cannot be neglected at frequencies below $\approx 100\,\mathrm{GHz}$ anywhere in the sky if $r \leq 0.03$.

Synchrotron

This is the main component of the radiation at low frequencies ($\nu \lesssim 10\,\mathrm{GHz}$), that is, at the frequencies of the QUIJOTE experiment considered in this work. It is due to relativistic electrons accelerated in a strong transversal magnetic field. It is the most important contribution to the radio continuum emission of the Galaxy and is the main emission mechanism for many types of point sources, like pulsars, quasars, radio-galaxies and supernova remnants. It is well traced by emission lines because free electrons are located in ionized regions like HII regions. The synchrotron spectrum follows a power law with exponent β typically between -1.4 and -0.5. In our Galaxy the mean value is -0.7 (Planck Collaboration et al., 2016b). This is due to the fact that the cosmic rays follow a power law energy distribution with exponent $\delta \approx -2.4$ and the corresponding synchrotron exponent is $\beta = \frac{\delta+1}{2}$. The synchrotron emission is highly polarised: the polarisation fraction in given in Rohlfs & Wilson (1996), Eq. (10.81), and ranges from 50% to 100% depending on the magnetic field and the angle of sight. Eq. (10.101) of the same book gives the polarisation fraction in terms of the exponent of the power law in case of a homogeneous magnetic field:

$$p = \frac{-\beta^{\mathrm{sync}} + 1}{-\beta^{\mathrm{sync}} + 5/3} \tag{1.34}$$

which gives for a typical value of $\beta^{\mathrm{sync}} = 0.75$ a polarisation of 72%. However, in reality the typical polarisation fractions are 10% or lower because of various mechanisms (incoherence in the magnetic field, Faraday depolarisation, superposition of different polarisation directions from different sources) that occur along the line of sight.

A different case of synchrotron emission is present in a Galactic region called "Haze", also known as "Fermi Bubbles" due to the γ-rays emission counterpart first revealed by data of the Fermi satellite. It is a huge region around the Galactic centre (Galactic coordinates $|l| < 15^{\mathrm{o}}$, $|b| < 50^{\mathrm{o}}$), which presents a

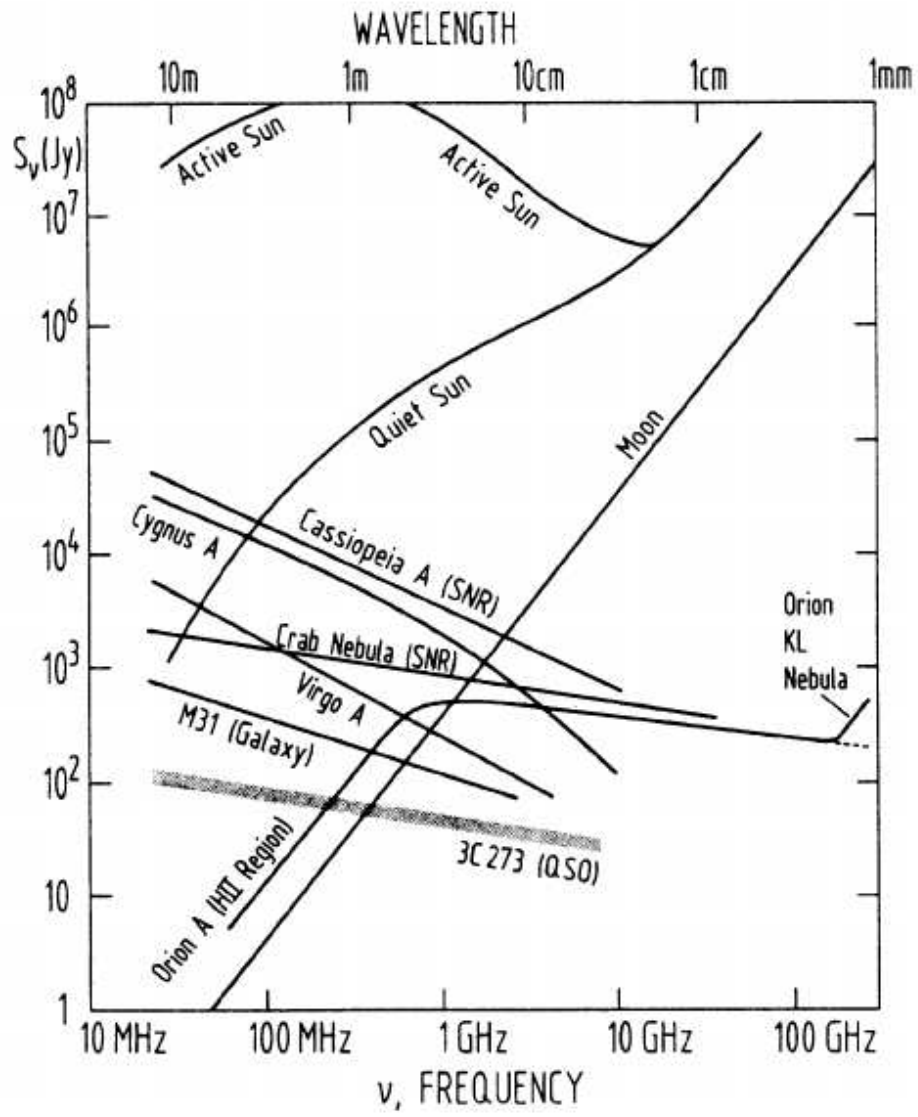

FIGURE 1.13— Spectra of some Galactic radiosources in the sky. Because of the Log scale of the graphic and the Rayleigh-Jeans approximation, the blackbody function results in a straight line ($B_\nu \approx \nu^2$) as for the Moon or the Sun when quiet. HII regions like Orion A typically present a change of the spectral dependence at $\nu \approx 1\,\mathrm{GHz}$. SuperNova Remnants (SNR) show a strong synchrotron emission. See text for more details. Credit: Rohlfs & Wilson (1996)

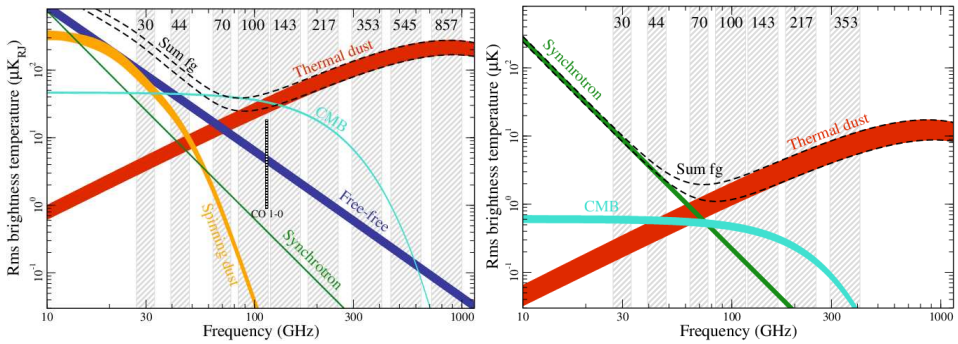

FIGURE 1.14— Brightness temperature RMS as a function of frequency and astrophysical component for temperature (left panel) and polarisation (right panel) in a typical clean region of the sky. The frequency coverage of the different Planck frequencies bands is indicated by vertical grey bars. At the QUIJOTE MFI frequencies the RMS is dominated by free-free emission in intensity and synchrotron emission in polarisation. Credit: Planck Collaboration et al. (2016a).

harder synchrotron spectrum. The interest of this region lies in the mechanisms that can explain the large amount of energy necessary to maintain such an energy distribution. QUIJOTE observations of this region will be discussed in section 5.6.2.

Free-Free Emission

The free-free emission is produced due to the thermal *bremsstrahlung* (braking radiation) arising from the interaction (without capture) between free electrons and ions. For this reason it is a good tracer of ionised regions. The free-free spectrum is characterised by a frequency dependence of ν^2 at low frequencies (below 0.1-1GHz) and of $\nu^{-0.15}$ at high frequencies. There is no net polarisation expected from this foreground since, although the free-free emission from a single electron is intrinsically polarised, the mean net polarisation of a population of electrons cancels out. However, edge effects from molecular clouds can produce a very small amount ($< 1\%$) of polarisation (Trujillo-Bueno et al., 2002).

Dust Emission

Dust particles are heated by the interstellar radiation field and re-emit this energy in the far infrared. There is evidence of two mechanisms: vibrational modes and rotational modes. The former is stronger and has a spectrum following a modified blackbody law: $T \approx B_\nu \nu^\beta \approx \nu^{\beta+2}$, where the factor ν^β accounts for opacity effects. Thus, this emission is typically observable at $\nu \geq 100\,\mathrm{GHz}$,

where it dominates over the other emission mechanisms. The average polarisation fraction of the dust is of a few percent, but it can be as high as 20% in small regions (Planck Collaboration et al., 2015).

Anomalous Microwave Emission

The Anomalous Microwave Emission (AME) is a radiation mechanism whose spectrum peaks between 10 and 50 GHz. One of the first detections was obtained in Watson et al. (2005) in the Perseus molecular could with the COSMOSOMAS experiment. The scenario that best explains it is the electric dipole emission from very small and rapidly rotating dust grains in the interstellar medium (Draine & Lazarian, 1999).

Small dust grains are likely to have a permanent electric dipole moment $\hat{\mu}$ due to the intrinsic dipole of molecules within the grain and uneven charge distribution. Interactions with the ambient gas and radiation field cause the grains to spin. Denoting by $\hat{\omega}$ their (vector) angular velocity, and assuming the grains to be spherical for simplicity (so they are not wobbling), Larmor's formula gives the power radiated by such a rotating dipole:

$$P(\omega) = \frac{2}{3}\frac{\ddot{\hat{\mu}}^2}{c^3} = \frac{2}{3}\frac{\omega^4 \mu_\perp^2}{c^3} \tag{1.35}$$

where $\mu_\perp$ is the component of $\hat{\mu}$ perpendicular to $\hat{\omega}$. This power is radiated at the rotation frequency, $\nu = \omega/(2\pi)$. In order to compute the emissivity due to this radiation process, one requires the probability distribution function $f(\omega)$ for the rotation rate ω, as well as the number density of dust grains. Both functions depend on the grain size, and so does the dipole moment μ. The distribution function $f(\omega)$ depends on the ambient gas temperature, density and ionization fraction and on the local radiation field. However, in observations the emission is usually modelled by a parabola in the logarithmic space characterised by its amplitude at the peak, its central frequency and its width (see Bonaldi et al. 2007).

Another scenario involves the magnetic dipole emission model, which predicts high polarisation fractions (up to 40 %) in the case of dust grains with atomic magnetic moments oriented in a single domain and much lower polarisation fractions for randomly-oriented magnetic moments. Thus, the study of AME polarisation is crucial to understand the emission mechanism. However, only upper limits[17] over individual sources have been set (López-Caraballo

[17] Although Battistelli et al. (2006) obtained a marginal detection of AME polarisation of $3.4^{+1.5}_{-1.9}$% at 11 GHz with the COSMOSOMAS experiment.

et al., 2011; Génova-Santos et al., 2015b). The best upper limit is from Génova-Santos et al. (2017) for the W43 region, which is 0.39% at 17 GHz and 0.22% at 41 GHz.

1.5 Motivation

As we have seen, the study of the CMB polarisation is of paramount importance for Cosmology, and it will eventually be the definitive probe of the Inflation epoch. From an observational point of view, the actual constraints on the characterisation of the polarisation power spectra and ultimately on the detection on the primordial B-modes are not technological but they reside in the correct estimation of the systematics of the experiment and in the foregrounds characterisation.

This thesis covers both of these aspects: the author actively participated in the commissioning phase of a new instrument, in its calibration and in the characterisation of the optics. While part of the process is published (Génova-Santos et al., 2015b), this will be the first document that gathers all the process and explains it in some detail available outside the QUIJOTE collaboration. A similar procedure for the optics characterisation will be used for the forthcoming QUIJOTE instruments.

Also, some of the data accumulated during the thesis are presented and used to characterise the foregrounds properties in different environments: HII regions, molecular clouds, supernova remnants (SNR) and in the diffuse Galactic emission, both in intensity and polarisation (when present). These regions have been chosen because they are an ideal laboratory to test our knowledge of the different foregrounds and their polarisation since, firstly, this analysis has to be done where the foregrounds are more intense. The same methodology can be later applied to the large blank regions used for cosmological studies (where the foreground contamination will be much lower) that are being observed at the moment of the writing of this thesis.

1.6 Objectives

This thesis was developed along with the exploitation of a new instrument at the Teide observatory: the Multi-Frequency Instrument (MFI), aimed at observing the Galactic foregrounds to correct the maps from forthcoming instruments, like the Thirty GigaHertz Instrument (TGI) or the Forty-GigaHertz Instrument (FGI), all three of them within the QUIJOTE collaboration. The objectives are (in chronological order):

1. To have a rapid characterisation of the global performance of the MFI

(commissioning phase).

2. To fully characterise the optics of the MFI in intensity. This is a crucial task for later cosmological observation, since the power spectrum measured by any experiment is affected by the response of the instrument (see subsection: 1.2.4).

3. To characterise the polarisation response of the MFI, with special emphasis on the intensity-to-polarisation leakage (the spurious polarisation signal coming from intensity) which is one of the most critical systematics in polarisation analysis.

4. To produce maps of most of the Galactic regions observed with the MFI.

5. To analyse those maps and to understand the spectral properties of the foregrounds, in order to estimate their contribution at higher frequencies.

6. To confirm the detection of the AME, particularly strong at the MFI frequencies (10-20 GHz).

7. To characterise the polarised emission of the Haze (see section 5.6.1), which is a huge Galactic region around the Galactic centre characterised by a hard synchrotron spectrum.

1.7 Outline

Chapter 2 presents the QUIJOTE experiment: the project, the telescopes and the instruments with special emphasis on the MFI, since only its data are used in this thesis. After that, the observing modes and the pipeline are described. Finally, the commissioning phase of this instrument and its calibration are presented.

Chapter 3 describes the optics characterisation of the MFI inside the first telescope. First, the calibration sources and the special map-making used for the analysis are presented. Also, the simulations used to compare the data are described. Then, the characterisation of the intensity beam is carried out: the main beams are modelled with elliptical Gaussian, the level of the sidelobes is estimated and the window functions are presented. Finally, a procedure to measure the polarisation response of the optics is presented and applied to one pixel of the MFI.

Chapter 4 presents the observations of the fields analysed in this thesis: W44, W49, W63 and the Haze. First, we present the observation strategy, then the criteria for the data selection and finally the maps. The last section of

the chapter presents the ancillary data used to complement QUIJOTE data at other frequencies.

Chapter 5 presents the analysis of the compact sources in these fields. The analysis includes the spectral energy distribution (SED) of two supernova remnants (W44 and W63), two HII regions (W43 and W47), one star forming region (W47) and a mixed morphology region (W51), in which two HII regions and one SNR fall inside the same MFI beam. The SED of the polarised sources (W44,W51,W63) are also presented and the rotation measure is retrieved. Then the Haze field is described and its diffuse emission is studied in regions of constant latitude through correlation plots, both in intensity and polarisation. Synchrotron emission has been found to be dominant outside the Galactic plane, while free-free emission dominates the disk.

Finally, the conclusions are presented in Chapter 6.

2

The QUIJOTE experiment

In this chapter we describe the QUIJOTE experiment: the scientific objectives, the telescopes and the instruments, with emphasis on the Multi-Frequency Instrument (MFI) on which the analyses presented in this work are based. Then we present the observing modes used in this thesis, and the advantages and disadvantages of each one. Also, the full pipeline of the MFI and its secondary products are presented with a final discussion on the map-making methods available for this work. A large section of this chapter is then dedicated to the commissioning process of the MFI and to its calibration. Finally, a very brief review of the observational status of the MFI is presented.

2.1 The QUIJOTE project

2.1.1 Scientific Goals

The QUIJOTE experiment (Q-U-I-JOint-TEnerife experiment) has two primary scientific goals:

1. to detect the B-modes imprinted in the CMB polarisation by primordial gravitational waves if they have an amplitude greater or equal to $r = 0.05$.

2. to provide essential information on the polarisation of the synchrotron and on the anomalous microwave emissions from our Galaxy at low frequencies (10-42 GHz).

To this aim, the QUIJOTE data will be used to characterise the polarisation of the CMB and other Galactic and extragalactic emission mechanisms in the frequency range 10-42 GHz, and at large angular scales. This will be achieved

through two polarisation surveys: one will cover an area of almost 20000 square degrees, with a sensitivity of $\approx 20\,\mu\mathrm{K/deg}^2$, and the other one will consist of deep observations of low contaminated regions in the sky, in order to achieve a sensitivity of $1\,\mu\mathrm{K/deg}^2$[1] in an area of ≈ 3000 square degrees. These measurements will be the most sensitive measurements ever obtained for the characterisation of the synchrotron and anomalous microwave emission (AME) in our Galaxy at those frequencies and will be used to correct their contamination in the QUIJOTE 30 and 40 GHz maps and in other CMB experiments. From this point of view, QUIJOTE is a good complement to the Planck experiment which observed at higher frequencies and can characterise the thermal dust polarisation emission.

The QUIJOTE experiment will also be dedicated to the study of several regions in the Milky Way. In particular, its observations have been of fundamental importance in measuring the uprise of the AME spectrum in the Perseus molecular complex (Génova-Santos et al., 2015b) and in the regions W43, W44 and W47 (Génova-Santos et al., 2017) and also in constraining their polarisation. Finally, another of the scientific objectives is the analysis of the spectral dependence and polarisation of the Haze region, in order to understand the mechanisms which rule this kind of emission.

2.1.2 Project Baseline

The QUIJOTE experiment consists of two telescopes and three instruments (see Fig. 2.1), and covers the frequency range 10-42 GHz with an angular resolution of $\approx 1^{\mathrm{o}}$, sited on the Teide Observatory (2400 m) in Tenerife (Spain). Experience over more than 30 years[2] with several CMB experiments (Tenerife Experiment, JBO-IAC Interferometer, COSMOSOMAS, Very Small Array) shows that this is an excellent place for CMB observations. The project is going through three phases:

1. *Phase I.* First QUIJOTE telescope (QT1) and the first instrument (MFI). This is a multichannel instrument providing the frequency coverage between 10 and 20 GHz that begun the commissioning phase in November 2012, right after the beginning of this thesis.

2. *Phase II.* Second QUIJOTE telescope (QT2) and the second instrument (TGI). It consists of 27 polarimeters working at 30 GHz. This telescope was commissioned during the summer of 2016.

[1] These are the sensibilities that will be achieved at 30 and 40 GHz. We expect to reach $5\,\mu\mathrm{K/deg}^2$ at lower frequencies.

[2] See *http://www.iac.es/proyecto/cmb/pages/en/former-cmb-experiments.php* for more information.

	MFI					TGI	FGI
Nominal Frequency [GHz]	11	13	17	19	30	30	40
Bandwidth [GHz]	2	2	2	2	8	8	10
Number of Horns	2	2	2	2	1	28	28
Channels per Horn	4	4	4	4	2	4	4
Beam FWHM [º]	0.92	0.92	0.60	0.60	0.37	0.37	0.28
$T_{\rm sys}$ [K]	25	25	25	25	35	35	45
NET $\left[\mu\text{K s}^{1/2}\right]$	280	280	280	280	390	50	50
Sensitivity $\left[\text{Jy s}^{1/2}\right]$	0.30	0.42	0.31	0.38	0.50	0.06	0.06

TABLE 2.1— Nominal characteristics of the three QUIJOTE instruments: the Multi-Frequency Instrument (MFI), the Thirty-GHz Instrument (TGI) and the Forty-GHz Instrument (FGI). Sensitivities are referred to Stokes Q and U parameters. The fifth horn of the MFI is actually a prototype of the TGI that was present in the laboratory phase but did not get into the telescope. See text for details.

3. *Phase III.* Third instrument (FGI) with 28 polarimeters working at 40 GHz. It will be fully or partly exchangeable with the TGI in the focal plane of the QT2. At the moment of writing this thesis, this instrument is being manufactured and tests are performed at the telescope with an instrument which in fact combines 14 detectors at both 30 and 40 GHz.

We refer to Rubiño-Martín et al. (2017) for the current status of the experiment and to Pérez-de-Taoro et al. (2014) for a technical overview. More information about the experiment can be found in Rubiño-Martín et al. (2012) and in Génova-Santos et al. (2015a).

Table 2.1 summarizes the basic (nominal) characteristics of these three instruments. The instantaneous noise equivalent temperature (NET) for one stabilized polarimeter horn is defined here as:

$$\text{NET} = \sqrt{2}\frac{T_{\rm sys}}{\sqrt{\Delta\nu N_{\rm channels}}} \tag{2.1}$$

where $T_{\rm sys}$ stands for the total system temperature, $\Delta\nu$ is the bandwidth and $N_{\rm channels}$ is the number of channels (computed here as the number of horns times the number of output channels per horn). From here, the noise is obtained as $\text{NET}/\sqrt{t}$, being t the integration time in seconds. We note that the system temperature ($T_{\rm sys}$) values quoted in Table 2.1 include the receiver contribution and the estimated contribution of the opto-mechanics. The spillover contribution (i.e., the background contribution when the instrument is placed in the focal plane of the telescope), the atmospheric contamination at the con-

sidered frequency and the CMB emission (2.728 K in Fixsen et al. 1996) have to be taken into account separately.

2.2 Telescopes and Instruments

2.2.1 Telescopes and Enclosure

The two telescopes of the QUIJOTE experiment are installed inside a single enclosure (see Fig. 2.1). The optics layout of both QT1 and QT2 telescopes is based on an alt-azimuthal mount supporting a primary (parabolic) and a secondary (hyperbolic) mirror arranged in an offset Gregorian Dracon scheme, which provides optimal cross-polarisation properties (designed to be less than -35 dB) and symmetric beams. Each primary mirror has a 2.25 m projected aperture, while the secondary has 1.89 m. The system is under-illuminated to minimize side-lobes and ground spillover. Each telescope is mounted on its own platform that can rotate around the vertical axis at a maximum frequency of 6 rotations per minute ($36^{o}s^{-1}$). The elevation limits of each telescope are 30^{o} and 95^{o}, thus the telescope can point at the zenith. The QT1 mirrors have been designed to operate up to 90 GHz (i.e., rms $\leq 20\,\mu$m and maximum deviation of $d = 100\mu$m). However, the QT2 has been specified to have a better surface accuracy, so the telescope could in principle operate up to 200 GHz. The centre of each secondary mirror has a hole designed to host a calibration diode. This is a small antenna kept at a constant temperature that emits periodically[3] circular polarised radiation. The installation of QT1 at the Teide Observatory took place during May 2012.

2.2.2 Multi-Frequency Instrument (MFI)

This is a multi-channel instrument with four independent sky pixels[4]: two operate in the frequency band 10-14 GHz and the other two in the frequency band 16-20 GHz. Its main science driver is the characterisation of the Galactic synchrotron emission, both in intensity and polarisation. These receivers were originally designed to perform simultaneous observations of the Stokes Q and U parameters with a continuous rotation of a polar modulator. A photograph of the MFI is shown in Fig. 2.2.

The optical arrangement includes five conical corrugated feedhorns (designed by the University of Manchester). Each horn feeds a novel cryogenic on-axis rotating polar modulator which can rotate at speeds of up to 1 Hz.

[3] The one in the MFI emits 20 pulses in one second every 31 s.

[4] A fifth pixel measuring at 30 GHz was used as a demonstrator of the second instrument during the laboratory tests, but was later removed to reduce the thermal load of the instrument.

FIGURE 2.1— The two QUIJOTE telescopes with the enclosure that protects them.

Two possible operational modes were considered: either continuous rotation of the polarimeters, or discrete changes of the positions of the motors in steps of 22.5º (note that the polar modulation occurs at four times the rotation angle). However, it was seen in the laboratory tests that each polar modulator has an average lifespan of 1000 rotations, thus the continuous rotation mode was restricted to a few tests and is not used in this thesis. On the other hand, the discrete rotation mode does not allow the simultaneous measurement of Q and U in each channel, which results in an overall reduced sensitivity.

The orthogonal linear polar signals are separated through a wide-band cryogenic Ortho-Mode-Transducer (OMT) before being amplified through two similar Low Noise Amplifiers (LNA). These two orthogonal signals are fed into a room-temperature Back-End module (BEM) where they are further amplified and spectrally filtered before being detected by square-law detectors. The band passes of the polarimeters have also been split into an upper and lower band which gives a total of eight channels per polarimeter (see Table 2.1). The Front-End Module (FEM) for the low frequency channels was built by the IAC. The receivers for these channels use Monolithic Microwave Integrated Circuit (MMIC) 6-20 GHz LNAs (designed by S. Weinreb and built in Caltech). The gain of these amplifiers is approximately 30 dB, and the noise temperature is typically around 9 K across the band. The cryogenics and the mechanical systems were provided by the IAC. The MFI scheme is illustrated in Fig. 2.3.

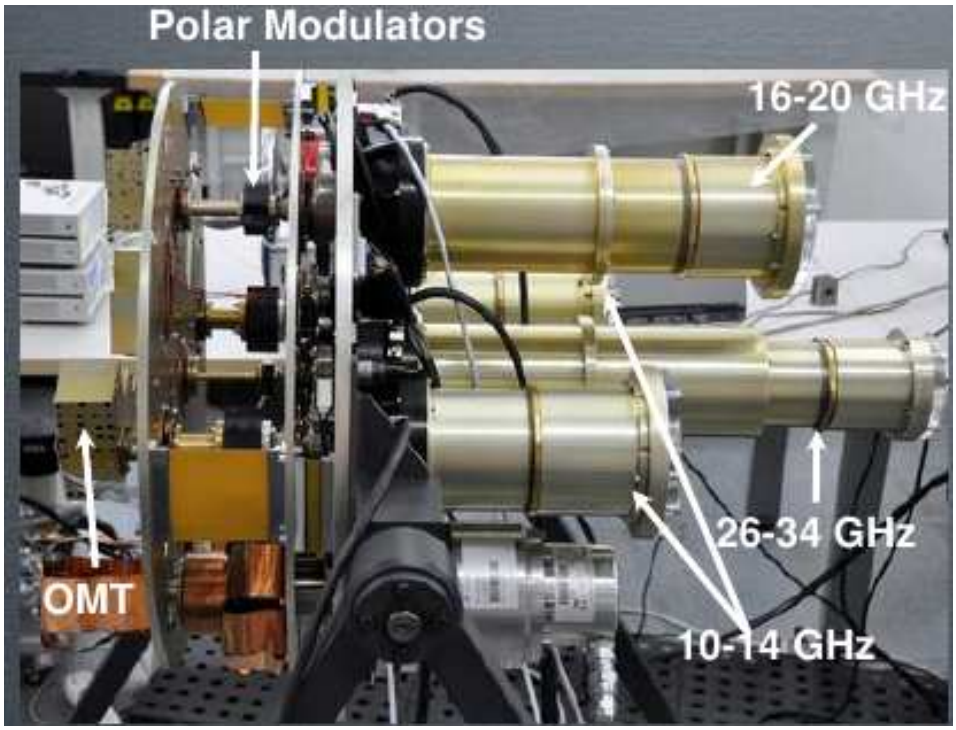

FIGURE 2.2— A photograph of the Multi-Frequency Instrument of the QUIJOTE experiment. The central horn at 30 GHz shown in the picture was removed in the current configuration to reduce the thermal load of the instrument.

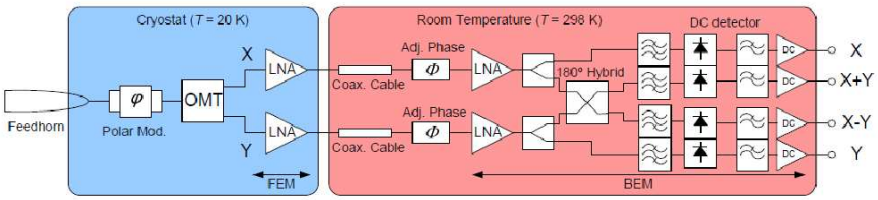

FIGURE 2.3— Detailed scheme of the MFI receiving system (first version). The incident radiation passes through a half-wave-plate rotator, an orthomode transducer (OMT), an amplifier and afterwards each channel is split into two, so we get four channels: two (X and Y) are directly detected and the other two are correlated through a 180° hybrid, thus they are called X+Y and X-Y.

The Stokes parameters can be obtained simultaneously with the continuous rotation, or each of them can be obtained from the difference between corresponding (correlated or uncorrelated, depending if they pass through the hybrid) in case of discrete rotation. The equations that give the responses of the MFI for the four outputs at each frequency are the following (López-Caraballo, 2013):

$$C_{\text{X+Y}} = \tfrac{1}{2}\big[I + Q\sin(4\theta) + U\cos(4\theta)\big] \tag{2.2}$$
$$C_{\text{X-Y}} = \tfrac{1}{2}\big[I - Q\sin(4\theta) - U\cos(4\theta)\big] \tag{2.3}$$
$$C_{\text{X}} = \tfrac{1}{2}\big[I + Q\cos(4\theta) - U\sin(4\theta)\big] \tag{2.4}$$
$$C_{\text{Y}} = \tfrac{1}{2}\big[I - Q\cos(4\theta) + U\sin(4\theta)\big] \tag{2.5}$$

where we introduced the theoretical Stokes parameters referred to the focal plane of the instrument and the angle of the position of the polar modulator θ referenced to its zero, that is calibrated afterwards with astronomical sources. The (X+Y) and (X-Y) channels are correlated through a 180º hybrid (see Fig. 2.3), thus are affected by the same 1/f noise. Hence, in their difference the 1/f noise cancels out and the polarisation data are much less affected. In this thesis, only correlated channels are used to retrieve polarisation data, and we will assume that the sky signal is constant on the time scales of our experiment. The 1/f noise in intensity is instead removed in the map-making process with a destriper code (see 2.5). The Stokes parameters (referred to the focal plane of the instrument) are then retrieved using only the $C_{\text{X-Y}}$ and $C_{\text{X-Y}}$, since:

$$I = C_{\text{X+Y}} + C_{\text{X-Y}} \qquad \forall\theta \tag{2.6}$$
$$Q = \pm(C_{\text{X+Y}} - C_{\text{X-Y}}) \qquad \text{for } \theta = 0^{\text{o}} \quad \text{or} \quad \theta = 45^{\text{o}} \tag{2.7}$$
$$U = \pm(C_{\text{X+Y}} - C_{\text{X-Y}}) \qquad \text{for } \theta = 22.5^{\text{o}} \quad \text{or} \quad \theta = 67.5^{\text{o}} \tag{2.8}$$

The low frequency maps (11-19 GHz) obtained with the MFI are to be used to correct the foregrounds contamination in the higher-frequency maps produced by the TGI and the FGI.

2.2.3 Modifications of the MFI

In April 2014, MFI observations were interrupted during 3 weeks for maintenance. The polar modulator of horn 1 had broken and we could not command its rotation by software, the amplifiers in horn 4 were of lower quality and had higher noise temperatures than those in other horns and we had detected the huge spillover from the satellites band through the far sidelobes of the telescope (see 3.4.4). The problem of Horn 4 was solved with the installation of two new

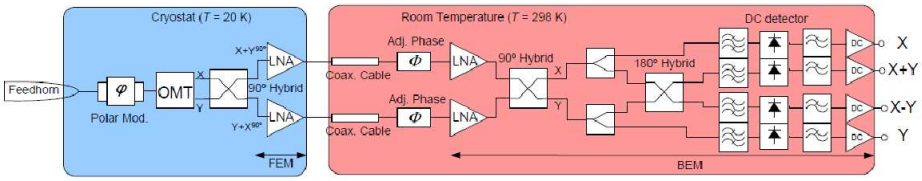

FIGURE 2.4— Scheme of the improved MFI receiving system. The difference with respect to the previous configuration shown in Fig. 2.3 is the presence of the two hybrids that are intended to correlate the outputs of the X and Y channels. See text for details.

amplifiers, while the installation of an extended shield over the QT1 solved the problem of the far sidelobes. However, the polar modulator of horn 1 could not be replaced, thus the engineering team opted for a new configuration of the receiver: since we could not move the modulator, the two correlated channels would always measure the same combination of the Stokes parameters Q and U, thus we could measure the perpendicular configuration with the uncorrelated channels. The major problem was the 1/f noise, which was removed in the subtraction of correlated channels. Hence, we introduced two 90º hybrids, one before the LNAs in the FEM and another one before the frequency splitters in the BEM (the new scheme of the "Improved" MFI is shown in Fig. 2.4) in order to have all the four channels correlated, allowing for the simultaneous detection of both Q and U without the contamination of 1/f noise.This new configuration was tested during the following year with horn 1, and has been finally applied to the other horns in December 2016, with one difference: in the case of horn 1 the polar modulator has been fixed to avoid eventual shifts in its zero position, while other horns can still rotate the polar modulators allowing an additional reduction of systematic effects (see O'Dea et al. 2007; Vignaga 2012).

The final equations for the response of the MFI after the modifications are the following:

$$C_{\mathrm{X+Y}} = \tfrac{1}{2}\big[I + Q\sin(4\theta) + U\cos(4\theta)\big] \tag{2.9}$$
$$C_{\mathrm{X\text{-}Y}} = \tfrac{1}{2}\big[I - Q\sin(4\theta) - U\cos(4\theta)\big] \tag{2.10}$$
$$C_{\mathrm{X}} = \tfrac{1}{2}\big[I - Q\cos(4\theta) + U\sin(4\theta)\big] \tag{2.11}$$
$$C_{\mathrm{Y}} = \tfrac{1}{2}\big[I + Q\cos(4\theta) - U\sin(4\theta)\big] \tag{2.12}$$

The equations are very similar to Eqs. (2.2)-(2.5) since the second 90º hybrid cancels the effect of the first one in the correlated channels, while the signs in the equations of the previously uncorrelated channels are inverted.

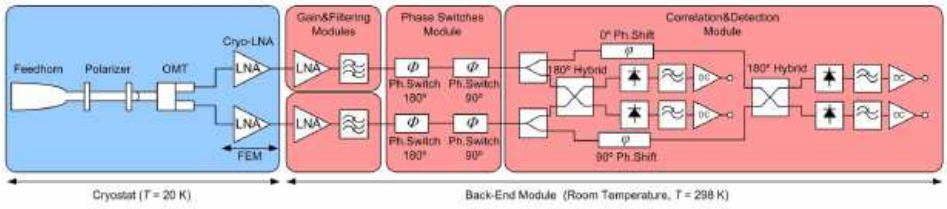

FIGURE 2.5— The final scheme for the TGI receiving system. The polar modulator has been replaced with two phase switches. See text for details.

2.2.4 Thirty-GHz Instrument (TGI)

This instrument is mainly devoted to constrain the amplitude of the primordial B-modes. With this instrument, we will be able to reach a sensitivity lower than 1 μK per square degree in an area of 3000 square degrees after three years of operation, allowing a detection of B-modes if $r = 0.1$. The TGI consists of 27 polarimeters working in the frequency range 26-36 GHz. As it was mentioned before, after the laboratory tests with the 30 GHz polarimeter of the MFI, we found that the MFI design, based on the spinning polar modulators in a cryogenic environment and shown in Fig. 2.3, is not appropriate for the long-term operations required for the TGI. For this reason, the receiver configuration has been modified by replacing the rotating polar modulator with a fixed polariser. The current new design is presented in Fig. 2.5. It includes a fixed polariser and two 90º and 180º phase switches to generate four polarisation states to minimise the different systematics in the receiver. The data will be recorded at 8 kHz rate, but the detection of Q and U will be almost instantaneous since the phase is switched at frequencies up to 16 kHz. The BEM for the 30 GHz instrument was built by DICOM, with collaboration of *Instituto de Física de Cantabria* at the simulation level.

2.2.5 Forty-GHz Instrument (FGI)

The design of the Forty-GigaHertz Instrument will be a replica of the second instrument but at 40 GHz. It will be devoted to primordial B-mode studies. Combining the two instruments, we will be able to lower the detection threshold of B-modes down to $r = 0.05$. The FGI will consist of 28 polarimeters working at 40 GHz. At the moment of the writing of this thesis, the second telescope is hosting a mixed configuration with 14 pixels of the TGI and 15 pixels of the FGI, which are been commissioned simultaneously. The conceptual design of a polarimeter chain for the FGI is identical to the one used for the TGI (see Fig. 2.5).

Observing Mode	Targets
Nominal mode	Northern sky
Transit mode	Low S/N sources
Raster mode	Calibration sources
Sky raster mode	Calibration sources
Sky dips	Atmospheric calibration
Local maps	Satellites and interferences

TABLE 2.2— Summary of the observing modes of the MFI and usual targets.

2.3 Observing Modes of the MFI

The observing modes implemented in the QUIJOTE first telescope are summarised in table 2.2. Here we proceed with a brief description of each of them.

Nominal Mode

The nominal mode consists of a continuous rotation of the telescope around the azimuth axis at constant speed, keeping fixed the elevation. Each rotation covers the declination band $[\phi - z, \phi + z]$, where z is the zenith angle and $\phi = 28^{\circ}$ is the observatory latitude, and a full-day observation provides the full range of right ascensions due to Earth rotation. This mode presents several advantages:

1. it covers a large area in the sky,
2. it allows the fastest rotation[5] of the telescope (since the rotation is always in the same direction) thus minimising the 1/f noise,
3. it keeps the elevation constant, thus reducing the atmospheric contamination[6].

The final observing strategy for this mode consists of 24-hour observation at the same elevation and modulator angle position. The observation is then repeated 3 times with other modulator angles before changing the elevation, which is usually stepped by 5 or 10° (from $EL = 30^{\circ}$ to $EL = 80^{\circ}$). The amount of time spent at each elevation is chosen to have a coverage as uniform as possible in the full observed area. At the writing of this thesis (31 May 2018), 10326 hours of observations have been obtained with this mode, covering over 20000 square degrees of the sky.

[5]Initially we set the telescope azimuth velocity to 6°/s, then we increased it to 12°/s.

[6]Changing the elevation implies changing the air mass seen by the instrument and this affects the baseline level.

Transit Mode

In the transit mode the telescope moves horizontally in a limited range of azimuths around the central coordinates of the target. The elevation is kept constant in order to avoid changes in the baseline due to different atmospheric emission associated with different air mass. The sky coverage is obtained with the rotation of the Earth. Given the separation of the horns of the MFI in the focal plane ($\sim 5^{\circ}$), the minimum scan length is usually $\Delta\mathrm{AZ} \geq 10^{\circ}$. Also, the speed of each scan has to be reduced with respect to Nominal Mode to avoid mechanical problems when inverting the AZ direction. We usually choose $V_{\mathrm{tel}} = 1^{\circ}/\mathrm{s}$ in sky coordinates[7]. The observation duration is chosen to have maps in the sky with the same size along the the declination direction and the right ascension. This observing method is the best suited for deep observations in specific regions of the sky, for example the Cosmological fields[8], the Haze region (see chapter 5.6.1), Jupiter and almost all the point sources apart from the calibrators.

Raster Mode

The raster mode allows to make square maps in local sky coordinates (AZ-EL) and it is used to observe strong sources, especially the calibrators. It starts by moving the telescope horizontally (fixed elevation) for usually 10° in the sky, then it steps in elevation by 0.1° and comes back horizontally to the initial azimuth. This process is repeated 100 times, in order to cover 10° in elevation. The steps in elevation are taken in the opposite direction of the source movement with respect to the Earth: if the source is rising with respect to the local horizon, it starts at an elevation 5° higher than the mean elevation of the source during the observation and the elevation decreases at each step. The advantage with respect to the transit mode is the lower duration: while a transit observation lasts from 40 minutes for a small region to 3 hours for a COSMO field[9], a raster usually takes only 23 minutes, which is very important since we do daily calibration observations of Cassiopeia A (hereafter Cas A) and the Crab Nebula (hereafter Tau A). The drawback is that we have lower integration time and have to remove a baseline of an azimuth scan in order to remove the

[7] $V_{\mathrm{tel}}^{\mathrm{AZ}} = 1/\cos(EL)^{\circ}/\mathrm{s}$ with the approximation in Kovalevsky (2002) for the conical projection.

[8] The other way the MFI does cosmological observations is through 3 clear fields (the choice has been made based of the Planck catalogue of point sources), which provide a wide area ($\sim$ 3000 squared degrees) with a higher S/N than nominal maps

[9] As it was mentioned before, the time in transit mode is chosen to have map of the same size in RA-DEC. For a small region this size is 10-15°, while for the COSMO fields it is 33° and we have to wait the Earth to move that much.

effect of the different air masses on the baseline levels. At the time of writing this thesis, with this observing mode we have accumulated ~ 625 hours of Tau A observations, ~ 600 hours of Cas A observations, 31.8 hours of observations on the Moon and 22.5 hours of geostationary satellites, which will be used for the optic characterisation in chapter 3.

Sky Raster Mode

The sky raster mode is very similar to the raster mode but the raster is done in equatorial coordinates (RA,DEC). It was implemented in order to have a squared sky coverage in equatorial coordinates. However, the contamination from the atmosphere changes significantly with the elevation:

$$T^{\rm atm}(EL) = \frac{T_0^{\rm atm}}{\sin EL} \tag{2.13}$$

with $T_0^{\rm atm}$ being the contribution of the atmosphere to the antenna temperature at the MFI frequencies at the zenith. It also had some technical issues at very high elevation since the velocity in azimuth when tracking is proportional to $1/\cos(EL)$ and the observations stopped when the velocity was higher than the mechanical limit of the telescope. Thus this mode was discarded before the end of the commissioning phase.

Sky Dips

This observing mode consists of fixing the azimuth and moving the elevation back and forth typically between elevation 30º and 90º several (usually 6) times (12 minutes). The idea is to obtain the contribution of $T_0^{\rm atm}$ in Eq. (2.13) by measuring $T^{\rm atm}(EL)$ at each elevation and fitting the cosecant dependence. Apart from that, the sky dips are useful to calibrate the relative gains (see subsection 2.6.6) of pairs of channels (the (X+Y) with the (X-Y) and the (X) with the (Y)) since the atmosphere is not polarised. We made daily a sky dip observation at AZ= 270º and sometimes a second one at AZ= 90º.

Local Map

This mode is a mixture between the nominal mode and the raster mode since it combines the continuous rotation with the stepping of the elevation, covering all the elevation range of the telescope. Each local map can last from 3 to 8 hours, depending on the step used for the elevation, which was 0.25º during the commissioning phase and then reduced to 0.08º for a better S/N. With this observing mode we map the geostationary satellites and all the radio interferences still in local coordinates (AZ,EL), like ground reflections or interferences

from the far sidelobes from the same satellites (see sections 3.4.4). The total amount of data in local maps is 101.7 hours for an observed area of 10313 square degrees.

2.4 The MFI Pipeline

The pipeline of the MFI includes all the processes that transform the Raw Data from the telescope into the Calibrated Time Ordered Data (CTOD), which are the inputs for the map-making codes described in the next section. This pipeline has been improved and developed continuously since the start of the MFI observations and several intermediate files have been produced. A summary of the steps of the pipeline is shown in Fig. 2.6. This thesis includes data from the commissioning phase of the MFI to recent observations, and a detailed description of each step in the pipeline is necessary to understand the kind of information available at each moment. Sections 2.6, 2.7 and 3.4 use only the first steps of the pipeline, called Time Ordered Data (TOD). The second step involved the separation of the calibration data in calibration files and Binned Time Ordered Data (BTOD), which are used in section 3.5, chapter 4 and chapter 5. Only sections 5.6.1 and 5.6.2 use data processed with the pipeline at his current state.

2.4.1 Raw Data

The raw data produced by the MFI are organised in five types of files, each one containing different information (Génova-Santos, 2013). These are:

1. Science data files: they contain the response of the 32 channels of the MFI recorded at the sample frequency of 1 kHz. They also contain information on the calibration signal.

2. Telescope data files: they contain the telescope pointing position (AZ and EL) of the centre of the focal plane. These are read from the encoders placed inside the telescope and are not the positions commanded to the telescope, which are stored in a separate file, used only for tests and in case of errors.

3. Modulator data files: they contain the position angles of each of the four polar modulators.

4. House Keeping data files: they contain all the information about the configuration of the observation (pointing, velocity, repetitions, etc.), the configuration of the internal calibration diode and the status of the modulators. Also, they keep track of the temperature and pressure measured in

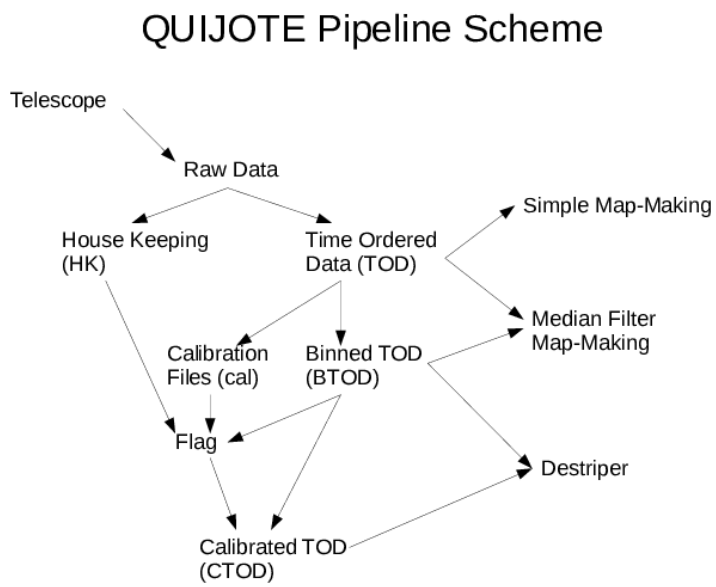

FIGURE 2.6— Scheme of the QUIJOTE pipeline. The Raw Data coming from the telescope are processed in various steps (TODs, BTODs, CTODs) by adding information (HK, flagging) and by compressing (binning) the data. Then the maps are obtained with increasing complexity map-makings. With "Simple Map-Making" we refer to maps of individual channels, which are used only for calibration purposes.

several place of the cryostat and outside. They are sampled at a frequency of 1 Hz.

2.4.2 Time Ordered Data (TOD)

The first process in the pipeline of the MFI is the synchronisation and compression of all the information. This is done by a F90 routine that produces two binary files: the Time Ordered Data (TOD) and the "compressed" House Keeping files (HK).

The TOD files contain the Julian date of each time sample referred to 2456244.5 (the Julian date of the beginning of the commissioning), the corresponding azimuth and elevation of the telescope from the encoder readings, the position of the polar modulator, the data from all the 32 channels and an additional flag indicating if the calibration signal is switched on or off. All the information is stored at the original sampling rate of 1 kHz, without any loss of information.

The name of each file contains the name of the field, the nominal position of the modulator with a letter from A to D corresponding to 0, 22.5, 45 and 67.5º, the date and time of the observation and finally an extension indicating the type of file[10]. For example, the file COSMO3C-130823-1659-000.tod which is used in section 2.7 is an observation of the third QUIJOTE cosmological field with the modulator position set to 45º (modulator position C). The observation is dated 23 August 2013 and started at 4.59 p.m. UT. The extension "-000.tod" indicates that this is the first ordered file of the observation (a TOD contains 24 minutes).

2.4.3 Calibration Files and Binned Time Ordered Data (BTOD)

The second process in the MFI pipeline is the separation of the data where the internal calibration signal is switched on and off. This leads to two different files, called Binned Time Ordered Data and Calibration files.

The calibration files contain the signal of the internal calibration system, which will be explained in detail in Section 2.7. This includes several parameters that are used for the flagging of the data. The information is stored at one sample every 31 s, which corresponds to one cycle of the calibration diode.

The Binned Time Ordered Data are the main data files used in this thesis to build the maps since they include the minimal pre-processing necessary and

[10]Some extensions contain a progressive number. This is because the file size of the raw data is limited to 40 MB that corresponds to 24 minutes of telescope data, 6 minutes of scientific data and so on. If the observation is longer the data are split in several files.

they are not as large as the TOD. The main steps followed to obtain the BTOD from the TOD are:

1. The binning of the data: this is usually done at intervals of 60 ms[11] and has two advantages: to reduce the amount of data that has to be stored and to drastically reduce the amount of time to build the maps or to analyse the data. However, the binning time cannot be very high because the telescope is spinning quite fast and at least 3 binned samples per beam are needed. Apart from the binned data, also the RMS calculated in each bin is stored to compute the error that will be propagated to the maps.

2. The Galactic coordinates corresponding to the pointing of each horn on the sky, after applying the pointing model (PM) of the telescope. In fact, the application of the full PM is quite time-consuming, has to be done separately for each horn and it is a necessary step for all the maps. However, the encoder coordinates of the telescope are kept in order to build maps in local coordinates and to flag out the geostationary satellites.

3. The basic flagging of the data, based on the distance from bright sources (Sun, Moon, geostationary satellites), on the HK values and, finally, on the presence of outliers in the data.

Finally, the conversion factors from voltage to temperature and zero modulator position obtained through the calibration are stored in each file.

2.4.4 Flagging

The basic flagging done at the BTOD level is usually insufficient to remove all the undesired artefacts in the data, such as stripes from interferences, strong contamination from the atmosphere due to bad whether, etc. For this reason, several additional flagging procedures have been implemented:

1. The calibration files are used as a first estimation of the baseline levels and of the gain model. A visual inspection is performed and, if these values are out of the usual range or present strong variations, the entire observation is discarded. A code for a partial flagging has also been implemented, but its use has been limited mainly to Nominal Mode observations, given their longer duration ($\approx$ 24 hours). This test is very sensitive to artefacts in the data that change with the time, such as contamination from the atmosphere, since a sudden change of the Relative Humidity (HR) or the temperature is visible on the baseline, or some geostationary satellites which do not present a constant emission.

[11] 40 ms in nominal mode.

2. The RMS of the data is calculated in bins of 3 minutes for all MFI observations and compared to a threshold for each channel[12]. Each bin with an RMS above the threshold is discarded automatically.

3. For the previous bins, the RMS of the ratio of corresponding channels (X with Y, and X+Y with X-Y) is computed, compared with a threshold and discarded if too large.

4. After these automatic flags, maps of single observations have been produced for each channels. This allowed a better detection of artefacts in the space domain, such as interference patterns from the ground or from geostationary satellites. The maps are then visually inspected and, if some artefacts are detected, the full observation is discarded.

2.4.5 Calibrated Time Ordered Data (CTOD)

The Calibrated Time Ordered Data contained the final baseline-subtracted, flagged and calibrated data.

The baseline subtraction procedure calculates a median value of the data for each scan at constant elevation of the telescope. This can be subtracted from the data (ideal for observations of compact or point sources) or not (ideal in the case of cosmological observations).

The calibration includes three factors: the Volt-to-Kelvin conversion, which is calculated from Cas A observations (see subsection 2.6.6), a factor that takes into account the different absorption of the modulator based on its position (see subsection 2.6.8), and a gain factor which takes into account fluctuations on the gain of the amplifiers through the internal calibration system and will be explained in subsection 2.7.3.

2.5 Map-making Methods

Making a map[13] $\vec{m}$ from a given dataset $\vec{x}$ in the time domain (for example the TOD), requires inverting the equation:

$$\vec{x} = P\vec{m} + \vec{n} \tag{2.14}$$

where P is the projection matrix, which projects the value of each pixel of the map into the the TOD through the pointing, and $\vec{n}$ is the noise vector

[12]The threshold is chosen in order to discard a fixed amount of data, which is 5-10% at the moment of writing of this thesis, depending of the channel.

[13]In this notation the map is 1-dimensional: we have defined an order for all the pixels and the i-component of $\vec{m}$ is the value of the map in the i-pixel. It is the same procedure used for example with the HEALPix (Górski et al., 2005) pixelisation.

(Peláez-Santos, 2013). The formal solution of the problem can be found with the maximum likelihood method, maximising the probability p of the data $\vec{x}$ given the map $\vec{m}$, which is

$$p(\vec{x}|\vec{m}) \propto \frac{\exp\left(-\frac{1}{2}(\vec{x}-P\vec{m})^{\mathrm{T}}N^{-1}(\vec{x}-P\vec{m})\right)}{\sqrt{|N|}} \tag{2.15}$$

where we introduced the covariance of the noise N as the average over many realisations of the noise. The solution can be found by minimising the $\chi^2(\vec{m}) = -2\ln p$, which gives:

$$\vec{m} = (P^{\mathrm{T}}N^{-1}P)^{-1}P^{\mathrm{T}}N^{-1}\vec{x} \tag{2.16}$$

This equation requires the inversion of the covariance matrix, which is computationally very expensive.

The various map-making methods mainly differ on the assumptions used to invert N and in the method to remove the baseline level coming from the system temperature contribution. In the QUIJOTE group, two approaches have been implemented: one applies a median filter to remove the baseline and assumes N to be diagonal (median filter map-making) and the other one applies a destriping algorithm to remove the 1/f contribution to the noise, also with the assumption that N (after the removal of the 1/f contribution to the noise) is diagonal.

The equations that give the Stokes parameters from the output of the MFI channels can be derived from the response of the MFI (Eqs. 2.2-2.5). With that notation, we can define the sum and the difference of correlated channels, d_i^+, d_i^-, and we have for each pixel:

$$d_i^+ = C^i_{x+y} + C^i_{x-y} = \qquad I \tag{2.17}$$

$$d_i^- = C^i_{x+y} - C^i_{x-y} = \quad Q\sin\theta_i + U\cos\theta_i \tag{2.18}$$

where the angle θ_i depends on four times the polar modulation, which is the position of the modulator ϕ_{mod_i} minus its zero, ϕ_0), and on two times the parallactic angle γ_{par_i}, so that

$$\theta_i = 4(\phi_{\mathrm{mod}_i} - \phi_0) + 2\gamma_{\mathrm{par}_i} \tag{2.19}$$

The index i goes through all the data that lie inside the same pixel. The Stokes parameters of each pixel can be estimated as the best values that fit the data, thus we can write two χ^2 functions, one for intensity and one for polarisation[14]:

$$\chi^2_{\mathrm{I}} = \sum_i \frac{(d_i^+ - I)^2}{\sigma_i^2} \qquad \chi^2_{\mathrm{P}} = \sum_i \frac{(d_i^- - Q\sin\theta_i - U\cos\theta_i)^2}{\sigma_i^2} \tag{2.20}$$

[14]We are assuming that N is diagonal and that the noise associated to each data point is Gaussian, omitting any correlation between consecutive data.

where the σ_i represents the error associated to each data point (if the data come from the BTOD, it will be the RMS of the channel response calculated in each bin). The solution in this case is analytical and gives for intensity:

$$I = \frac{\sum_i \frac{d_i^+}{\sigma_i^2}}{\sum_i \frac{1}{\sigma_i^2}} \tag{2.21}$$

and, similarly, for polarisation:

$$Q = \frac{af - cd}{ab - c^2} \qquad U = \frac{bd - cf}{ab - c^2} \tag{2.22}$$

where

$$a = \sum_i \cos\theta_i^2 \sigma_i^{-2} \tag{2.23}$$
$$b = \sum_i \sin\theta_i^2 \sigma_i^{-2} \tag{2.24}$$
$$c = \sum_i \cos\theta_i \sin\theta_i \sigma_i^{-2} \tag{2.25}$$
$$d = \sum_i d_i^- \cos\theta_i \sigma_i^{-2} \tag{2.26}$$
$$f = \sum_i d_i^- \sin\theta_i \sigma_i^{-2} \tag{2.27}$$

Median Filter Map-Making

This map-making removes the baseline of the data at the TOD level through a median filter with a kernel of usually 20 s and assumes a diagonal covariance matrix N. Its main advantage with respect to other map-making methods is that it is computationally very fast. However, we lose all information about angular scales larger than $\approx 20^o$, assuming that the telescope is moving at 1^o/s. The maps analysed in chapter 5 have been built using the destriper code in intensity and this map-making in polarisation. This map-making method has also been implemented for the "improved" MFI receiving system, but this implementation has not been used in this thesis.

Destriper

The destriper code (Peláez-Santos, 2013) assumes that the noise has two components: the white uncorrelated noise $\vec{n'}$ and a slowly varying component represented by a baselines vector $F\vec{b}$. The matrix F represents how the 1/f noise is projected along the baselines to the TOD. Thus we can maximise $p(\vec{x}|\vec{m}, \vec{b})$

where $\vec{x} = P\vec{m} + F\vec{b} + \vec{n'}$ instead, which gives[15]:

$$Z = \mathbb{1} - P(P^{\mathrm{T}}N'^{-1}P)^{-1}P^{\mathrm{T}})N'^{-1} \quad (2.28)$$

$$\vec{b} = (F^{\mathrm{T}}Z^{\mathrm{T}}N'^{-1}ZF)^{-1}F^{\mathrm{T}}Z^{\mathrm{T}}N'^{-1}Z\vec{x} \quad (2.29)$$

$$\vec{m} = (P^{\mathrm{T}}N'^{-1}P)^{-1}P^{\mathrm{T}}N'^{-1}(\vec{x} - F\vec{b}) \quad (2.30)$$

where we introduced the covariance matrix N' of the white noise $\vec{n'}$, which is diagonal by definition. This last equation is the same as Eq. 2.16, but the data have been previously fitted for the 1/f noise and the corresponding baselines have been removed. The equations that give the Stokes parameters are then Eq. 2.21 and Eq. 2.22, after the removal of the 1/f component.

More details about this can be found in Keihänen et al. (2004) and in Kurki-Suonio et al. (2009) for a general description of the algorithm, in Schlegel et al. (1998a) for the example of the application of the destriper to the DIRBE instrument, in Keihänen et al. (2010) for the application to Planck LFI data (code named MADAM, which is not publically available) and finally in Peláez-Santos (2013) and in Harper (2016) for their two independent implementations in QUIJOTE. While this method is the only one that accounts for the 1/f noise in intensity, it is computationally expensive. Also, it has not been adapted to combine the output of the four channels for the "Improved MFI" receiving system.

Other Map-Making Methods

Another map-making method has been implemented independently by the author during the commissioning phase (in Fig. 2.6 it is called "Simple Map-making") and has later been adapted to make maps in local coordinates (see section 3.2). It applied a median filter at the TOD level to remove the baseline and then built an intensity map as a weighted average of the data for each channel. The major part of the calibration during the commissioning phase was done with this simple map-making, without using the HEALPix projection.

Finally, we mention that another map-making method for QUIJOTE has been implemented separately in Harper (2016), which uses the Conjugate Gradient Method both to reduce the computational time of the destriper and to invert the full matrix $(P^{\mathrm{T}}N^{-1}P)^{-1}P$ under some assumptions, like it is sufficiently sparse, symmetrical and positively definite. This map-making was applied mainly to data obtained in nominal mode and it is not used in this work.

[15] This equation can be generalised to whatever N. We use here N' since the destriper code implemented in Peláez-Santos (2013) assumes that the non-1/f component of the noise is Gaussian. See Harper (2016) for a derivation of the next equations.

2.6 Calibration and Commissioning of the MFI

In this section we explain the work done in the commissioning phase of the MFI, before the pipeline was consolidated, and its final calibration. Only the TOD and HK files were available at the moment of doing this analysis. Also, we will explain in some detail the determination of some calibration factors that are used at the BTOD level, like the conversion factors between voltage and temperature and the modulator reference position angles. The main contributions of the author to the commissioning and calibration of the MFI were the fit of the geometry of the focal plane (described in subsection 2.6.1, the internal calibration system (described in the section 2.7) and with the beams characterisation (described in the chapter 3). The PM is described in details in Tramonte (2013) whereas the characterisation of the 1/f noise is presented in Peláez-Santos (2013). The calibration procedure is partially described in Génova-Santos et al. (2015b), but an article describing the full calibration of QUIJOTE and its pipeline is currently in preparation. For this reason it is described here although the author did not participate in all the process.

2.6.1 Geometry of the Focal Plane

One of the first steps in the commissioning phase was the determination of the geometry of the focal plane. We already had a measure of the geometrical position of each horn with respect to the centre of the focal plane (see column 2 and 3 of table 2.3) but we wanted to confirm that with an astronomical source. This was done with a raster mode observation of the Moon, dating 12 November 2012. Fig. 2.7 shows a map made at that moment with the "simple map-making" method combining all the channels. The Moon is seen 4 times because of the displacement of the horns with respect to the centre of the focal plane, and its amplitude is different in each horn because we did not apply the voltage-to-temperature factors. Also it seems very elongated because the conical projection correction was not been applied. The projection from sky (spherical) coordinates (α,δ) centred around the point (α_0,δ_0) to the flat focal plane coordinates (x, y) was obtained as in Kovalevsky (2002). The equations are the following ($\alpha = \alpha_0 + \Delta\alpha$, $\delta = \delta_0 + \Delta\delta$):

$$x = \frac{\sin\Delta\alpha}{\cos\delta_0(\tan\delta_0\tan\delta + \cos\Delta\alpha)} \approx \Delta\alpha\cos\delta_0 \tag{2.31}$$

$$y = \frac{\tan\delta - \tan\delta_0\cos\Delta\alpha}{\tan\delta_0\tan\delta + \cos\Delta\alpha} \approx \Delta\delta \tag{2.32}$$

The right sides of the equations represent the first order approximations for $\Delta\alpha \ll \alpha_0$ and $\Delta\delta \ll \delta_0$. In order to confirm that the position of the horns

	$x_{\rm Inst}$ (mm)	$y_{\rm Inst}$ (mm)	$x_{\rm Sky}$ ($^{\rm o}$)	$y_{\rm Sky}$ ($^{\rm o}$)
Horn 1	90.00	-155.88	1.417	-2.454
Horn 2	-155.88	-90.00	-2.454	-1.417
Horn 3	-90.00	155.88	-1.417	2.454
Horn 4	155.88	90.00	+2.454	1.417

TABLE 2.3— Positions of the horns in the focal plane of the MFI as measured by the engineering team and corresponding positions in sky coordinates, assuming the nominal focal length of 3637 mm.

measured in the laboratory was correct, we made a simulation to replicate the TOD of the observation of the Moon and compared the results. First, for each channel, we fitted the resulting map with an elliptical Gaussian:

$$B(x,y) = A\exp\left(-\frac{1}{2\sigma_\mu^2}[(x-x_0)\cos\chi + (y-y_0)\sin\chi]^2 \right. \\ \left. -\frac{1}{2\sigma_\nu^2}[-(x-x_0)\sin\chi + (y-y_0)\cos\chi]^2\right) \quad (2.33)$$

which gave the amplitude A, the position of the centroid (x_0, y_0), the axes (σ_μ,σ_ν) and an eventual rotation angle of the ellipse with respect to the AZ-EL coordinates. After this, we simulated a TOD file of the observation, using as a model another elliptical Gaussian with the amplitude A retrieved from the fit, the nominal FWHM of each horn of the MFI corrected for the angular size of the Moon (0.5$^{\rm o}$), and the nominal positions of each horn, which were converted in degrees with the nominal focal length of the telescope (3637 mm), as seen in column 4 and 5 of table 2.3, and then corrected to take into account the conical projection. The comparison of the simulation with the original map is shown in Fig. 2.7, in which we see an almost perfect agreement between the two maps.

2.6.2 Pointing Model

Any real telescope is affected by non-idealities that produce errors in the pointing. This effect can be corrected by a set of coordinate transformations, which are parametrised by the Pointing Model (PM). In the case of QUIJOTE, the model presented in Wallace (2008) is used, which consists of seven parameters that take into account the vertical flexure of the telescope, the misalignment between the azimuth axis with respect to the vertical, the non-perpendicularities between the mount axes of the telescope and eventual offsets in the encoders measurements. The vertical flexure of the telescope, which takes into account the bending of the telescope due to its own weight, has particular relevance,

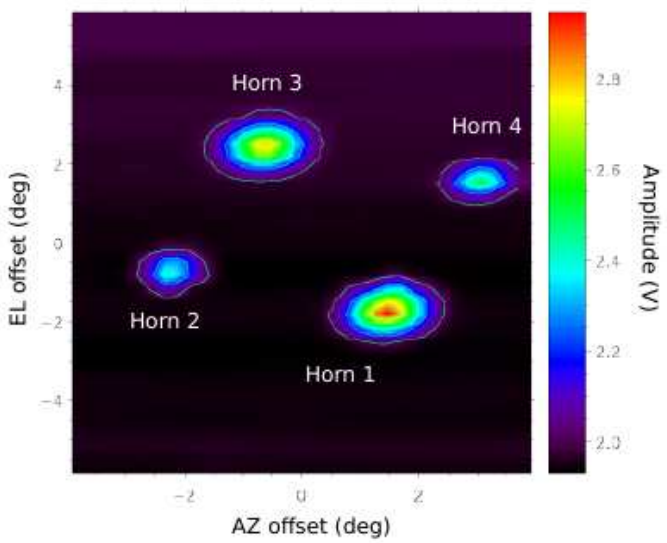

FIGURE 2.7— Simulation (in colour scale) of the observation according to the nominal position of the horns in the focal plane and the nominal FWHM of the MFI. The contours show the observation of the Moon with the MFI on 12 November 2012, a few days after the first light of the telescope. See text for details.

since the correction depends strongly on the elevation. For this reason, observations made at different elevations could not be combined before a good characterisation of this effect had been performed, since the resulting map would present smearing effects or elongations on the beam shape. The details of the determination of the PM for the QT1 can be found in Tramonte (2013). The analysis used individual observations of Cas A and Tau A, which were fitted at the TOD level in order to find the optimal solution for the PM parameters, with the objective of a precision in the pointing of $\lesssim 1$ arcmin, which is sufficient considering the minimum beam size of the MFI (0.6° for the high frequency horns).

2.6.3 Bandpass Characterisation

Each horn of the MFI is sensitive to a frequency range: from 10 to 14 GHz or from 16 to 20 GHz. The bandwidth is then split in two halves in order to better determine the spectrum of the incoming radiation. Ideally, the responsivity of the detector should be uniform across the the full band, but a full characterisation is essential since it affects the main flux calibration through the colour correction. The flux density detected by the receiver is the weighted integral of

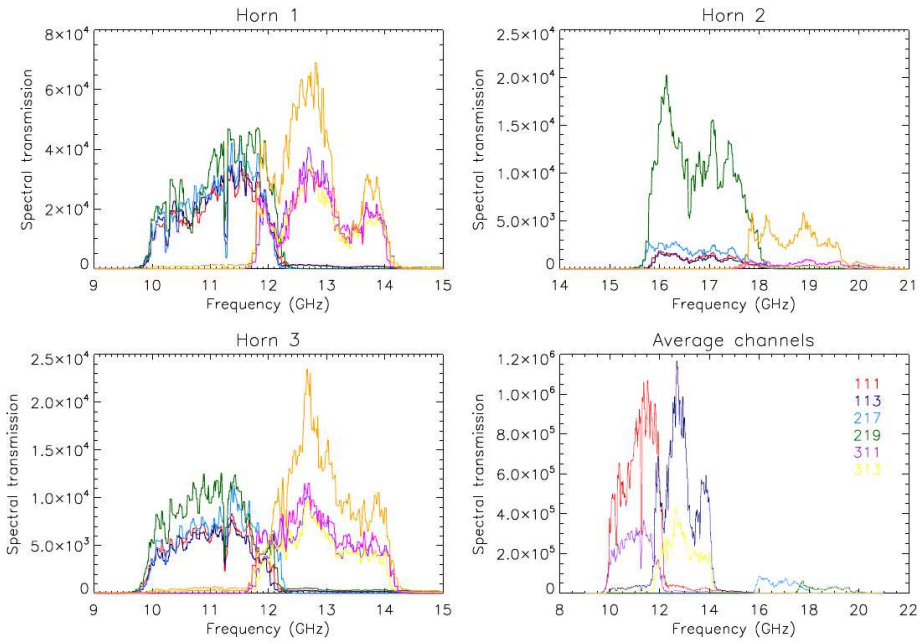

FIGURE 2.8— Bandpasses of the first three polarimeters of the MFI before April 2014. Each coloured line represents a different channel. The fourth horn bandpasses were not calculated due to the insufficient amplification of its LNAs. The bottom-right panel shows the comparison between the different horns and frequencies. Credit: Génova-Santos & Hoyland (2014).

the source spectrum across the whole bandpass $g(\nu)$:

$$S = \frac{\int g(\nu) S_{\rm source}(\nu) d\nu}{\int g(\nu) d\nu} \tag{2.34}$$

where we introduced the real spectrum of the source, $S_{\rm source}$.

Also, the presence of a finite bandwidth affects the polarisation measurements, since any difference in the bandpass of the two channels to be subtracted results immediately into a leakage from intensity to polarisation.

The characterisation of the bandpasses has been done in the laboratory before the beginning of the commissioning by the engineering team (Génova-Santos & Hoyland, 2014) and its results are shown in Fig. 2.8. Horn 4 has not been measured since the original amplifiers were of lower quality and had higher noise than those in other horns (they were replaced in April 2014).

2.6.4 Beams

The beam characterisation will be fully explained in chapter 3 since it is one of the main goals of this thesis. Here, we just mention that during the commissioning the beam values were calculated by 2D elliptical Gaussian fitting over individual Cas A observations. A better approach would use a stacking of several observations to enlarge the S/N of the map, but, since the PM was not available, this would have caused smearing effects or elongations in the beam shape.

2.6.5 1/f Noise

The noise introduced by the LNAs presents typically two components, one is the white noise and the other is the 1/f noise. Due to its proper nature, the characterisation of the 1/f noise has to be done in the Fourier domain and requires avoiding strong sources but also gaps in the data. For this reason, special observations on blank fields with the calibration system switched off were made during the commissioning. The noise spectrum was modelled (Peláez-Santos, 2013) with:

$$PS(f) = \sigma^2 \frac{N_t}{f_{\text{samp}}^2} \left[1 + \left(\frac{f_k}{f}\right)^{\alpha}\right] \tag{2.35}$$

where the 3 free parameters are the amplitude of the white noise σ^2, the knee-frequency f_k, which is the frequency where the white noise and the 1/f noise have the same amplitude, and the exponent α of the power law. The sampling frequency $f_{\text{samp}} = 1\,\text{kHz}$ and the number of input data N_t are fixed. The analysis done in Peláez-Santos (2013) showed that:

1. The spectral index of the 1/f component is $\alpha \sim 1$. This is the value expected for the type of detectors in the MFI.

2. The knee frequencies of individual channels range from 10 Hz to 100 Hz depending on the horn and the channel.

3. In general, correlated channels have lower f_k in polarisation, due to the subtraction of channels affected by the same 1/f.

4. The knee frequency in polarisation (difference in correlated channel) is reduced to 0.2 Hz

5. The values fitted for σ^2 are compatible with the nominal NET (see Eq. 2.1).

Source	Cas A	Tau A
Intensity	see Eq. (2.36)	see Eq. (2.38)
Polarisation Fraction (%)	0.35	7.08
Polarisation Angle (°)	82.7	-88.5

TABLE 2.4— Intensity and polarisation of the main calibrators of the MFI as in Weiland et al. (2011). No secular decrease has been taken into account for this table. See text for details.

2.6.6 Amplitude Calibration

The amplitude calibration of the MFI is done by comparing the output voltage of the observations of the calibrator (Cas A) with its flux density as modelled in literature. The best estimate for the flux density of Cas A at the moment of the commissioning was given by the WMAP 7-years results (Weiland et al. 2011, Table 17) as:

$$\log(S^{2000}_{\text{Cas A}}(\nu)) = (2.204 \pm 0.002) - 0.682 \pm 0.011)\log(\nu/40) + \\ + (0.038 \pm 0.008)(\log(\nu/40))^2 \quad (2.36)$$

where the flux density is given in Jy and the frequencies in GHz. This estimate is referred to the year 2000 and this is necessary since the source presents a secular decrease. In fact, using data from the VSA, Hafez et al. (2008) found:

$$\left(\frac{dS}{Sdt}\right)_{\text{Cas A}} = [(0.68 \pm 0.04) - (0.15 \pm 0.04)\log\nu]\,\%\ \text{year}^{-1} \quad (2.37)$$

For a detailed description of the calibration procedure we refer to Génova-Santos (2015a). In summary, daily maps of Cas A observations are produced and fitted to retrieve the flux density (in Volts) of each channel of the MFI[16]. Then, each flux density (in Volts) is compared to the flux of Cas A from Eq. 2.36 integrated along the bandpass of the channel. Their ratio provides daily amplitude calibration factors used to convert from Volts to Jansky, and also from Volts to Kelvin given the beam shape.

The final amplitude calibration factors are the medians of these daily factors and are stored in the BTODs. At the CTOD level these values are corrected for the gain variations using the model that is obtained using the internal calibration system (see section 2.7) and by the modulator absorption (see subsection 2.6.8).

[16]The maps built from individual channels are a combination of I, Q, U, dependent of the position of the modulator and the parallactic angle, but, since Cas A is practically unpolarised (see table 2.4), they are a very good approximation to the intensity-only maps.

The overall calibration error is estimated to be of the order of 5%, given the day-to-day scatter in Cas A fluxes after this calibration. This scatter reduces up to 2% if we choose to calibrate using only observations with similar BEM temperature, which is closer to the calibration error of the model (Weiland et al., 2011), which is $\approx 1\%$. For this reason, it was decided that the BEM temperature had to be stabilised and in December 2016, six thermal mats[17] have been inserted to the BEM of the MFI. The same mechanism is used for the BEMs of the other QUIJOTE instruments.

2.6.7 Polar Modulator Angle

For the calibration of the reference position angle ϕ_0 of the polar modulator, a polarised source is needed. The brightest polarised point source in the sky is Tau A, with a polarisation fraction of $\Pi_{\text{Tau A}} = 7.08\%$ at 23 GHz according to Weiland et al. (2011) (see table 2.4). We suppose that it is constant down to 11 GHz since Faraday depolarisation effects should occur at lower frequency. We also assume that neither the polarisation angle changes at our frequencies, so $\gamma_{\text{Tau A}} = -88.5^{\text{o}}$. We present here for completeness the equation for the flux density of Tau A, although only its polarisation angle is needed for calibration of the modulator:

$$\log(S^{2000}_{\text{Tau A}}(\nu)) = (2.506 \pm 0.003) - (0.302 \pm 0.005)\log(\nu/40) \tag{2.38}$$

Like Cas A, its flux suffers a secular decrease of $(-0.22 \pm 0.07)\%$ year^{-1} (Hafez et al., 2008).

Then, from Eq.(2.2) to Eq.(2.5), we have[18]:

$$\begin{aligned}\frac{C_{\text{X-Y}} - C_{\text{X+Y}}}{C_{\text{X-Y}} + C_{\text{X+Y}}} &= \frac{Q_{\text{Tau A}}\sin(\theta) + U_{\text{Tau A}}\cos(\theta)}{I_{\text{Tau A}}} = \\ &= \Pi_{\text{Tau A}}\cos(2\gamma_{\text{Tau A}})\sin\theta - \Pi_{\text{Tau A}}\sin(2\gamma_{\text{Tau A}})\cos\theta\end{aligned} \tag{2.39}$$

and we recall that $\theta = 4(\phi_{\text{mod}} - \phi_0) + 2\gamma_{\text{par}}$, that is 4 times the encoder position angle of the modulator (minus its zero reference value) plus 2 times the parallactic angle. Thus, the ratio between the difference and the sum of correlated channels can be fitted with a sinusoidal function and we can retrieve the zero angle of the modulator from its phase. In order to fit this, several observations

[17] Given the limited available space in the BEM, is was impossible to add both a heating system (thermal mat) and a cooler system, thus the BEM temperature is kept above the room temperature.

[18] Throughout this thesis we will always use the convention for the polarisation angle used in HEALPix: $\gamma = \frac{1}{2}\arctan(-U/Q)$.

of Tau A in the same day have been made because we needed the broadest possible coverage of θs. The errors for the polarisation reference angle obtained with this method are of the order of 3º. However, after the improvement of the other aspects of the calibration, the error was reduced to $\approx 1^{o}$ (Génova-Santos, 2015b).

2.6.8 Polar Modulator Absorption

The polar modulator absorbs part of the incoming radiation, thus the amplitude calibration factors depend on the position of the modulator. This was first discovered during the commissioning in one test with one of the modulators spinning in continuous mode: the resulting TOD showed a sinusoidal behaviour in all its channels.

Since all the observations after the commissioning have been done using the modulators in a fixed position (the modulator was moved once a day when the MFI was not observing), a provisional solution was a separate amplitude calibration for each position of the modulators.

However, at the CTOD level, the amplitude calibration factor is obtained combining observations at different positions of the modulators, but the absorption of the modulator is still taken into account with a scaling parameter. This has been calculated separately from the few observations with the modulator spinning in continuous mode. In fact, those observations were fitted with a sinusoidal function, normalised to unity, and the amplitude of the fit is registered in a separate table for each position of the modulators.

2.7 Internal calibration of the MFI

2.7.1 Description

The MFI internal calibration system consists in an antenna (diode hereafter) put in the centre of the secondary mirror in front of the focal plane.

Typically, every 30 s of scientific observations there is a calibration cycle of 1 s during which the diode is switched on and off at the frequency of 20 Hz. The sampling rate is the same as for the scientific data (1 kHz), thus every activation has 50 data samples. The activation curve (Fig. 2.9) shows a small transient at the beginning of the activation and a large transient at its end, which must be removed during the analysis. The signal emitted by the diode is circularly polarised. However, since no horn is exactly at the centre of the focal plane, the signal seen by the MFI horns is partially linearly polarised[19] with a polarisation fraction of the order of 5-10%.

[19]The polarisation measured by a hypothetical central horn would be circularly polarised, but the displacement of the horns with respect to the optical axis causes the polarisation to be

2.7.2 Stability and Warming Curve

Fig. 2.9 shows a stacking of 3540 (177 series of 20) activations of the diode over the observation COSMO3C-130823-1659. One can see that, apart from the peaks just before and after the activations and the following transient period, the diode signal is very stable, with variations typically below 2%.

The analyses done in the laboratory showed that, if its temperature is not kept controlled, the diode presented a warming curve (the first activation has a smaller signal than the other 19, during the same second of activations). For this reason, now the diode is kept at a constant temperature of 40 degrees Celsius[20], which also guarantees the stability over large periods of time.

Fig. 2.10 shows, for the same observation, the activations of the diode organised by activation number: the first point is the average over the first activation of each of the 177 series in the observation, and so on. 20 points are presented since the diode is switched on and off at 20 Hz. The increase in the signal due to the warming of the temperature is visible but not significant, since it is well inside the error bars.

2.7.3 Data Correction

If we call $T_{\rm ins}$ the contribution of the instrument to the system temperature, $T_{\rm sky}$ the temperature of the sky and $T_{\rm diode}$ the temperature of the diode when activated, the signal V that we measure is:

$$V_{\rm off} = G(T_{\rm ins} + T_{\rm sky}) \tag{2.40}$$

$$V_{\rm on} = G(T_{\rm ins} + T_{\rm sky} + T_{\rm diode}) \tag{2.41}$$

where G is the gain of the instrument and the subscripts "on" and "off" indicate if the diode is activated or not. Thus, the difference gives us an estimate of $GT_{\rm diode}$ and, with the assumption that $T_{\rm diode}$ is constant, we can retrieve the gain G, apart from the multiplicative factor $T_{\rm diode}$.

In order to reduce the 1/f noise, we have to minimise the time between the measurements of $V_{\rm on}$ and $V_{\rm off}$. For this reason, both the baseline level and the gain have to be calculated when the diode is switching. The first attempt to calculate the gain used two values: one was the average of the signal when the diode was activated in each activation ("On1" in Fig. 2.11), and the other was average of the signal just after the activation ("Off1" in Fig. 2.11). Then the

elliptical, which means that it has the original circular polarisation combined with a certain amount of linear polarisation, roughly proportional to the amount of the displacement.

[20] It is easy to stabilise the temperature at a value higher than room temperature, because it can be achieved with a heater and a temperature controller. If we wanted to stabilise the temperature at 10°C then we would have had to implement both a heater and a cooler.

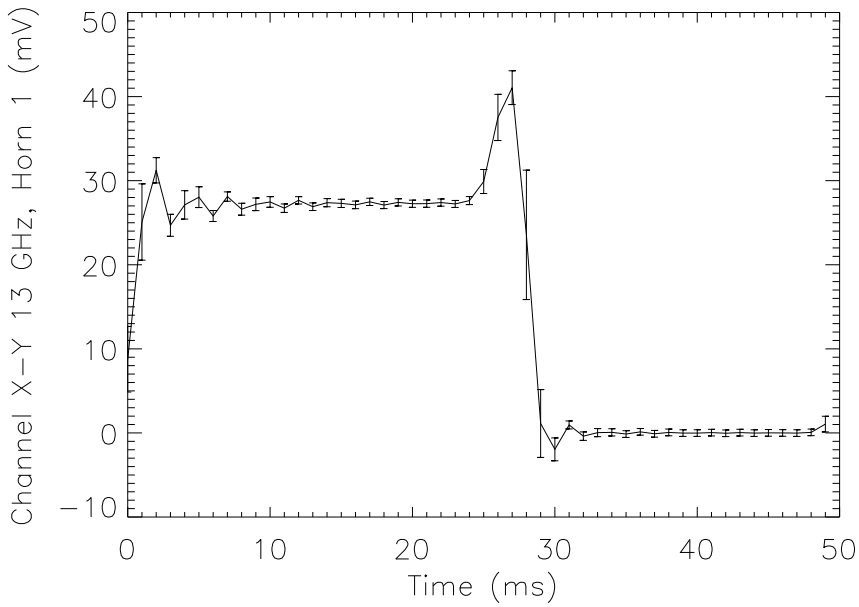

FIGURE 2.9— Average of the diode signal on channel (X-Y) 13 GHz of Horn 1, calculated over 3540 (177 series of 20) activations in observation COSMO3C-130823-1659. The error bar is the standard deviation of each set of activations. The diode signal results extremely stable (the error bars are below 2%). The transient periods at the beginning and at the end of each activation are also visible.

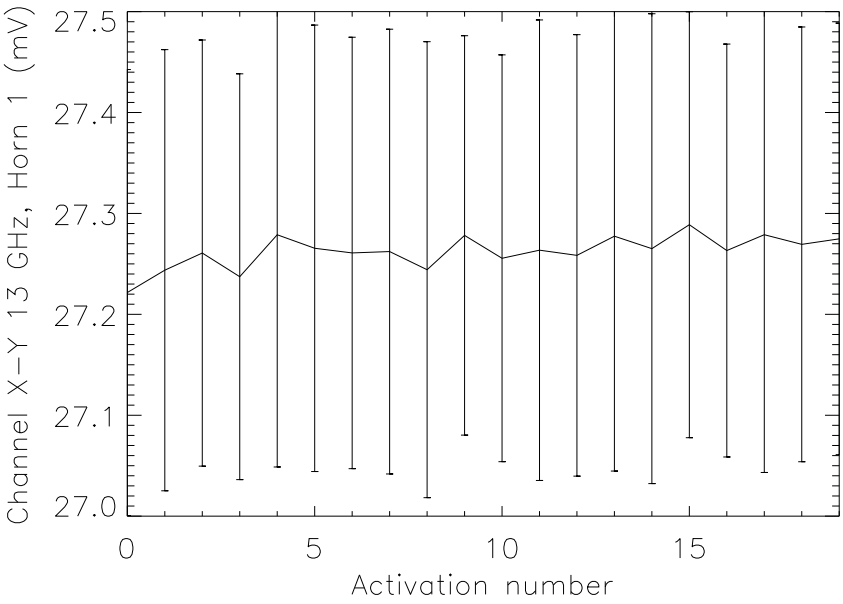

FIGURE 2.10— Warming curve. Observation COSMO3C-130823-1659 (same as Fig. 2.9). Average of the diode activations organised by number of activation (the first point is the average of all the first activations of a series of 20; the second point corresponds to all second activations of the series, and so on). The warming curve is almost not observable and well inside the error bars. This example is from Horn 1, channel (X-Y) at 13 GHz.

baseline level was directly "Off1" and the gain was given by "On1-Off1". The first activation of each series of 20 was excluded to avoid eventual systematics due to the warming curve of the diode, although we saw that this effect is quite negligible. Also the transient periods immediately before and after the activation were excluded (see Fig. 2.11. This method worked adequately in all observations except those characterised by strong gradients in the baseline, such as in nominal mode when observing near the Sun or in the sky dips observations. The solution has been to use two points to trace the baseline level per diode activation: one immediately before it and one immediately after it (in Fig. 2.11 the gain is "On2-Off2", where "Off2" is split before and after the second activation). In this way, we have a value for the gain every 50 ms (1/20 Hz): the $V_{\rm on}$ voltage is calculated averaging the data samples between number 9 and 22, while the baseline level $V_{\rm off}$ is calculated from the average of samples 34 to 40 after the activation and samples 41 to 47 of the previous activation (the first activation is excluded). A summary can be found in Fig. 2.11. A first attempt to correct the data was simply the ratio between the original data and the gain, since the G in Eq. 2.40 cancels out. However, the diode signal is too small compared with the intensity signal and introduces too much noise. For this reason, it is necessary to average the 20 activations per second for several seconds, in order to reduce the noise introduced by the diode itself. As the diode signal is approximately 1/20 of the baseline level, it should be a good choice to have at least 20·20 activation per measure, which is around 10 minutes of observation (we have 20 measurements every 31 s). The tests made showed that periods of about 20 minutes give better results and, considering that the TOD are split in periods of 24 minutes, the final choice is to have one value per TOD file, or every 46·20 activations. This correction did not compensate the gain variations as expected before the commissioning, but it worked very well in removing the day-night effect due to external temperature variations, especially in nominal mode. At the CTOD level, after more years of experience with the MFI, the final choice has been to use a more sophisticated gain model. The gain from the diode is firstly computed in the Cas A observations used to calculate the amplitude calibration factors. Then, a kernel of 30 minutes for low frequency horns and 120 minutes for high frequency horns is used to smooth the gain, after having removed all the outliers. The same smoothing is applied to the gain of each observation and then normalised to the median gain from the Cas A observations. The final value for each data sample in a CTOD (in Kelvin) is then:

$$T_i[K] = A_{\rm mod}(\phi_{\rm mod}) \cdot \langle A_{\text{Volts to Kelvin}} \rangle \cdot \frac{G_{\rm sm}(i)}{\langle G_{\rm sm} \rangle_{\text{Cas A}}} G_{\rm sm}(i) \cdot C_i[V] \qquad (2.42)$$

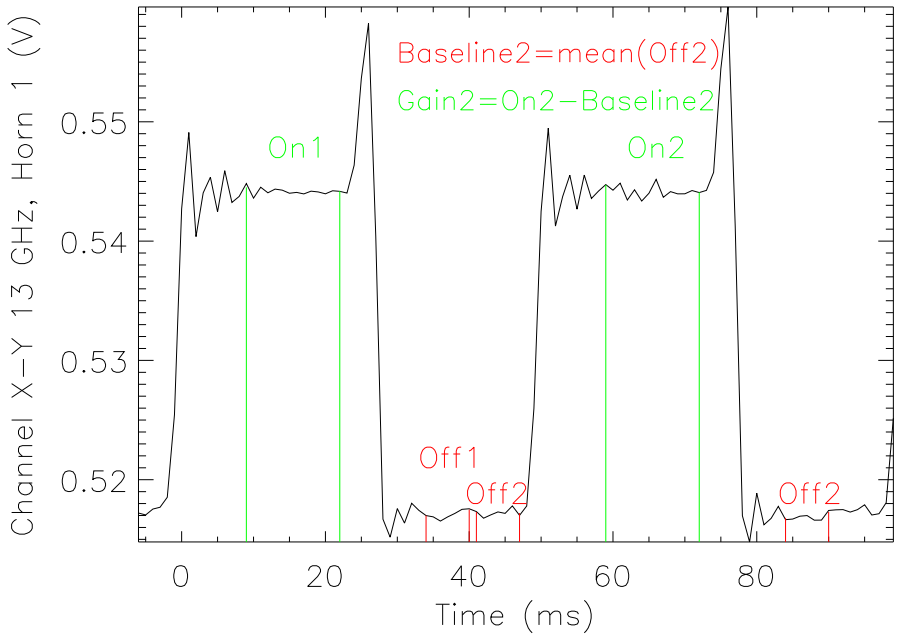

FIGURE 2.11— Example of a single activation of the diode. The data presented are the first activation of the diode signal in channel (X-Y) 13 GHz of Horn 1, observation COSMO3C-130823-1659. The algorithm uses the values within the green intervals to calculate the gain and the values within the red ones to calculate the baseline level. This procedure is repeated 20 times in each second of activation of the diode.The first attempt to calculate the gain only used the "On1" and "Off1" signal, so that Gain1 = On1 - Off1. Later, a split over the baseline signal was used to correct for strong gradients in the baseline, so that the baseline was the average of the two intervals marked "Off2", while the corresponding gain was Gain2, as marked in the figure.

where $A_{\rm mod}(\phi_{\rm mod})$ is the modulator absorption correction factor calculated in subsection 2.6.8 that depends only on the modulator angle position $\phi_{\rm mod}$. $\langle A_{\text{Volts to Kelvin}}\rangle$ is median amplitude correction factor calculated from Cas A observations as explained in subsection 2.6.6. $G_{\rm sm}(i)$ is the smoothed gain calculated with the diode in the observation, i is the sample number on the time ordered domain. $\langle G_{\rm sm}\rangle_{\text{Cas A}}$ represents the median of the smoothed gain calculated in the same Cas A observations used to calculate $\langle A_{\text{Volts to Kelvin}}\rangle$ and $C_i[V]$ is the output of the channel in Volts.

2.8 Observational Status

We conclude the chapter with a brief review of the observational status of the MFI at the moment of writing of this thesis (31 May 2018). The MFI has been observing almost continuously since November 2012 to the date, accumulating almost 24000 hours of observations.

Almost 2000 hours have been dedicated to calibration observations. The main calibrators (Cas A and Tau A) have been observed daily ($\approx$ 3000 22-minutes observations) to achieve a sensitivity of $5\mu{\rm K}/1\,{\rm deg}^2$, while the atmosphere has been characterised with 337 hours of sky-dips observations.

According to the primary scientific objective of the experiment, it observed in nominal mode during 10326 hours, achieving an expected sensitivity[21] of $\approx 18\mu{\rm K}/1\,{\rm deg}^2$, and approximately 6000 hours were dedicated to deep observations of clear regions in the sky, covering an area of 3300 square degrees with an average sensitivity of $9.3\mu{\rm K}/1\,{\rm deg}^2$.

The time dedicated to the secondary objectives, i.e. the characterisation of individual sources, amounts to $\approx$ 5300 hours and allowed to reach a sensitivity of $\approx 10-12\mu{\rm K}/1\,{\rm deg}^2$ in most fields. The best measurements have been achieved a sensitivity of $\approx 3\mu{\rm K}/1\,{\rm deg}^2$ in a small region (30 ${\rm deg}^2$) in the Perseus field with an integration time of 571 hours.

[21] The sensitivities presented in this section are calculated with the total observing time, the area of the regions and the NET (see Eq. (2.1)). They do not take into account that a fraction of the data is discarded or flagged out. For this reason the sensitivities presented in the sources analysed in chapters 4 and 5 are larger.

3

Optics characterisation of the MFI+QT1 system

This chapter presents the characterisation of the beams of the MFI which is mounted on the QUIJOTE first telescope. First, a brief motivation of this work is stated in section 3.1. Then, the different astronomical calibration sources used in this chapter are described. These have been compared to simulations made with standard engineering software (GRASP and CST). Section 3.4 presents the full analysis of the intensity beams, with emphasis on the sidelobes. Finally, the analysis of the polarisation response of horn 1 after the modifications in April 2014 is presented in section 3.5.

3.1 Motivation

In any CMB experiment the beam characterisation is one of the most crucial tasks since it determines the shape of the window function, which has a huge impact in the determination of the angular power spectrum. Thus, an incorrect determination of the beams leads to errors in the determination of the cosmological parameters, and, in particular, in the measurement of the parameter r, which is one of the main objectives of the experiments looking for primordial B-modes. Typically, in intensity the beam must be mapped to less than -30 dB of the peak to achieve 1% accuracy on the angular power spectrum (Page et al., 2003).

Moreover, the foreground removal to get clean CMB maps relies on a comparison of maps at different frequencies, that usually have different beam sizes, thus it is important to have an accurate characterisation of the beams of each

experiment in order to correct the maps and degrade them to a common resolution. In QUIJOTE, the nominal widths for the beams are: 0.9^{o} at 11 and 13 GHz, 0.65^{o} at 17 and 19 GHz, 0.37^{o} at 30 GHz and 0.28^{o} at 40 GHz. A first approach, which is sufficiently accurate in the study of compact sources, is to assume a perfectly Gaussian beam and to characterise it with a single parameter: its Full Width Half Maximum (FWHM). However, cosmological analyses require that the maps are convolved with the exact shape of the beam, in order to take into account large-scale effects and asymmetries of the beams.

Finally, one of the most critical issues in every polarisation experiment is the "leakage". Non-idealities in the instrument can produce a leak from the total intensity signal into the polarisation (I to Q and/or U leakage), and can rotate the polarisation axis away from the nominal one, giving rise to the Q to U or U to Q leakages[1]. In the case of the CMB, the intensity signal is a few orders of magnitude stronger than the polarisation one, thus a detection of the B-modes would be impossible without a very precise characterisation of this systematic.

3.2 Calibration Sources and Special Map-making

In order to characterise the beams, we use several astronomical calibration sources: geostationary satellites, Tau A, Cas A and the Sun. The Moon is not used in this analysis because it is extended[2]. Jupiter was also considered as a calibrator since it is a point source and its emission has been characterised very precisely, however it is not detectable in a single MFI observation since its emission is very diluted by the beam.

The standard map-making procedure of the QUIJOTE pipeline produce maps in sky coordinates (equatorial or Galactic), thus it is not adequate for the beam analysis since it would average out any eventual asymmetry in the beam. In fact, we do not always observe the calibrators at the same local coordinates, thus the source is seen with a different parallactic angle and rotated from an observation to another one. Also, the bending of the telescope changes with the elevation (see subsection 2.6.2) and this can cause a different beam shape. The beam asymmetries can be seen only by making maps in local coordinates (Azimuth and Elevation) with a correction for the movement of the source itself. Therefore, the standard pipeline has been modified with the addition of a new

[1] There is also leakage from Q and/or U to I, but this is usually neglected given that the intensity signal is usually at least an order of magnitude stronger than the polarisation one.

[2] The Sun is also extended, but it is still the best source for the far sidelobes analysis thanks to its brightness and because in this case we are interested at scales much larger ($\approx 60 - 90^{o}$ than the Sun's size

IDL program developed by the author. First, it uses some of the routines of the PM (see subsection 2.6.2) to take into account the non-idealities of the telescope, but removed the conversion from local coordinates to Galactic coordinates. Then, it calculates the positions of the calibration source in local coordinates for each data sample and subtracts it from the coordinates of the telescope, taking into account the correction for the conic projection and the PM. Finally, it used the median-filter map-making (see subsection 2.5) to produce maps from the data stream. The results are maps with the axes orientated as the telescope that are not blurred by the movement of the Earth in the sky.

In the case of the maps of the geostationary satellites, this has not been necessary since they are always located at the same local coordinates, therefore we use directly the encoder readings of the telescope as coordinates. The pointing correction is not necessary since the data are not stacked from different observations. In fact, since each satellite is observed at its elevation and the pointing model depends mostly on the elevation of the telescope, the correction of the pointing model would almost be the same. Then, the maps are made in a reference frame centred in the calibration source with the axes parallel to a AZ-EL sky-reference frame with a simplified (non-destriping) map-making method after the median filter removal (see subsection 2.5).

3.3 Simulations

The simulations of the QT1 beams have been done independently by Bruno Maffei (University of Manchester) and Roger Hoyland (IAC) with different software packages: GRASP[3] and the CST[4] asymptotic solver, respectively. The former is a staple in the industry for precise modelling of reflector antennas and has been used for the simulation of the PLANCK beams (Planck Collaboration et al., 2014b). The latter is one of the possible solvers the CST Microwave Studio offers for the 3D electromagnetic simulation approach. It is based on the Shooting Bouncing Ray method (Ling et al., 1989), which allows to simulate several input rays of different wavelengths, to calculate their reflections over all the surfaces in the telescope, both the mirrors and the tube, up to several times, in order to reconstruct the beam shape and the resulting sidelobes. These sidelobes are usually a consequence of incident rays reflecting over the internal surface of the telescope and this method is one of the best for their estimation. In both cases the simulations have been done using the geometrical parameters from the design of the telescope, including the nominal focal length

[3]The acronym states for "General Responsibility Assignment Software Patterns". More information can be found at the webpage: *http://www.ticra.com/products/software/grasp.*

[4]"Computer Simulation Technology, see the webpage: *https://www.cst.com.*

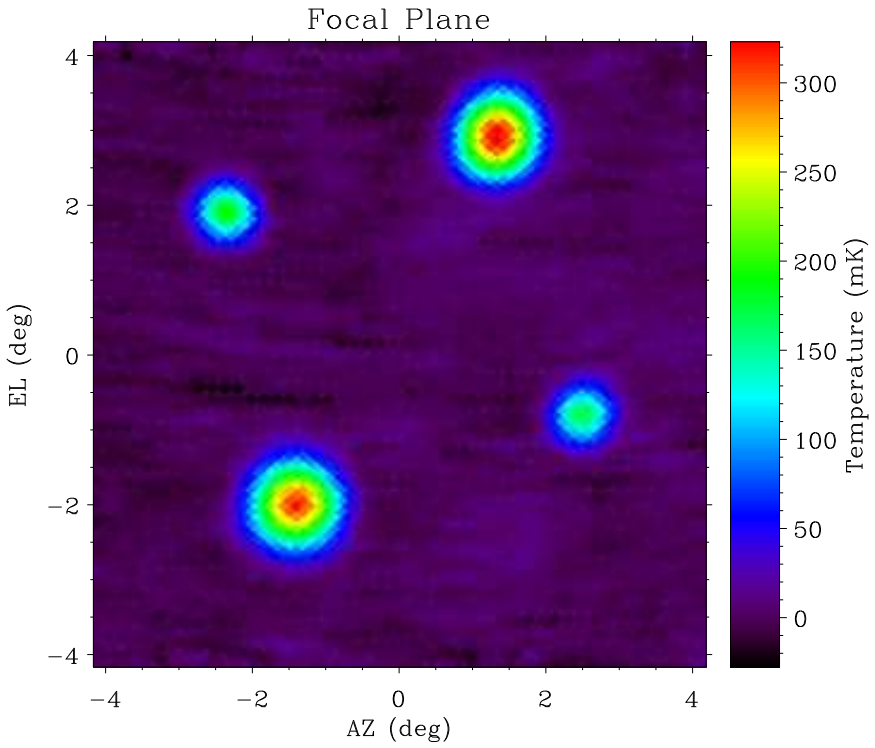

FIGURE 3.1— Map of the beam of the four horns of the MFI with their offset with respect to the centre of the focal plane. The correction for the conical projection has been applied and the source (Cas A) is calibrated in intensity (each channel is multiplied by its conversion factor and the eight channels of each horn are combined to produce this map). The difference between the horns is clearly visible: the FWHM of the low-frequency horns are larger and the detected antenna temperature is higher.

and the nominal position of the horns. There, it has also been assumed that the entire internal surface of the telescope is reflective.

There are four main effects that can induce differences between the simulated maps and the real ones:

1. The surface distortion of the mirror is taken into account only statistically, e.g. we do not have a map of the actual rugosity of the mirror, but only an estimate of its RMS, which is the input of the simulation.

2. The upper inner part of the telescope is made of a material that absorbs microwaves in order to avoid multiple reflections of the incident radiation. Ideally, the incident rays are reflected twice, once in the primary mirror and once in the secondary. However, some of them are reflected only once and some three or four times, which causes the presence of far sidelobes. However, the simulator considers all the inner part of the telescope to be reflective, and limits the number of reflections of each ray to 3.

3. The simulations were done using the nominal values for the positions of the horns and the focal length. While the positions have been confirmed, the PM gave a slightly different focal length for each horn, which is not taken into account since its fit was made after the simulations.

4. The simulation is done in telescope coordinates, with a squared pixelisation[5] which has been converted and projected into the HEALPix format by the author for the sake of comparison with the real data. This process can cause small-scale distortions.

3.4 Intensity Beams

3.4.1 Preliminary Approach

The first-order approximation to model the beam of the QUIJOTE experiment is a bidimensional Gaussian. One of the sources initially used is Cas A since it is a standard calibration source (Weiland et al., 2011), it can be considered as a point source given its size compared the QUIJOTE beam (5.8' against 57' for the low frequencies and 36' at higher frequencies) and it is practically unpolarised (see table 2.4). Therefore, it is very useful to characterise the intensity beams and also allows the construction of maps of individual channels. In fact, intensity beams can be different from the polarisation beams, and the signal

[5]The pixel size for the full sky simulation is 0.25^{o}, however, in case of horn 1, a square region of size 10^{o} around the main beam has been simulated with a higher sampling (pixel size=0.1^{o}).

of a single channel is the sum of the intensity and a combination of Q and U. Thus a map of a polarised source presents a PSF which has the contribution from the intensity beam and a usually smaller contribution from the polarisation beam. The same approach was followed in the characterisation of the beam of the QUIET experiment (Monsalve, 2010, 2012) and BICEP2 (BICEP2 and Keck Array Collaborations et al., 2015). This issue will be carefully examined afterwards. As mentioned in section 2.3 the observing strategy for Cas A provides in a map covering an area of 100 square degrees on the sky. Those observations are typically ~ 22 minutes long, and the resulting map lacks the sufficient sensitivity as to permit a full characterisation of the beam with a single observation, thus two different approaches have been chosen to get a better signal-to-noise ratio (S/N). The first one is to make maps of single observations, fit the 2D-Gaussian to each observation and average the parameters of the fits. This procedure has several advantages:

1. It is independent of the PM of the telescope. The PM produces a correction that depends mostly on the elevation of the observation, but the effect in a single observation is negligible. However, this is not the case if we combine several observations.

2. It is independent of eventual systematic effects that affect the continuum level, like the atmospheric contribution or long-term gain fluctuations. In fact, it is a useful check of systematics, like time drifts of some parameters of the telescope or changes of the beam properties with the elevation.

3. The maps are done in Volts. This way the analysis is independent of the gain calibration of the instrument. Actually, the gain calibration was initially done exactly this way, fitting Gaussians to Cas A observations and calculating the gain factor to get the flux predicted by the WMAP model of Weiland et al. (2011), thus it is crucial to separate these two aspects since they are strongly correlated.

All these advantages are very important especially during the commissioning phase, when the characterisation of other aspects of the calibration, such as the PM or the gain calibration, were also preliminary. Nevertheless, this procedure also presents some disadvantages:

1. It relies completely on a Gaussian parametrisation of the beam, since a more precise characterisation would require a higher S/N.

2. The fits are poorer than the ones on a stacked map.

3. In order to get a better S/N in a single map and to avoid blank pixels, the pixelisation cannot be too small. The beam size is then affected by the larger pixel size of the map.

The second method to get a better S/N ratio with Cas A is a stack of all observations. This could be done only after a complete characterisation of the PM of the first telescope, since observations at different elevations would result in distortions of the beam. However, this approach does not rely on a Gaussian parametrisation of the beam shape. For this reason, we choose to use this method, that will be described in the next section, for the final characterisation of the beams.

3.4.2 Main Beams

The main beams of the MFI have been determined with three different methods:

- Single observations of geostationary satellites, when available.
- Stacking of Cas A observations.
- Simulations.

The use of the geostationary satellites presents several advantages:

- They are point sources: the physical size of the antenna of a satellite is of the order of 1 m, which at the geostationary orbit (35786 km above Earth surface) corresponds to a subtended angle of $\approx 10^{-3}$ arcseconds.
- They are the strongest radio sources in the sky: many satellites saturate the voltage output of the MFI (≈ 11 V) and the brightness temperature measured during a test with the instrument in warm conditions (which results in lower gain and therefore no saturation of the output signal) was ≈ 70000 K at 11 GHz. However, we found that some of them have temperatures several orders of magnitude lower.

We use one satellite per horn and frequency. The choice of the best satellite for each frequency has been done considering all satellites seen in local maps, avoiding non-isolated satellites (the geostationary satellites occupy a stripe of constant declination between -4^o and 0^o with a distance between them of usually 2^o) and choosing the brightest satellite that does not saturate the MFI detectors. However, we did not identify any satellite at 17 GHz, thus the analysis of the data at this frequency has been done with the second method: the stacking of Cas A observations. This method has also been used as a cross-check for

the other horns. However, the latter gave a characterisation of the beam profile down to -25 dB, while with the former we reached the -40 dB at low frequencies.

In both cases, the maps are preliminary fitted with 2D elliptical Gaussians:

$$B(x,y) = A\exp\left(-\frac{1}{2\sigma_\mu^2}[(x-x_0)\cos\chi + (y-y_0)\sin\chi]^2 \right. \\ \left. -\frac{1}{2\sigma_\nu^2}[-(x-x_0)\sin\chi + (y-y_0)\cos\chi]^2\right) \quad (3.1)$$

This allows the simultaneous determination of the centre of the source (x_0, y_0), its amplitude A, which can be used for the calibration of the gain, and to obtain an estimation of the FWHM and ellipticity of the beams from the σ_μ, σ_ν parameters (σ_μ is measured along the major axis and σ_ν along the minor one; χ is the rotation angle between this major axis and the horizontal axis). Table 3.1 shows all these parameters for the four horns. Table 3.2 shows the same parameters for the eight channels of horn 1 separately. The ellipticities are very close to 1 (the minimum value from satellites observations is 0.92, and 0.87 in Cas A observations), which assess the circularity of the beam. For this reason, we can use the the radial-profile approximation by defining:

$$b_r(\theta) = \frac{\int d\phi B(\theta,\phi)}{A\int d\phi} \quad (3.2)$$

in which θ and ϕ are respectively the radial and polar angles of the previous map in polar coordinates centred in the source. Note that we normalise the amplitude to unity by dividing by A. The main advantages of this procedure are that we gain signal to noise by compressing the information from 2D to 1D and that we average the small ellipticity coming from the source itself (however this should be negligible since we see it as a point source at our resolution). The profiles are then characterised by a Gaussian fit to control the compatibility with the previous analysis. The two plots in Fig. 3.2 show respectively the radial profiles of the four horns and of the four channels at the same frequency of horn 1. The big bump at 3.5º is produced by another satellite, with a much lower brightness temperature. Since we are only interested in the main beam in this section this satellite has not been masked. The analysis of the near sidelobes is done in section 3.4.3 with another approach that allows us to reach levels of -70 dB.

For the sake of comparison we provide also some additional parameters that are often used in other experiments: the solid angle Ω_{MB} which has been computed directly on the 2D map of the satellites integrating out to the first sidelobe

Horn	Freq (GHz)	CST Simulation FWHM (deg)	e	Sat. Obs. FWHM (deg)	e	Cas A Obs. FWHM (deg)	e	Ω_{MB} (msr)	$\eta_{\rm B}$	G_m (dBi)	Γ (μK/Jy)
1	11	0.90	0.96	0.89	0.99	0.91	0.97	0.28	0.93	46.49	916.29
1	13	0.91	0.98	0.89	0.99	0.88	0.99	0.28	0.95	46.47	696.78
3	11	0.89	1.00	0.84	0.93	0.84	0.97	0.25	0.95	46.94	1029.31
3	13	0.90	0.96	0.85	0.92	0.82	0.97	0.26	0.96	46.91	765.81
2	17	0.63	0.97	—	—	0.61	0.95	0.13	0.97	49.78	877.95
2	19	0.64	0.97	0.63	0.98	0.54	0.89	0.16	0.98	48.84	566.20
4	17	0.62	0.97	—	—	0.49	0.93	0.12	0.90	50.28	966.89
4	19	0.64	0.96	0.65	0.97	0.47	0.87	0.15	0.92	49.31	611.81

TABLE 3.1— Full Width Half Maximum (FWHM) and ellipticities ($e = \sigma_\nu/\sigma_\mu$) of the beams of each horn and frequency calculated with 2D Gaussian fits to the maps of Cas A or geostationary satellites. The results have been obtained with the CST simulations of the beam, the raster scans of satellites (note that there was not a suitable satellite at 17 GHz) and the combined map of the Cas A rasters. The main beam solid angle (Ω_{MB}) is calculated from the 2-D maps of the satellite, when available, and from the 2-D stacked map of Cas A otherwise (17 GHz). The gain (G_m) and the sensitivity (Γ) have been computed from Ω_{MB} for sake of comparison with other experiments. The beam efficiency $\eta_{\rm B}$ has been calculated from the simulations. See text for details. The low values of the FWHM of Cas A in horn 4 can be explained by the lower S/N of the maps used.

(differences between this value and the one calculated as $\Omega'_{MB} = 2\pi\sigma^2$ are indicators of non-Gaussianity), the telescope forward gain $G_m = 10\log_{10}(\frac{4\pi}{\Omega_{MB}})$ and the telescope sensitivity (conversion factor between flux density and antenna temperature):

$$\Gamma\left[\frac{\mu\mathrm{K}}{\mathrm{Jy}}\right] = \frac{10^{-20}c^2}{2k_b\nu_e^2\Omega_{MB}} \tag{3.3}$$

where c and k_b are the speed of light and the Boltzmann constant respectively, while ν_e is the effective observing frequency which was computed from the bandpasses measured in the laboratory (see subsection 2.6.3). The beam efficiency η_B is defined as $\eta_\mathrm{B} = \Omega_{MB}/\Omega_A$, where Ω_A is the full solid angle of the antenna. Since we could not calculate it on the maps, because they are truncated at a few degrees from the source, we computed Ω_A in the simulation and, for consistency, also the Ω_{MB} calculated in the simulation was used in this case.

There are small discrepancies between the values in the tables 3.1 and 3.2: the FWHM obtained from the simulations are very similar to the nominal ones (see table 2.1, while the ones measured with the satellites are generally smaller. One effect that could explain this is the bandwidth: the signal emitted by the satellites has a very narrow spectrum, while each band of the MFI is about 2 GHz. The beam shape changes with the frequency, since it is partially determined by how the incident rays bounce inside the telescope, thus the beam calculated from Cas A observations is weighted by the bandpass, while the beam measured from the satellites is given only by the beam at its emission frequency. The FWHMs measured with Cas A present a higher dispersion, due to the lower S/N. Also, the data of Cas A measured with horn 4 had a much lower S/N[6], which caused a large discrepancy between the FWHM obtained with this method and the FWHM obtained with the simulation. Also, we note that there is almost no variation between the FWHM of the same horn, although the frequency changes. This is because the system is under-illuminated: the solid angle subtended by the mirrors is broader than the solid angle subtended by the horn. This gives a very high beam efficiency (the minimum η_B is 0.9 in horn 4, 17 GHz), which combined with the ellipticities very close to 1 proves the exceptional optical quality of the MFI compared to other CMB experiments.

3.4.3 Near Sidelobes

The study of the near sidelobes requires a strong point source as calibrator since they are expected to be below the level of -40 dB. Since the antenna temperature of Cas A at 11 GHz is of the order of 300 mK, the first sidelobe

[6]In subsection 2.2.3 we explained that the amplifier of horn 4 was of lower quality and had to be replaced.

Channel	Freq (GHz)	CST Simulation FWHM (deg)	e	Sat. Obs. FWHM (deg)	e	Cas A Obs. FWHM (deg)	e	Ω_{MB} (msr)	$\eta_{\rm B}$	G_m (dBi)	Γ (μK/Jy)
X-Y	11	0.91	0.98	0.88	1.00	0.89	0.95	0.28	0.95	46.47	926.29
X	11	0.91	0.95	0.88	0.99	0.91	0.96	0.29	0.95	46.41	889.96
Y	11	0.91	0.95	0.90	0.97	0.94	0.98	0.28	0.95	46.49	917.60
X+Y	11	0.91	0.98	0.89	0.99	0.91	0.97	0.29	0.95	46.43	898.64
X-Y	13	0.90	0.96	0.89	0.98	0.86	0.97	0.29	0.93	46.43	686.05
X	13	0.90	0.97	0.89	0.99	0.87	0.98	0.28	0.93	46.49	698.21
Y	13	0.90	0.97	0.89	1.00	0.91	0.99	0.28	0.93	46.50	708.78
X+Y	13	0.90	0.96	0.90	0.98	0.87	0.99	0.29	0.93	46.44	694.08

TABLE 3.2— FWHM and ellipticities ($e = \sigma_\nu/\sigma_\mu$) of the beams of each channel of horn 1, calculated with 2D Gaussian fits to the maps of geostationary satellites. The main beam solid angle (Ω_{MB}) is calculated from the 2-D maps of the satellite. The gain (G_m) and the sensitivity (Γ) have been computed from Ω_{MB} for sake of comparison with other experiments. The beam efficiency $\eta_{\rm B}$ has been calculated from the simulations. See text for details.

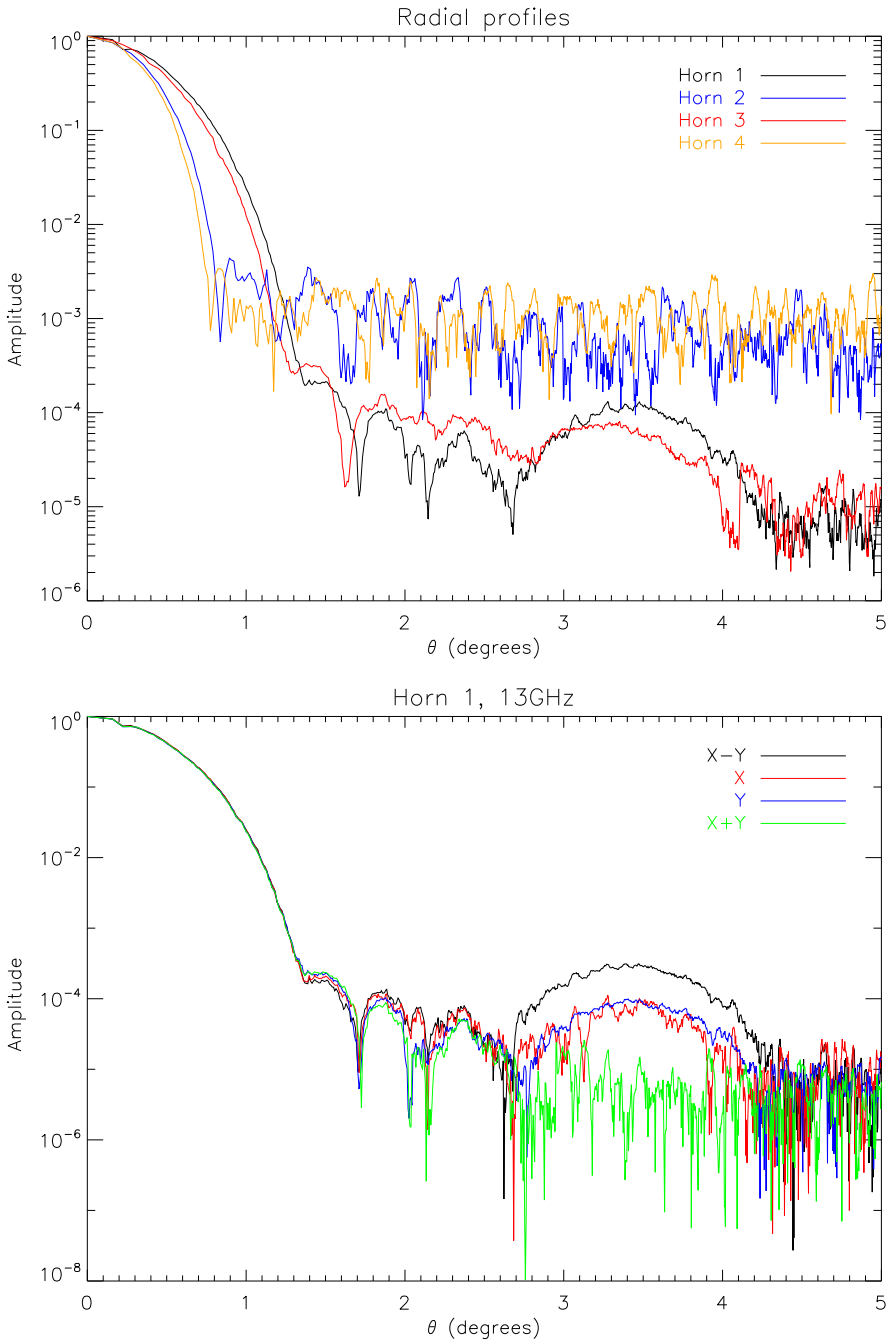

FIGURE 3.2— Top: Beam radial profiles of the four horns at 13 and 19 GHz (sum of correlated channels). Note that higher frequencies correspond to narrower and noisier beam shapes. Bottom: Beam radial profiles of single channels of horn 1, 13 GHz. There is no relevant difference in the observed properties of the different channels. The big bump centred in 3.5 °is due to a nearby, very weak, satellite.

should be at the level of 30 μK. The Sun and the Moon are sufficiently bright to have detectable sidelobes but they are not adequate since they are extended, thus their main beams may overlap with the first sidelobes. For those reasons the best calibration sources for the study of the near sidelobes are geostationary satellites, or we could also resort to simulations.

In normal conditions, the signal from the satellites usually saturates and does not permit the correct reconstruction of the shape of the beam, thus it does not allow the direct comparison between the main beam and the near sidelobes. However, the gains of the receiver strongly depend on the MFI cryostat temperature: the amplification is lower if the temperature is higher. For this reason, we used a local map observation made with the cryostat at room-temperature (Map 1) to determine the main beam of the brightest satellite out to 1.3^{o}, and a normal local map (Map 2) to measure the sidelobes out to 10^{o}. Map 2 was calibrated with the standard MFI pipeline, but we needed the conversion factors from voltage to temperature of Map 1 in order to combine it with Map 2. The calibration has been done with the Sun, which has a brightness temperature of $\approx 10^4$ K in the frequency range between 10 and 20 GHz (Ho et al., 2008; Shimabukuro & Stacey, 1968; Lo & Lonc, 1986; Keller & Krucker, 2004). A correction factor of $\Omega_{\rm Sun}/\Omega_{\rm MB}$ has been used to account for the solid angle subtended by the Sun and the dilution factor of the beam. The combination of the two maps allowed us to reach an unprecedented level of -70 dB.

Fig. 3.3 (bottom) shows the resulting map for the X+Y channel of horn 1, 13 GHz. The first near sidelobes are clearly visible. It is important to note that they are clearly not radially symmetric. This is due to the offset of the horn with respect to the centre of the focal plane. In fact, opposite horns show this feature on opposite sides with respect to the source. Apart from the stripes in the azimuth direction of the data, which are caused by the median filter in the map-making, the simulation agrees remarkably well with the data, showing the first sidelobes at a level of -35 dB

3.4.4 Far Sidelobes

The analysis on the far sidelobes is done taking the Sun as a calibration source following the same idea that was applied to the QUIET experiment (Bischoff et al., 2013). This is because it would have been very complicated to separate the effects of all the satellites on large scales, since each feature of the map will be the sum of all the sidelobes of each satellite, while the fact that the Sun is an extended source in the QUIJOTE beams can be safely ignored some degrees away from its position.

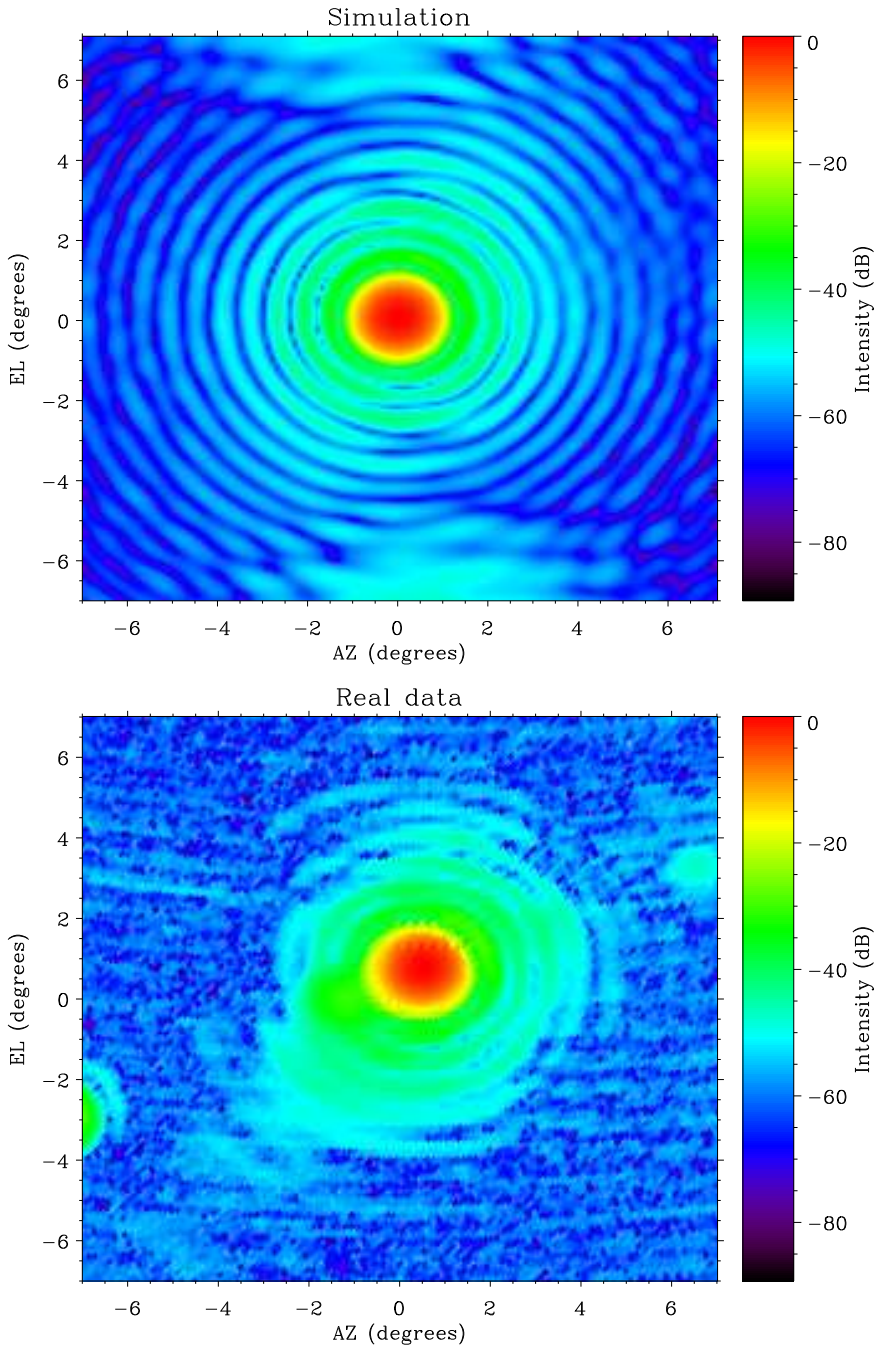

FIGURE 3.3— Map of the near sidelobes of a simulation (top) and of the brightest artificial satellite (bottom). The latter has been obtained combining two local maps, one with the cryostat at room temperature in order to avoid saturation effects in the shape of the main beam, and one with the cold cryostat to measure accurately the first sidelobes. The calibration of the warm cryostat map has been done with the Sun. See text for details.

The procedure we used to estimate the far sidelobes was the following:

1. We use observations in nominal mode in position A of the modulator at elevation between 65º and 85º in order to maximise the sky coverage. The presence of the satellites is therefore avoided (all the satellites have elevation below 58º) and the far sidelobes of the satellites are diluted since moving in the reference frame of the Sun. The total amount of data used for this analysis was 383 hours. The range of elevations was given mainly by the Sun movements.

2. We computed the Sun position for each time sample of these observations, and we made maps in local coordinates centred in the Sun position with the same algorithm used for the main beam analysis, correcting for both the pointing model and the Earth movement. Since the maps covered a large fraction of the sky, we keep spherical coordinates instead of applying the conic projection.

3. Finally, the map was rotated in order to show the Sun at the North Pole. This allowed a better visualisation of the sidelobes at 90º, which would have been distorted in a normal projection. The same has been done with the CST simulation.

The results are shown in Fig. 3.4. The brightest sidelobe, at 90º from the source is caused by the spillover, as in the QUIET experiment. This has been confirmed also for QUIJOTE with simulations: if we reduce the number of permitted reflections on the internal surface of the telescope, the far sidelobes are reduced as well. The natural solution to reduce these reflections was to extend the telescope with a radiation shield as it had been done in QUIET (Bischoff et al., 2013). Therefore, an extended shield of 80 cm was added to the QT1 in April 2014. Fig. 3.5 shows the QT1 after the installation of this extended shield, while the QT2 appears without such extension. Since the QT2 is observing at higher frequencies, it is not affected by spillovers from the geostationary satellites, which emit mainly in the 10-14 GHz range.

One possible method to assess the level of contamination introduced by far sidelobes from geostationary satellites is to make a stack in azimuth of the data: since the satellites do not move, their sidelobes remain in the same position, while the sky signal is diluted because of Earth rotation. This approach has been implemented by F. Poidevin (IAC) in parallel with this thesis. He made a stack in azimuth in bins of 5º for every elevation in the nominal maps and for every modulator position, before and after the installation of the extended shield. While the stacks before April 2014 present a bump in the signal between

AZ=20° and AZ=30°, this feature was not detected after the modification. An upper limit was established at approximately -10 dB with respect to the peak of the bump seen before. The effect is clearly visible considering local maps before and after the installation (Fig. 3.6), in which the interference pattern is clearly visible in the left panel (the red spot in the bottom left and near the centre) but not in the right panel.

3.4.5 Window Functions

The window function, w_l, of an experiment at zero lag (Page et al., 2003) represents the response of the instrument at each angular scale. Mathematically, it can be expressed directly as the second power of the Legendre transformation of the transfer function of the beam. In the case of the radial profile analysis, the beam transfer function, b_l, is:

$$b_l = \sqrt{w_l} = \frac{2\pi}{\Omega_A} \int b_r(\theta) P_l(\cos\theta) d(\cos\theta) \tag{3.4}$$

where P_l corresponds to the Legendre polynomial of order l. In the case of a perfect Gaussian beam this leads to the expression $w_l = \exp(-l(l+1)\sigma^2)$.

In this thesis we calculated the window function of horn 1 of the MFI using 3 different methods:

1. We applied Eq. (3.4) over the radial-profiles $b_r(\theta)$ truncated at $\theta = 2.5°$ ("Direct fit" in Fig. 3.7) to avoid contamination from other satellites and from the low S/N part of the profile.

2. We fitted the radial-profiles with a Fourier transform of order 50 and applied Eq. (3.4) to the fitted data. This further reduced the noise and permitted to compute $b_r(\theta)$ up to a larger radius. The result of this procedure is shown in Fig. 3.7, red line ("Fourier fit").

3. We perform a 2D harmonic analysis of the simulation with the $ianafast$ routine[7] of HEALPix. This method cannot be applied to real data from a ground experiment since it requires full sky coverage, but presents other advantages: it does not truncate the data and does not assumes a perfect symmetry in the beam. The Blue line ("Simulation") in Fig. 3.7 shows the window function calculated with this method.

Despite the differences in the methods used for the calculations, the simulation agrees remarkably well with the data, being the difference between them

[7] See *https://healpix.jpl.nasa.gov/html/facilitiesnode7.htm* for details.

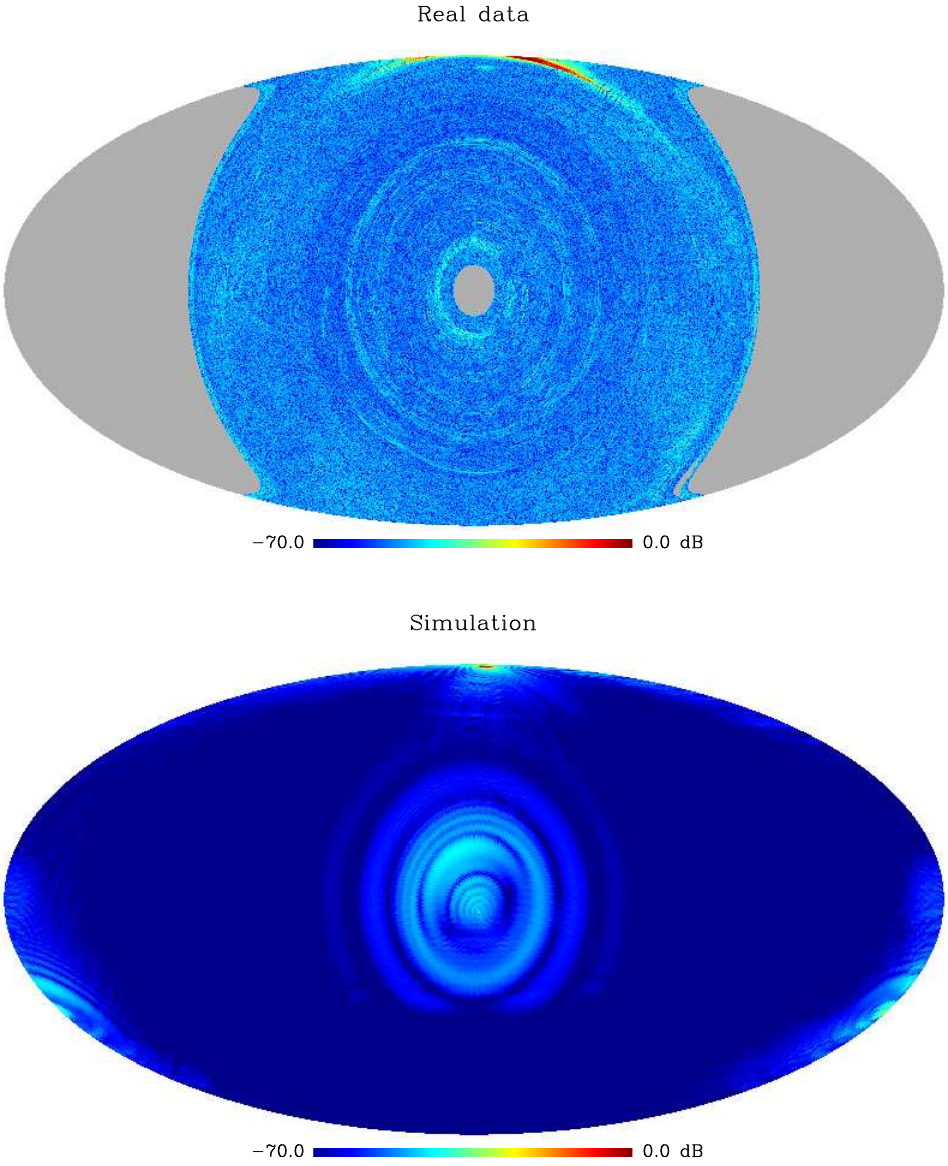

FIGURE 3.4— Map of the sidelobes of the Sun in the simulation and in real data. This has been obtained combining 383 hours of Nominal mode observations centred in the Sun, at elevations between 65° and 85° to avoid the contamination from the geostationary satellites. The signal from the sky and from the sidelobes of the satellites is averaged out with the Sun movements.

FIGURE 3.5— Photograph of the QT1 and QT2. QT1 on the left is equipped with the extended shield that avoids the spillover which causes far sidelobes from the strong astronomical sources, especially the geostationary satellites. On the contrary, the QT2 is not expected to be affected since it observes at higher frequency (30 and 40 GHz), where no geostationary satellites emission is expected. QT1 was an exact replica of QT2 before April 2014, when the shield was installed.

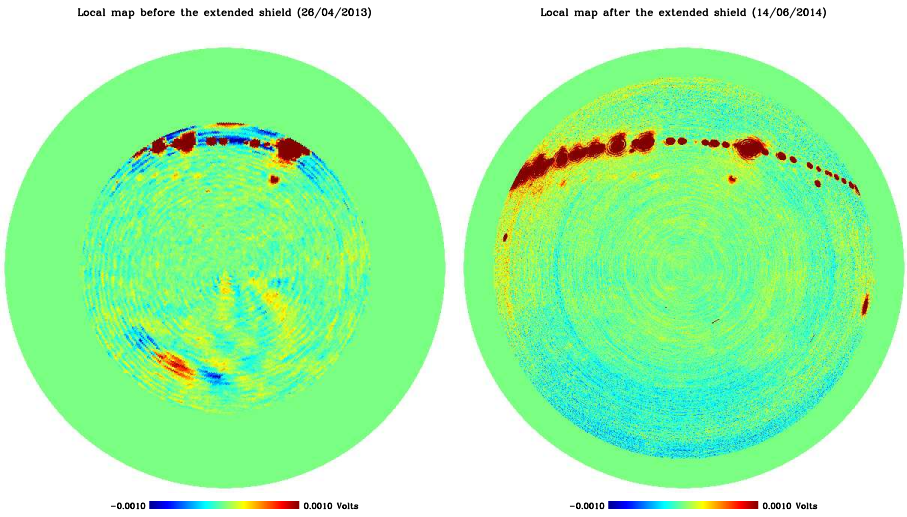

FIGURE 3.6— Left panel: local map observation performed on the 26 April 2013 (before the installation of the extended shield). Right panel: local map observation performed on the 14 June 2014 (after the installation of the extended shield). The maps have the same scale in Volts (from -1 mV to 1 mV) in order to show the interference pattern (bottom part of the left panel). This is not visible in the right panel because the extended shield prevents the signal from off-line of sight sources to enter the telescope. The satellites band is visible in the upper side of both panels and the brightest satellites reach the saturation level of the detector (11.2 V).

less than 1.1%, while the Fourier fit gives a difference with the unfitted data at 0.1% level. It is important to note that, with the first two methods, the window function is calculated from truncated data, thus we lose the information at large angular scales. However, since the brightest radio sources (except the Sun and the Moon) have a temperature of 300 mK, their contribution to the near a dn to the far sidelobes would be of the order of 30 μK and 30 nK respectively. If we consider that the polarisation is never larger than 10%, and we correct for bright sources, we have a contribution of 3 nK coming from the far sidelobes which is relatively small in comparison with the recombination bump at $r = 0.1$ which peaks at 100 nK (see Fig.1.12).

The window functions of horns 2, 3 and 4 are calculated with the direct method and after the Fourier fit. They present a similar behaviour to the one presented for horn 1. The simulations of the beams for these horns were made at a coarser pixelisation, which affected the calculation of the window funtion at high l.

For cosmological analyses, we recommend the window function calculated with the Fourier fit, since it filters out eventual noise at high l, although the different methods give very similar results. However, the window functions calculated with either of these methods take into account only the beam of the instrument. Other effects, such as the map-making process or the masks used to remove contamination from strong sources, are not taken into account, and this will cause a significative reduction of the w_l at low l.

3.5 Polarisation Beams

The polarisation beams are studied following the Müller matrices formalism, with a procedure similar to the one applied in Monsalve (2010) for the QUIET experiment. However, our method differs on the choice of the calibrators since we did not have the possibility to use a laboratory calibration source, but only celestial sources. This implied that we had to combine data from different calibrators to get different polarisation states and that we had to deal with longer observations in order to achieve a sufficient S/N level.

3.5.1 Jones and Müller Matrices

The effect of any optical device can be described by one 2x2 matrix specifying how the complex components of the electric field change (Trujillo-Bueno et al., 2002; O'Dea et al., 2007). This matrix is called Jones matrix. For example, the effect of an ideal polariser oriented along the x-axis is given by

$$\begin{bmatrix} \epsilon_1' \\ \epsilon_2' \end{bmatrix} = e^{i\phi} \begin{bmatrix} 1 & 0 \\ 0 & 0 \end{bmatrix} \begin{bmatrix} \epsilon_1 \\ \epsilon_2 \end{bmatrix} \tag{3.5}$$

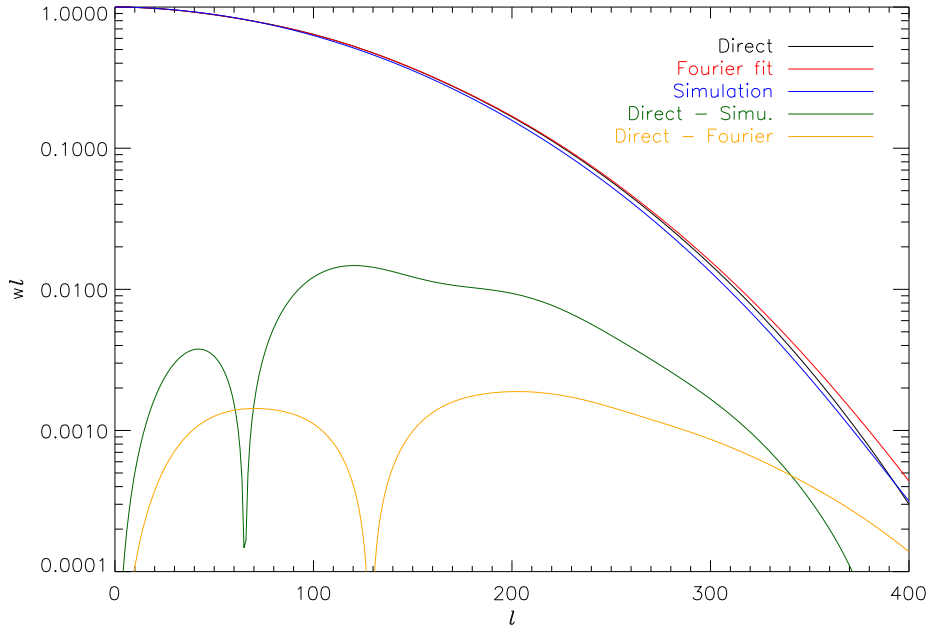

FIGURE 3.7— Window functions of channel 1 of horn 3 computed with the three methods: direct computation over the data (black line), computation over a Fourier fit of the first 50 harmonics (red line) and comparison with the simulation (blue line). The green line shows the absolute value of the difference between the direct calculation and the simulation, while the orange line represents the absolute value of the difference between the direct calculation and the Fourier fit. The differences become important in percentage at high l but they do not surpass 1.1%

where the subscripts represent the observed field. Obviously, in the receiving system of the instrument there is a train of components and the total Jones matrix is simply given by the matrix product of the individual Jones matrices.

Sometimes, we are interested in the electromagnetic tensor:

$$\langle E_i^* E_j \rangle \equiv \begin{pmatrix} E_{\mathrm{A,co}} & E_{\mathrm{A,cross}} \\ E_{\mathrm{B,cross}} & E_{\mathrm{B,co}} \end{pmatrix} = \frac{1}{2} \begin{pmatrix} T+Q & U+iV \\ U-iV & T-Q \end{pmatrix} \tag{3.6}$$

In this case, we can use formula (12) of O'Dea et al. (2007):

$$\begin{pmatrix} T+Q & U+iV \\ U-iV & T-Q \end{pmatrix}' = J \begin{pmatrix} T+Q & U+iV \\ U-iV & T-Q \end{pmatrix} J^{*T} \tag{3.7}$$

where J is the Jones matrix. This can be easily proven with some algebra.

Another way to represent the action of an optical device over a radiation field is the Müller matrix. This allows us to see the effect of the device directly on the Stokes parameters. In fact one can define a Stokes 4-component vector as $S_T = (I, Q, U, V)$ and look for an equation like $S' = MS$ where M is a 4x4 matrix. The result, which has been proven with Mathematica and analytically, is

$$M = \frac{1}{2} \begin{bmatrix} a^*a + b^*b + c^*c + d^*d & a^*a - b^*b + c^*c - d^*d & 2\mathrm{Re}(a^*b + c^*d) & 2\mathrm{Im}(a^*b + c^*d) \\ a^*a + b^*b - c^*c - d^*d & a^*a - b^*b - c^*c + d^*d & 2\mathrm{Re}(a^*b - c^*d) & 2\mathrm{Im}(a^*b - c^*d) \\ 2\mathrm{Re}(a^*c + b^*d) & 2\mathrm{Re}(a^*c - b^*d) & 2\mathrm{Re}(a^*d + b^*c) & 2\mathrm{Im}(a^*d - b^*c) \\ -2\mathrm{Im}(a^*c + b^*d) & -2\mathrm{Im}(a^*c - b^*d) & -2\mathrm{Im}(a^*d + b^*c) & 2\mathrm{Re}(a^*d - b^*c) \end{bmatrix} \tag{3.8}$$

where $J = \begin{bmatrix} a & b \\ c & d \end{bmatrix}$ is a generic Jones matrix. It can be easily demonstrated that the Müller matrix satisfies the "train property" as the Jones one does, and that the Eq. (1.18) is valid for S' if and only if it is valid for S, keeping the equal sign if it is the case.

3.5.2 Case of Horn 1

The equations that give the Stokes parameters for horn 1 after the modifications in April 2014 as a function of the 4 channels are the following (see also Eqs. 2.9-2.12):

$$d_I = \tfrac{1}{2}[C_{X+Y}G_{X+Y} + C_{X-Y}G_{X-Y} + C_X G_X + C_Y G_Y] \tag{3.9}$$

$$d_Q = (C_{X+Y}G_{X+Y} - C_{X-Y}G_{X-Y})\sin 4\theta + (C_X G_X - C_Y G_Y)\cos 4\theta \tag{3.10}$$

$$d_U = (C_{X+Y}G_{X+Y} - C_{X-Y}G_{X-Y})\cos 4\theta - (C_X G_X - C_Y G_Y)\sin 4\theta \tag{3.11}$$

where we explicitly put the gains G for each channel and the difference θ between the modulator position and its zero reference position[8]. This difference is fixed for horn 1 but not zero. The parameters d_I, d_Q, d_U are the Stokes parameters as they enter the instrument, that is after passing the optic of the telescope. This is characterised by the Müller matrix with the equation:

$$\begin{pmatrix} I_m \\ Q_m \\ U_m \end{pmatrix} = \begin{pmatrix} M_{II} & M_{QI} & M_{UI} \\ M_{IQ} & M_{QQ} & M_{UQ} \\ M_{IU} & M_{QU} & M_{UU} \end{pmatrix} \begin{pmatrix} I_0 \\ Q_0 \\ U_0 \end{pmatrix} = \\ \begin{pmatrix} M_{II} & M_{QI} & M_{UI} \\ M_{IQ} & M_{QQ} & M_{UQ} \\ M_{IU} & M_{QU} & M_{UU} \end{pmatrix} \begin{pmatrix} 1 & 0 & 0 \\ 0 & \cos 2\gamma & -\sin 2\gamma \\ 0 & \sin 2\gamma & \cos 2\gamma \end{pmatrix} \begin{pmatrix} I_S \\ Q_S \\ U_S \end{pmatrix} \quad (3.12)$$

where we have introduced the Stokes parameters I_S, Q_S, U_S of the source used as calibrator and the parallactic angle γ to rotate the source into the reference system of the telescope (Stokes parameters I_0, Q_0, U_0).

Following the same formalism as IN QUIET (Monsalve, 2010), we introduce the polarisation fraction p and polarisation angle γ_s of the source. The explicit equations are:

$$\frac{d_I}{I_S} = M_{II} + pM_{QI}\cos(2\gamma - 2\gamma_s) + pM_{UI}\sin(2\gamma - 2\gamma_s) \quad (3.13)$$

$$\frac{d_Q}{I_S} = M_{IQ} + pM_{QQ}\cos(2\gamma - 2\gamma_s) + pM_{UQ}\sin(2\gamma - 2\gamma_s) \quad (3.14)$$

$$\frac{d_U}{I_S} = M_{IU} + pM_{QU}\cos(2\gamma - 2\gamma_s) + pM_{UU}\sin(2\gamma - 2\gamma_s) \quad (3.15)$$

For each Stokes parameter, we combine Eqs. 3.9-3.11 with Eqs. 3.13-3.15. In the case of intensity (for the sake of simplicity we explain it just for the second term), we get:

$$I_S^{-1} \cdot [(C_{x+y}G_{x+y} - C_{x-y}G_{x-y})\sin 4\theta + (C_xG_x - C_yG_y)\cos 4\theta] = \\ = M_{IQ} + pM_{QQ}\cos(2\gamma - 2\gamma_s) + pM_{UQ}\sin(2\gamma - 2\gamma_s) + n \quad (3.16)$$

where we introduce a white noise component n for convenience. The left side of the previous equation depends only on the data of the instrument and the right side contains only the second line of the Müller matrix and the noise as

[8]The parallactic angle γ is not taken into account at this stage since the Stokes parameters are refereed to local (AZ-EL) coordinates: these equations represent how to translate a signal coming from just outside the telescope into the signal seen after the instrument.

variables. The equation holds for each data sample, and the Müller matrix terms depend only on the pointing coordinates of the telescope with respect to the source. Therefore if we group all data that lie in the same pixel, we can obtain the components of the Müller matrix as the free parameters of a model described by Eq. (3.16). This is done analytically with a χ^2 minimisation as explained in the Monsalve's thesis (Monsalve, 2012).

However, we cannot use geostationary satellites as calibrators in this case because we need very precise information about the intensity and polarisation of the source. Moreover, we need at least three independent sets of data because we want to retrieve three parameters (M_{IQ}, M_{QQ}, M_{UQ}). An unpolarised source such as Cas A gives only one set of data, since the dependence on the parallactic angle is lost because $p = 0$. On the other hand, a polarised source such as Tau A gives two sets of data because the parallactic angles vary very little between all observations before culmination and changes rapidly to another value after the culmination. If we could change the polarisation of the source, or if the parallactic angles were uniformly distributed, this would not be necessary. In fact, the polarisation calibration of the TGI is done in the laboratory with a rotating polarised antenna (a spare pixel switched on) and in the QUIET experiment it is obtained by rotating a emitting wire. In the case of the MFI, the same effect cannot be obtained rotating the polar modulator since it affects only the left side of Eq. (3.16), being independent of the free parameters of the model.

3.5.3 Results and Discussion

Fig. 3.8 shows the Müller matrix obtained applying the procedure described above to 27.2 hours of Tau A and 27.6 hours of Cas A observations performed between June and October 2014. All observations are kept in local coordinates, have been corrected with the PM and with a median filter of 20 s. The important features are the following:

1. The diagonal terms (II, QQ, UU) are represented by monopoles, and their amplitudes are close to 1, especially for the polarisation terms. This is reasonable, as the gain factors are calculated channel by channel to improve the polarisation calibration: if we would have calibrated the sum of channels, we would have M_{II} closer to one instead. Also, the profiles are almost circular, which is as an additional confirmation of the ellipticities close to 1 in the main beam analysis and of the validity of the radial profile method to calculate the FWHM.

2. The second and third panels of the first column represent the leakages

from the intensity signal to Q and U respectively. These are the main contamination to the polarisation angular power spectrum since the intensity signal is some orders of magnitude stronger than the polarisation one. The monopole is of the order of 0.8%, which is very good compared to other CMB experiments (the leakage level of the Planck LFI is about 2% at 28 GHz), while the largest contribution comes from the dipole. In QUIET the dipole contribution comes mainly from a different pointing along the two axes of the polarisation detectors, but this is not the case of the MFI. Finally, we note that the orientation of the dipoles is rotated by 45º, as expected with the operative definition of the Stokes parameters.

3. The panels QU and UQ represent the leakages from Q to U and vice-versa. These are usually caused by the non-perpendicularities between one of the two arms of the OMT. The U-to-Q leakage is below the noise of the map, therefore compatible with zero, but the Q-to-U leakage is not.

4. The first line (panels QI and UI) represents the contribution from polarisation to intensity. Although this seems huge, it is actually not relevant since QUIJOTE is specifically designed to measure polarisation and since the polarised signal is several orders of magnitude lower than the intensity one. Moreover, for this same reason, it is difficult to estimate properly the contribution of the polarisation into the intensity signal: if we have a 2% error in intensity, and the polarised signal is also a 2% of the intensity, we could claim that the whole intensity error comes from leakage from polarisation and this would correspond to a QI or UI close to 1.

For the other horns, the same procedure could be applied since we can obtain simultaneously Q and U using the four channels at each frequency. However, the uncorrelated channels are strongly affected by 1/f noise, which prevents a good simultaneous measurement of the Q and U Stokes parameters. Therefore, although the same procedure has been applied, the results were dominated by the noise and no conclusions could be obtained. This method could be applied in the future, after accumulating a sufficient number of observations with the horns provided with the 90º hybridisers, however it cannot be used to correct the observations made before their installation.

3.6 Conclusions

In this chapter we presented the analyses of the MFI optics.

- The intensity beams of the MFI are symmetrical (ellipticities > 90) with FWHM of 0.9º at low frequencies (11 and 13 GHz) and 0.63º at high

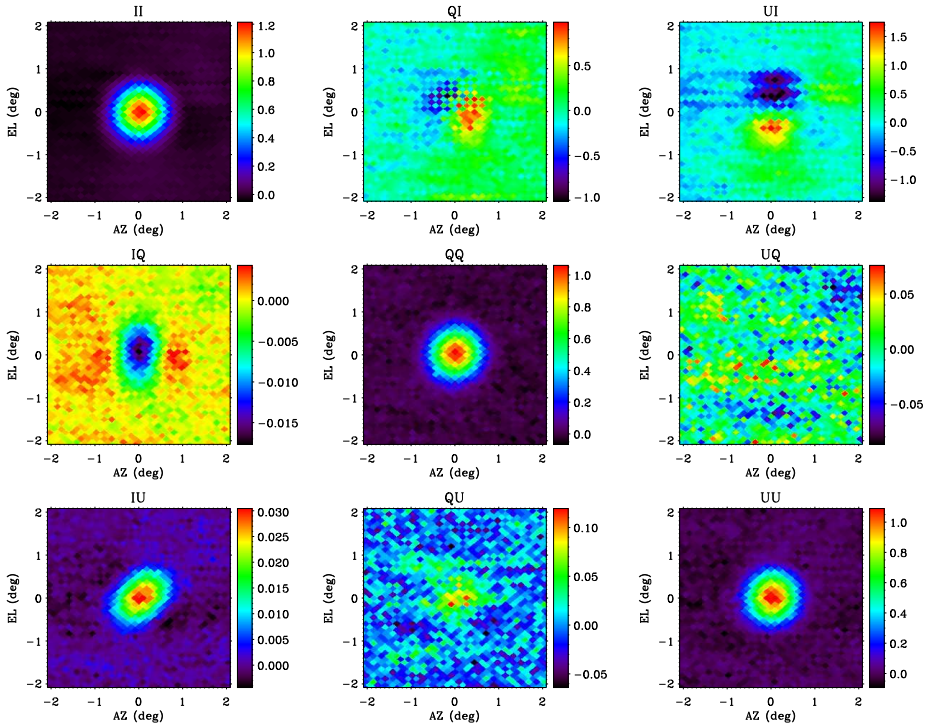

FIGURE 3.8— Müller matrix of horn 1. The data have been obtained with a selection of the best observations of the calibrators between June and October 2014, accumulating 27.2 hours of Tau A observations and 27.6 hours of Cas A observations. The main effect on cosmological observations is represented by the first column, the intensity-to-polarisation leakage, which introduce a spurious signal into the polarisation angular power spectrum. In the case of the MFI this leakage is about 0.8%.

frequencies (17 and 19 GHz).

- The sidelobes are found at levels of -70 dB at low frequency.
- The instrument is sensitive to a range of l up to 100 or 150. However, the minimum l at which it can observe will be ≈ 20 given the sky coverage, the masks that have to be applied and the map-making process.
- The leakage from intensity to polarisation, which is the main contaminant to CMB polarisation observations, is measured to be 0.8% in horn 1. The analysis could not be applied to other horns because of the insufficient amount of data with the other horn in the new configuration.

4

QUIJOTE-MFI Observations, Data Reduction and Maps of the Fields W44, W49, W63 and the Haze

In this chapter we present a description of the observations and data reduction of the Galactic fields W44, W49, W63 and the Haze, which were observed with the MFI instrument between 2013 and 2015. We show the final maps and discuss their quality and overall properties, including noise levels. The ancillary datasets used for the analyses presented in the following chapters are also described.

4.1 Fields Selection

One of the main drivers of the MFI is the characterisation of the CMB foregrounds (see section 2.1.1). For this analysis, we selected several fields along the Galactic plane, where the foreground emission is the main contributor, in order to perform a characterisation of the low-frequency foregrounds (synchrotron emission, free-free emission and AME) in several individual sources. The QUIJOTE fields Haze, W44, W49 and W63 were chosen in order to have a quasi-contiguous coverage of the Galactic plane between Galactic longitudes $l = 0^{\rm o}$ and $l = 86^{\rm o}$.

The Haze field is centred at Galactic coordinates $(l, b) = (8.73^{\rm o}, 2.23^{\rm o})$ and covers an area of approximately 700 squared degrees from the Galactic centre (visible only in horns 3 and 4 due to the elevation limit of the telescope, which is $30^{\rm o}$) to the geostationary satellite band which crosses the Galactic plane at

$l \approx 34^{\circ}$. The region is characterised by a hard synchrotron spectrum which was initially associated with Dark Matter (DM) annihilation processes (Finkbeiner, 2004b), thus it constituted a very appealing scientific case and we started the observations in 2013. However, at the moment of writing this thesis, this phenomenon is believed to be associated with an outflow from star-forming regions near the Galactic centre (Carretti et al., 2013) that would be responsible for both the Haze characteristic emission and for its counterpart in γ-rays, the so-called Fermi bubbles. More details about the region and its emission processes will be presented in section 5.6.1. Also, the Haze field presents one of the strongest polarised diffuse emission in the sky, thus it was a good candidate to test the capability of the MFI to detect large-scale structures.

Observations of the W44 field began in 2015, after the release of the C-BASS results at 5.6 GHz (Irfan et al., 2015), where the presence of AME was shown in the two HII complexes W43, W47 and in the SuperNova Remnant (SNR) W44. The observations of this field with the MFI were appealing because these sources were bright enough to put constraints on AME polarisation at a few percent level, apart from providing information on the uprising part of the AME spectrum, that was lacking in that paper. The results of this work have been published in Génova-Santos et al. (2017) and have been reproduced independently in the present work in Chapter 5.

The region around W63 has been observed mainly as another test for the MFI: W63 is a SNR very close to the Cygnus complex, an extended region dominated by free-free emission. We wanted to confirm our capability to disentangle the synchrotron emission associated with the SNR from the diffuse free-free mission, as well as to assess the capability to retrieve the polarised diffuse emission of extended regions both with the median-filter map making procedure and with the destriper algorithm (see section 2.5).

Finally, the W49 field was chosen because W51 is one of the strongest polarised sources in the area that we were interested in, and the centre of the field located in W49 allowed a contiguous coverage of the Galactic plane between the W44 and the W63 fields.

4.2 Observational Strategy

The QUIJOTE telescopes provide several observation modes. We showed in Section 2.3 that the best strategy for non-calibration observations is the transit mode since it is the less affected by atmospheric contamination. The criteria used to choose the optimal observation strategy were the following:

1. A contiguous coverage of the Galactic plane from $l \approx 0^{\circ}$ to $l \approx 85^{\circ}$. For this reason each field is contiguous to the next one, apart from the Haze

and the W44 fields, which are separated by the satellites band.

2. The minimum size for a QUIJOTE field is almost 20º, due to the angular distance between the horns in the focal plane[1], thus, if the angular separation of two sources of interest is less than 10º, we observe them in the same field, choosing an intermediate point as central coordinates and enlarging the area. For this reason, the sources W43 and and W47 are also covered in the observations of the W44 field. Similarly, the HII region W49 is covered by the observations of W51, although the name of the field is W49 because it lies almost at the centre of the field.

3. The velocity of the scan is fixed to 1º/s in sky coordinates for the transit mode. This has been chosen to avoid too strong accelerations and decelerations of the telescope when reaching the edges of the field, while it should be sufficiently fast to reduce the contamination of the 1/f noise. At low elevations we could use a higher speed, but we choose the same velocity for all the scans.

4. The duration of each observation is set in order to get a map with a size along the elevation direction similar to that along the azimuth direction, which is determined by the size of the scan. For a typical azimuth range of 25º, this corresponds to approximately 1.5 hours per observation.

5. Observations have to be performed before and after the culmination of the source in order to have at least two significantly different parallactic angles. This is fundamental to reconstruct the Stokes parameters Q and U independently, and benefits the destriper code thanks to a better determination of the baselines.

In the case of the W44 field, a different observation strategy was also attempted: before the modifications of the MFI during April 2014 (see subsection 2.2.3), neither horn 1 nor 4 performed adequately, the former because of the damaged polariser while the latter had amplifiers giving too high noise. Thus the observations were centred in the middle of the focal plane between horns 2 and 3 with a narrower azimuth range ($\approx 10^{\circ}$) and a shorter duration of 25 minutes. This allowed a much higher S/N per pixel, but did not provide information on the near sources W43 and W47. For this reason the area covered by the observations was later extended in order to include them.

[1]The distance between horns in the focal plane is 5º, but to observe the full source we have to add at least one FWHM (1º) and some additional width to avoid the edges of the map, which are very noisy.

The case of the Haze observations was different: we were not interested in a particular source but on the diffuse component. Moreover, the observation strategy for this region was chosen in June 2013, before having established the criteria described above and with few information about the location of the stronger features of this region. It was needed to include the Galactic centre, whose maximum elevation from the observatory is 35º, part of the Haze region and a "control region" where the synchrotron was expected to have a standard behaviour (spectral index ≈ -0.6 or less), while it was limited by the satellites band and the lower elevation limit of the telescope (30º). The final solution was to observe a huge field centred halfway between the Galactic centre and the satellites band, with an azimuth scan size of 33º and an observation time of 135 minutes, and observe this field every day at the same sidereal hour at elevation 33º, such that the shape of the field was parallel to the satellites band almost without any overlap. As a side note, this method was later implemented for all observations as an automatic queueing system since September 2013. However, we realised afterwards that this observation strategy had two major drawbacks, despite optimising all the criteria considered in 2013 at the beginning of the Haze observations campaign. The first one is that all observations were done before culmination in order to optimise the shape of the field, and this caused a poor performance of the destriper code, which was not taken into account because the code itself was not implemented yet. To correct for this effect, observations after culmination were started, but the total amount of observation time after culmination was still small compared to the time before culmination. Also, due to the low elevation (observations after culmination were done at 37º), the overlap between the two areas in the sky is smaller than in other regions. The second drawback was that the stronger polarised emission in the northern hemisphere was later found by Planck (Planck Collaboration et al., 2013) in a filament outside the region we chose to observe, thus the data have a smaller S/N than the extrapolation at the QUIJOTE frequencies that we made with the WMAP data.

Table 4.2 shows the main characteristics of the observation strategy for each field: the duration of each observation, the area and the central coordinates of each field and the main sources of interest.

4.3 Data Selection and Production of the Maps

We showed in section 2.4 the the pipeline of the MFI has evolved during its years of activity. In particular, when we produced the maps of the fields described above, the CTODs were not available, and an *ad hoc* procedure (which is represented in Fig. 4.1 and described below) was developed to discard bad data and

Field	Observational time (Hours)	Area (deg ^{2})	Galactic coordinates l, b (°)	Main sources
Haze	795	695	(8.73, 2.23)	M8, M16, M17, SgrA, W28, W31, W33, [LPH96]008.786-0.034
W44	210	250	(34.69, -0.42)	W43, W44, W47
W49	236	250	(43.20, 0.00)	W47, W49, W51
W63	250	250	(82.15, 5.32)	W63, CygA

TABLE 4.1— Main parameters of the QUIJOTE fields: the total observed time in each field, the area, the central coordinates and the main sources of the field.

consequently improve the quality of the maps. Also, since the destriper code was not optimised to reduce its computational time, after each step of the selection we produced some preliminary maps with the median-filter map-making (see section 2.5) with the HEALPix (Górski et al., 2005) pixelisation at the resolution of $N_{\rm SIDE} = 256$, which corresponds to a pixel size of 14 arcmin. Then, if the map did not present strange artefacts, we re-process the BTODs with the destriper code (see section 2.5) at the higher resolution of $N_{\rm SIDE} = 512$ (pixel size of 7 arcmin) in order to have intensity maps with a very reduced contamination from the 1/f noise. In the case of the polarisation data, the 1/f noise has a much lower knee frequency (see subsection 2.6.5 or Peláez-Santos 2013), thus the use of the destriper is not critical and, at the time of writing of this thesis, it introduces artificial strong gradients at the map level. This is not critical for the study of point or compact sources, but it could strongly affect the spectral indexes of the diffuse emission, especially in the Haze region.

Re-flagging of the Satellites

The source W43 in the W44 field was partially flagged out by the automatic flagging at the BTOD level since it was located in the proximity of the satellites band. For this reason the BTODs of this field were regenerated with a different flagging, masking out only pixels located within 3.5º from each individual satellite instead of 5º, which is the default option and the optimal one for nominal mode observations. A more refined approach would be to customise the radius for each satellite based on its strength: the radius for the saturating satellites could be kept to 5º, and the non-saturating satellites could be fitted with 2D-Gaussian to compute a suitable radius for the mask. However, this has not been implemented yet. The same procedure has been attempted for the Haze field, since it is the only other region analysed in this work that is partially masked by the satellites band, but some residual stripes remained, so we finally decided to keep the original flagging radius at 5º.

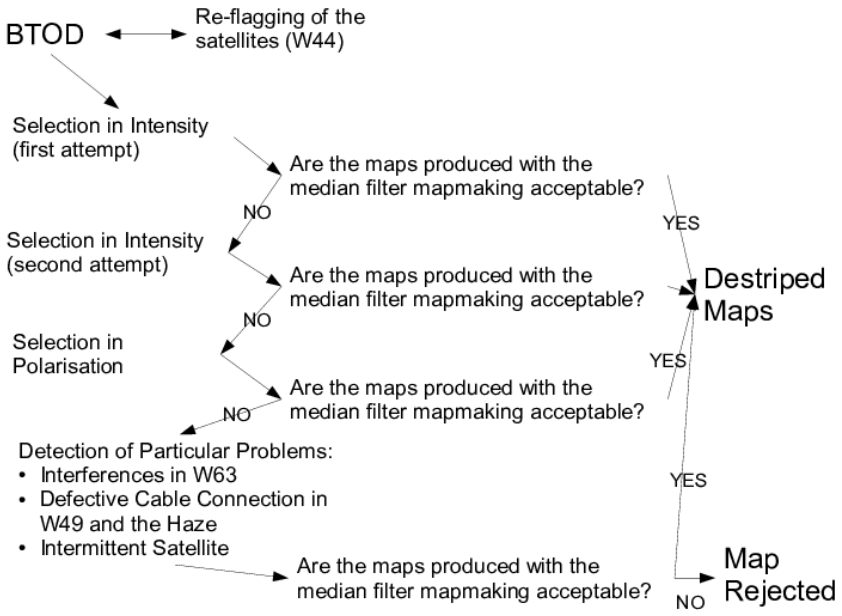

FIGURE 4.1— Scheme of the procedure used to select the data in this work.

Selection in Intensity

We use the simple map-making (see section 2.5) to produce maps of individual channels[2] for every observation at $N_{\rm SIDE} = 256$. This guarantees a sufficiently fast computation time, enough S/N ratio in each map and enough resolution given the beam of the instrument. Then, if a map contains visible undesirable features, e.g. a moving satellite or stripes resulting from 1/f noise, it is discarded.

After this selection, preliminary maps of the full dataset were produced with the median filter map-making method and, in many cases, some artefacts (mainly stripes or outliers) remain. In this cases, the process is repeated again with a more careful selection of individual observations that do not contain them.

Selection in Polarisation

While the median filter maps produced after the previous selection were usually sufficiently good in intensity, all the fields but W44 presented some very bright stripes in polarisation, which had no counterpart in intensity. For this reason, we produced daily maps of the differences of pairs of correlated channels, after a correction to take into account the different gains. While these maps do not represent the correct polarisation since they are insensitive to the polarisation angle, they can provide information on the polarised intensity[3]. However, in some cases the complete elimination of the stripes was impossible. This has been the case of a thick stripe in the 13 GHz map of horn 1 of W63, and of several thin stripes in the 19 GHz maps of W49 and of the Haze in horn 2 at 19 GHz.

Interference Correction (Case of W63)

The thick stripe of the 13 GHz map of W63 is very likely due to an interference pattern from the far sidelobes of the satellites band. In fact, it lies at 60º from the band, it is parallel to it, and the same pattern appears in the COSMO1 field which is just above in Galactic coordinates, thus it could represent the contamination from the first far sidelobe shown in Fig. 3.4. Since the S/N of these stripes was too low to make them visible in daily maps, we separated

[2] We remind that maps of individual channels are a combination of intensity and polarisation. Given that the former is usually much stronger than the latter, they can be used as an approximation of the intensity maps.

[3] Since during one individual observation the parallactic angle does not change much and the modulator is fixed, the map represents the quantity $Q\sin\theta + U\cos\theta$, with $\theta = 4\phi_{\rm mod} - 4\phi_0 + 2\gamma_{\rm par}$ =constant, see Eq. (2.17).

the observations in elevation bins of 5º and produced maps of each subset of observations in order to increase the S/N of the interference (which depends on the elevation and not on the Galactic coordinates) and to isolate the observations in which the interference does not superpose W63. This finally led to use only observations with elevations between 50º and 60º, which constituted approximately 50% of the total observation time.

Problems with Individual Channels (Case of W49 and the Haze)

The maps at 19 GHz of horn 2 of the W49 and the Haze fields present some thin stripes which are probably related to a problem with the (X-Y) channel, that has shown many instabilities in the baseline level during several months of observations probably due to a defective cable connection. To automatically detect this behaviour we tried two different approaches: the first one consisted in checking and discarding the observation in which the peak-to-peak baseline voltage was above 0.3 V (the voltage was dropping to half of its usual value in the daily inspection of the data), and the second one consisted in selecting the good observations based on the RMS of the baseline level. This second approach has been later automatically implemented in the pipeline at the CTOD level, but the analysis of the W49 field presented in this work was already concluded at that moment.

Intermittent Satellites (Case of the Haze)

The maps at 19 GHz of the Haze show an additional undesirable feature consisting in a thin line at constant declination. A close look at the BTOD showed that it is caused by an intermittent satellite which emits a strong signal during a few minutes every hour. This is not flagged since its signal is averaged out both in the daily maps and in the automatic RMS flagging procedure. An attempt to reduce its effect was done inspecting each file at the BTOD level and changing *ad hoc* the flag of the contaminated data, but some residual signal still affects the maps. Another procedure has been developed to find eventual satellites outside our catalogues based on azimuth stacks of each observation, and has been applied to all observations apart from the W44 region, since it would have flagged W43 due to its proximity to the satellites band.

4.4 Description of the Maps

The final maps have been produced with the selection of data described in the previous section at the finer resolution of $N_{\rm SIDE} = 512$ (pixel size of 7 arcmin) with the destriper code in intensity and with the median filter map-making in polarisation (see section 2.5). Some examples of the resulting maps are shown

Source	Type	l (°)	b (°)
W43	HII region	30.7	-0.02
W44	SNR	34.69	-0.42
W47	HII region	37.789	-0.187
W49	Star forming region	43.2	-00.00
W51	HII and SNR	49.14	-0.602
W63	SNR	82.15	5.31
M8	HII region	6.05	-1.08
M16	HII region (Eagle nebula)	17.05	0.77
M17	HII region (Omega nebula)	15.09	-0.65
W28	SNR	6.32	-0.24
W31	HII region	10.34	-0.24
W33	SNR and HII	12.81	-0.11
LPH96-008.786-0.034	HII region	08.47	-0.09

TABLE 4.2— List of the compact regions identified in the maps presented. The horizontal line separates the sources belonging to the Haze field.

in Figs. 4.2 to 4.5, in which we present also the comparison with the WMAP 9-years map at 23 GHz. Some of the compact sources are marked in each field and table 4.2 presents their location and the main type of emission, although a detailed description will be presented alongside the analysis in the next chapter.

In Fig. 4.2 we notice that the intensity map of the W63 field is dominated by the Cygnus complex, which emits mainly free-free emission, which is not polarised. However, the Q map at 13 GHz seems to present polarisation in the same location. This is due to leakage from intensity to polarisation at a level of $\approx 1\%$. The only compact source that clearly shows up in polarisation is the SNR W63, which is the main polarised source in the field and it is located a few degrees north of the Cygnus complex.

Fig. 4.3 shows the map of the W49 field. In intensity, four compact sources are detectable, but the ones located at $l < 40^{\circ}$ are W47 and W44, which were observed in the W44 field, thus they are excluded on the analysis of this region. The others are W49 and W51, two of the largest molecular clouds in the Galaxy, which also host some SNR. However, W51 is the only one visible in polarisation, and it is located outside the maps from horn 3 (first line). For this reason, we used the maps from horn 1 to retrieve the flux, although its quality is a bit worse.

Fig. 4.4 shows the map of the W44 field. It contains 3 main sources: W43, W44 and W47. Only W44, which is a SNR, presents polarisation, although the WMAP data show evidence of a diffuse component alongside the Galactic plane. The satellites band crosses the map next to W43, but it is not visible in the maps at 17 GHz.

Finally, Fig. 4.5 presents the maps of the Haze field. We identified 7 compact sources in intensity and the Galactic centre is visible at the right edge of the maps of horn 3, however it is not visible in the other horns. In polarisation we recover most of the diffuse signal, and a structure is seen in the MFI maps at $l \approx 8^{\circ}$ which is not visible in the WMAP 23 GHz data. Also, we note a quadrupolar pattern visible in Q and U (rotated by 45° in the latter map) at the location of M17. This is another example of leakage at the level of 1%. The quadrupolar pattern, which was predicted in section 3.5, is caused by a point source with respect to the beam of the instrument: the leakage from the Cygnus complex caused a diffuse signal because it is an extended source.

4.5 Map Quality Assessment

In order to have a quantitative estimate of the quality of the maps, we have computed the pixel-to-pixel standard deviation of the data in circles of radius 1°, for each horn and frequency. For each map, the position of the circle was chosen in order to avoid bright sources and strong foregrounds, while having a similar number of data samples per pixel to that in the centre of the map[4]. The results are shown in tables 4.3-4.6. The values are in units of μK per beam with a FWHM of 1° (μK/1° beam). It is important to note that the noise levels in intensity in all fields are much higher (from 3 to 10 times) than in polarisation. This is due to two reasons: the first is that the sky emission is much stronger in intensity than in polarisation and the second one is the effect of the 1/f noise, which is strongly reduced with the subtraction of correlated channels in the polarisation maps. However, the RMS of the intensity in the W49 region is much higher than in other fields, while the polarisation noise is comparable. We are not sure of the reason, but we suspect that this can be due to a poor choice of the location of the circle used for the estimation, which probably presents a stronger intensity emission that is not sufficiently appreciable in the maps. In fact, the circle used for the W49 field is nearer to the Galactic plane than the circles used for other regions, since the extension of the field in Galactic latitude is smaller.

In order to avoid the bias introduced by sky emission in the RMS estimates, we applied Jack-Knife (JK) tests on our maps. The common way to apply this technique is to resample the data into two halves and to produce the maps for each half. Since the observed sky is the same in each map, the difference

[4]Observations done before and after culmination produce a different sky coverage, since the shape of the field is different due to Earth rotation. Only pixels observed in both cases are used for the discs, which can be recognised by having approximately the same number of data samples as the ones in the centre of the map.

between them should be a map of pure noise. We split the observations based on the azimuth of the source (if less or greater than 180°) and forced each half to have the same number of observations from each group. Then, we ordered the observations by increasing elevation and we put alternatively one in one half and one in the other half in order to have the same atmospheric contribution and a sky coverage as similar as possible in the two halves. The sixth column of tables 4.3-4.6 shows the pixel-to-pixel standard deviation of the JK Q map in the same circles as above, divided by 2. This factor is due to the fact that each half of the JK map has half the integration time, which gives a noise $\sqrt{2}$ stronger, and that the JK map is the subtraction of two maps, which increases the noise by another factor $\sqrt{2}$. The JK U maps present similar values and are not reported in the tables. Generally, the noise levels derived from the JK maps are lower than the noise level of the sky maps, since the latter include astronomical signal that is removed in the subtraction of the JK maps. However, since we did the analysis in clear regions, the sky contribution is minimal, and the RMS in the polarisation maps and in the JK are very similar. The notable exception is the W63 region, which presents above-average values for the polarisation RMS in the lower frequencies that are not reflected in the JK. Probably this is due to residuals of the interference pattern at 11 GHz described in section data selection. The same feature is visible in the Haze region, horn 3 at 11 GHz, as shown in table 4.6.

In the last column of tables 4.3-4.6 we show the instrument sensitivities of each horn and frequency, calculated from column 6 by scaling with the square root of the average integration time of each pixel. These can be compared with the nominal sensitivities presented in table 2.1. The values of the sensitivities calculated from the maps are generally higher than expected, but reasonable, typically with values between 1 and 3 mK $s^{1/2}$. This is probably due to 1/f residuals in polarisation. We note some particular cases in which they are much worse, such as the measured sensitivity of horn 1 in the W49 field, or the 19 GHz channels of horn 2 in the W63 field, generally due to the residual artefacts in the maps. In the case of W44, the higher values of horn 1 can be caused by some leakage, since the polarisation levels are not similar between horn 1 and 3. Finally, in the Haze region, the worst sensitivity corresponds to the 19 GHz channels of horn 4, since most observations were done before the replacement of the amplifier (see subsection 2.2.3). The removal of all observations affected by that problem reduced considerably the amount of data available and, as a result, the S/N of the remaining data was insufficient to reach any meaningful conclusion, thus we opted to exclude this map from the scientific analyses of the region.

Horn	Freq(GHz)	I(μK)	Q(μK)	U(μK)	JK,Q(μK)	Sensitivity,Q(μK s$^{1/2}$)
1	11	2754	83	46	75	5127
1	13	2206	64	46	47	3235
2	17	2195	27	24	30	1836
2	19	1760	43	37	47	2886
3	11	2998	51	36	39	1834
3	13	2334	41	40	37	1755
4	17	2027	27	32	29	1404
4	19	1675	39	40	35	1673

TABLE 4.3— Pixel-to-pixel standard deviations of 1°-radius discs in a clean area in the W49 region for each horn and for each frequency in intensity and polarisation (columns 3-5). Pixel-to-pixel standard deviations in the same disc for the Jack-Knife (JK) polarisation (Q) maps (column 6). Polarisation sensitivity calculated from the JK polarisation map (column 7). See text for details.

Horn	Freq(GHz)	I(μK)	Q(μK)	U(μK)	JK,Q(μK)	Sensitivity,Q(μK s$^{1/2}$)
1	11	670	97	125	34	1805
1	13	523	74	94	32	1688
2	17	370	43	54	32	1437
2	19	335	112	87	108	4541
3	11	727	113	148	49	2006
3	13	528	85	115	48	2260
4	17	352	40	46	39	1374
4	19	323	65	60	57	2004

TABLE 4.4— Same as for table 4.3, but for W63.

Horn	Freq(GHz)	I(μK)	Q(μK)	U(μK)	JK,Q(μK)	Sensitivity,Q(μK s$^{-1/2}$)
1	11	415	119	82	117	3314
1	13	372	102	70	108	3043
2	17	390	29	37	28	1095
2	19	355	55	68	46	2132
3	11	614	53	46	63	1598
3	13	369	46	46	62	1619
4	17	428	43	38	43	1110
4	19	362	50	52	55	1327

TABLE 4.5— Same as for table 4.3, but for W44. See also table 1 of Génova-Santos et al. (2017).

Horn	Freq(GHz)	I(μK)	Q(μK)	U(μK)	JK,Q(μK)	Sensitivity,Q(μK s$^{-1/2}$)
1	11	503	35	41	31	2121
1	13	266	30	31	28	1418
2	17	232	57	69	48	2071
2	19	322	66	84	65	2630
3	11	515	73	60	36	2383
3	13	429	50	48	32	2101
4	17	338	30	32	30	2032
4	19	378	59	45	57	3816

TABLE 4.6— Same as for table 4.3, but for the Haze region.

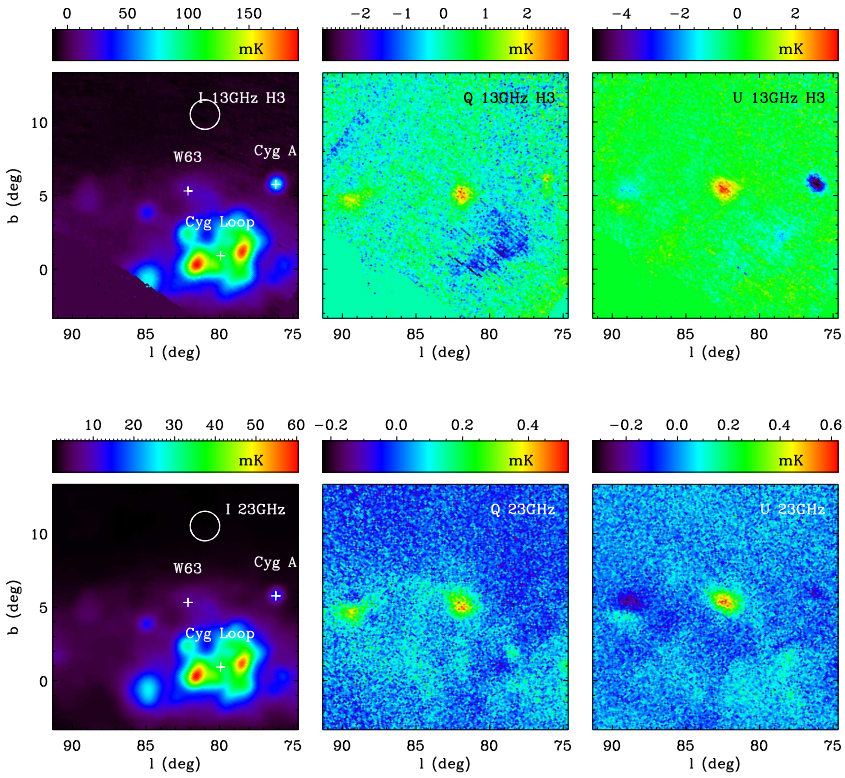

FIGURE 4.2— Maps of the W63 field, in intensity (first column) and polarisation (Q in the second one and U in the third one). The sources analysed in the next chapters are indicated with "+". We also indicated the positions of the Cygnus complex and Cyg A. The circle marks the clean region used to calculate the RMS of the map. Each line corresponds to a different frequency, as indicated in the figure, the last line shows the comparison with WMAP 9-years, 23 GHz.

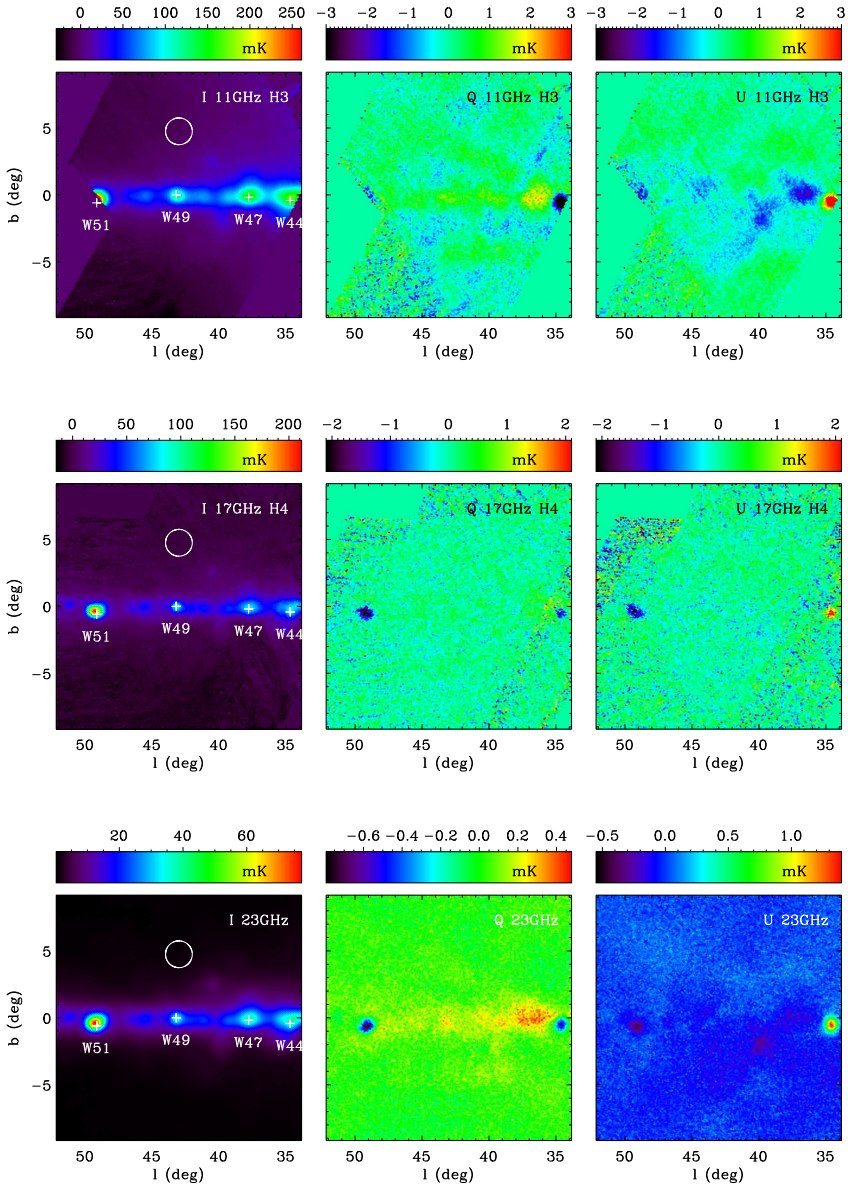

FIGURE 4.3— Same as in Fig. 4.2, but for the W49 field.

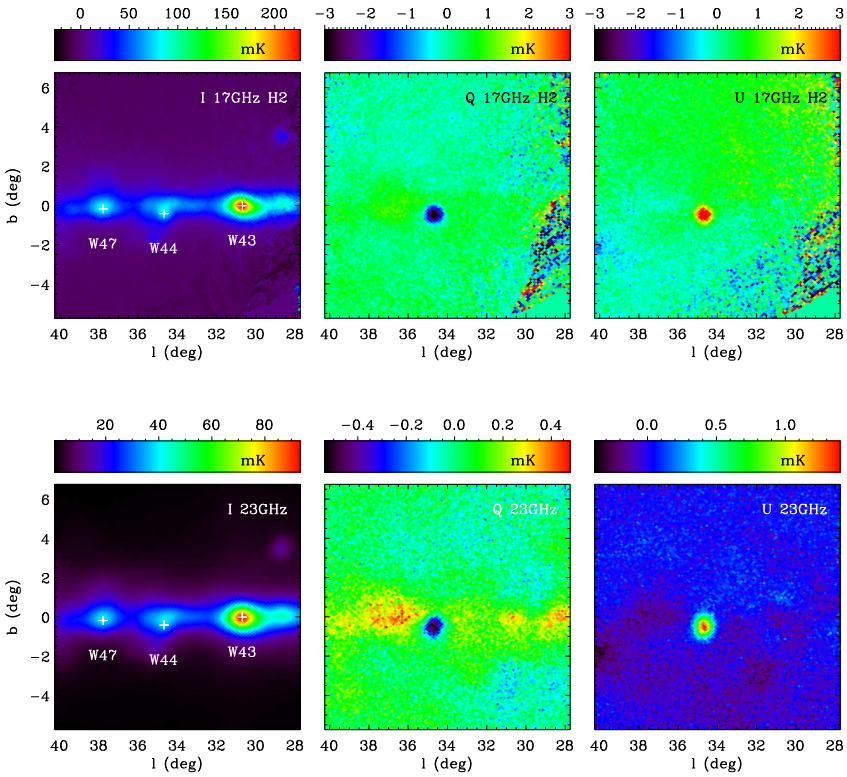

FIGURE 4.4— Same as in Fig. 4.2, but for the W44 field.

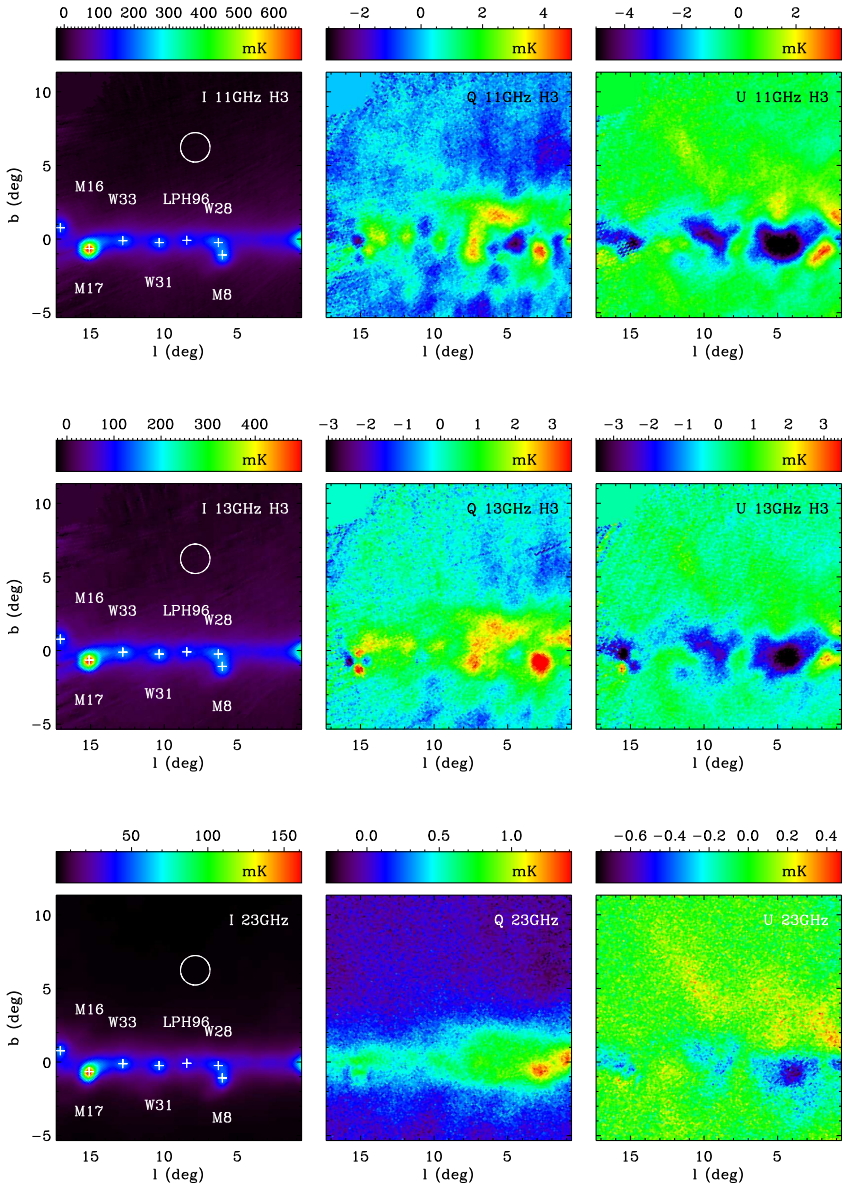

FIGURE 4.5— Same as in Fig. 4.2, but for the Haze region.

5

Analyses of the Galactic Plane Fields

This chapter presents the analyses of the regions in the Galactic fields observed with QUIJOTE that were discussed in the previous chapter. These are complemented at different frequencies with ancillary data which are briefly described. Then, the methodology of the analyses is presented. Later, for each region, the main point sources are presented and their Spectral Energy Distributions (SEDs) are calculated and discussed. Finally, a section is dedicated to the analysis of the diffuse emission in the Haze field through a correlation technique.

5.1 Ancillary Maps

The production of the SEDs requires data at a much larger range of frequencies than the ones that QUIJOTE can provide. This information is obtained from the following experiments:

- At 408 MHz we use the radio continuum all-sky map presented in Haslam et al. (1981, 1982) that combines data from four different surveys at a final resolution of 0.85º. New versions of the map have been published in Platania et al. (2003), which is the one used in this thesis, and in Remazeilles et al. (2015).

- At 0.82 GHz we use the survey made with the 25 m Dwingeloo telescope in the Netherlands between 1965 and 1967. It covers the range in declinations from -7º to +85º. The effective resolution of the map is 1.2º. The details of the survey can be found in Berkhuijsen (1972).

- At 1.42 GHz (21 cm), we use the survey described in Reich (1982). It was performed using the 25 m Stockert telescope in Germany at a resolution of 35' (0.58°) and covered declinations > 20°. A correction factor of 1.55 was applied to the flux of point sources to account for the main beam-to-full beam calibration, as explained in Reich & Reich (1988).

- At 2.326 GHz, we use the survey made with the 26 m telescope of the Hartebeesthoek Radio Astronomy Observatory (HartRAO), located in South Africa, which is described in Jonas et al. (1998) and covers 67% of the sky. We use a correction factor for the main beam-to-full beam calibration of 1.45, which is taken from Jonas et al. (1998).

- At 4.8 GHz (6 cm) we used a map produced with the 25 m Urumqi telescope of the National Astronomical Observatories of the Chinese Academy of Sciences in collaboration with the *Max-Planck-Institut für Radioastronomie* (Han et al., 2013; Sun et al., 2007). It covers a limited region of the Galactic plane ($10^o < l < 230^o$, $|b| < 5^o$) with an angular resolution of 9.5', both in intensity and in polarisation.

- The Wilkinson Microwave Anisotropy Probe (WMAP, Page 2000) provided full-sky maps at five different frequencies, from 23 GHz to 94 GHz. In this work we used the 9-year release 1-deg-smoothed maps (Bennett et al., 2013) that are publicly available in the LAMBDA website[1] in the HEALPix format at $N_{\rm side} = 512$.

- The Planck satellite provided full-sky maps with two instruments: the Low Frequency Instrument (LFI, Bersanelli et al. 2010), which observed at 30, 44 and 70 GHz, and the High Frequency Instrument (HFI, Lamarre et al. 2010), which observed from 100 to 857 GHz in 6 different bands. The maps are publicly available at the Planck Legacy Archive website[2] in the HEALPix format at $N_{\rm SIDE}$=2048 for the HFI and $N_{\rm SIDE}$=1024 for the LFI.

- We used the three full-sky maps from the Diffuse Infrared Background Experiment (DIRBE, Schlegel et al. 1998b) at frequencies between 1 and 3 THz.

Table 5.1 presents a summary of the ancillary maps used, providing information about the frequencies, the resolution, the sky coverage, the availability of polarisation data and a reference.

[1] *https://lambda.gsfc.nasa.gov/*
[2] *http://pla.esac.esa.int/pla/*

Name	Freq. (GHz)	Res. (°)	Full sky	Polarisation	Reference paper
Haslam	0.408	0.85	Yes	No	Haslam et al. (1981)
Dwingeloo	0.82	1.2	No	No	Berkhuijsen (1972)
Reich	1.420	0.58	No	No	Reich (1982)
HartRAO	2.36	0.33	No	No	Jonas et al. (1998)
Urumqi	4.8	0.16	No	Yes	Sun et al. (2007)
WMAP K-band	23	0.88	Yes	Yes	Page (2000)
WMAP Ka-band	33	0.66	Yes	Yes	Page (2000)
WMAP Q-band	41	0.51	Yes	Yes	Page (2000)
WMAP V-band	61	0.35	Yes	Yes	Page (2000)
WMAP W-band	94	0.22	Yes	Yes	Page (2000)
Planck LFI	30	0.55	Yes	Yes	Bersanelli et al. (2010)
Planck LFI	44	0.40	Yes	Yes	Bersanelli et al. (2010)
Planck LFI	70	0.23	Yes	Yes	Bersanelli et al. (2010)
Planck HFI	100	0.16	Yes	Yes	Lamarre et al. (2010)
Planck HFI	143	0.12	Yes	Yes	Lamarre et al. (2010)
Planck HFI	217	0.08	Yes	Yes	Lamarre et al. (2010)
Planck HFI	353	0.08	Yes	Yes	Lamarre et al. (2010)
Planck HFI	545	0.08	Yes	No	Lamarre et al. (2010)
Planck HFI	857	0.08	Yes	No	Lamarre et al. (2010)
DIRBE	1250	0.64	Yes	No	Schlegel et al. (1998b)
DIRBE	2142	0.63	Yes	No	Schlegel et al. (1998b)
DIRBE	3000	0.62	Yes	No	Schlegel et al. (1998b)

TABLE 5.1— Summary of the ancillary data in this thesis.

5.2 Methodology

This section explains the procedure used to derive the SEDs of the compact sources from the maps described in the previous chapter. This process involves four steps:

1. All the maps are degraded to a common angular resolution and set to common measurement units.

2. The flux density of each compact source is calculated at each frequency through the aperture photometry technique, in which the signal is integrated in an area around the source and the background[3] is subtracted.

3. The polarised intensity is a non-negative quantity by definition, thus it does not follow a Gaussian distribution. This causes a bias that needs to be corrected.

4. The derived SEDs are fitted with a motivated model to assess the physical properties of the analysed sources.

5.2.1 Smoothing

In order to compare maps from different experiments, we have to degrade all the maps to a common angular resolution, which we choose to be[4] FWHM=1°. For this reason, we convolute all the maps with symmetric two-dimensional Gaussian functions with FWHMs given by:

$$\mathrm{FWHM_{sm}} = \sqrt{(1^2 - \mathrm{FWHM_{map}})} \tag{5.1}$$

where $\mathrm{FWHM_{map}}$ is the original angular resolution of the map in degrees. The convolution can be performed in the real space or in the Fourier space. The maps from lower frequencies, from Planck and from DIRBE have been smoothed in Fourier space since this method is much faster than the convolution in the real space. However, we saw in the QUIJOTE maps that spurious signal was introduced by bright pixels at the edges of the maps. For this reason, first we

[3]Through this chapter, we use the generic word "background" to account for all emission mechanisms along the line of sight that are not caused by the compact source itself. We do not reference to the relative position of the source of interest with respect to the position of the other emissions in the line of sight.

[4]The final resolution should be the lowest of all maps, that is 1.2 degrees for the Dwingeloo map. Instead we choose 1 degree since it is significantly larger than the other resolutions and some surveys provide the data already smoothed to the 1 degree angular resolution. We left the Dwingeloo map at its original resolution.

masked all pixels with an integration time lower than 2 s and then we did the convolution in the real space.

The smoothed maps from WMAP were directly downloaded from the Lambda[5] webpage. In this case the exact window function of the experiment instead of the Gaussian approximation was used.

5.2.2 Aperture Photometry

One standard way to calculate flux densities of a source in a map in the microwave regime is aperture photometry. It consists in integrating the flux of a region with a given angular size centred in the source of interest and subtracting a background level over a control region to remove the contamination from other emissions along the line of sight:

$$S_\nu = a(\nu)\left[\frac{\sum_{i=1}^{n_1} T_i}{n_1} - \tilde{T}\right] \tag{5.2}$$

where S_ν is the flux density we want to determine, $a(\nu)$ is the conversion factor from temperature to flux given in the equation below, the sum is performed over the n_1 pixels in the region of interest, and $\tilde{T}$ is the median of the temperature of the n_2 pixels in the background region, since the median is a better estimator than the average in case of strong variations. The conversion factor is given by:

$$a(\nu) = \frac{h^2\nu^4}{2k_\mathrm{b}T_\mathrm{cmb}^2c^2}\,\sinh^{-2}\left(\frac{h\nu}{2k_\mathrm{b}T_\mathrm{cmb}}\right) n_1\Omega_\mathrm{pix} \tag{5.3}$$

where h and k_b are the Planck and Boltzmann constants, c the speed of light, $T_\mathrm{cmb} = 2.725\,\mathrm{K}$ the CMB temperature (Fixsen et al., 1996) and Ω_pix the solid angle subtended by each pixel.

In the case of perfect white uncorrelated noise, the error associated with S_ν can be easily estimated through:

$$\sigma(S_\nu) = a(\nu)\left[\frac{\sum_{i=1}^{n_1}\sigma_i^2}{n_1^2} + \frac{\pi}{2}\frac{\sum_{j=1}^{n_2}\sigma_j^2}{n_2^2}\right]^{1/2} \tag{5.4}$$

where σ_i represents the error of each pixel. The factor $\pi/2$ comes from the fact that the error on the estimate of the median of a normal distribution of n points is $\sqrt{\pi/2}\sigma/\sqrt{n}$ for n sufficiently large (this result has been confirmed through simulation by R. Génova (IAC) inside the QUIJOTE collaboration).

The noise σ_i is calculated as the pixel-to-pixel standard deviation of all pixels in the background region (the standard deviation of the pixels in the

[5] *https://lambda.gsfc.nasa.gov*

aperture would be larger due to the presence of the source itself and will not be a good estimate of the noise), which is a good approximation in case of independent pixels. However, in QUIJOTE the instrumental noise between pixels is correlated due to the presence of $1/f$ residuals, and also the Galactic background fluctuations introduce an important contribution to the error at all frequencies, which is correlated on the order of the beam size. One method to take this into account, although we do not use it in this work, is to introduce the number of independent pixels in each region, n'_1 and n'_2, but their estimation is not trivial. A conservative approach would use the number of beams in the aperture, $n'_{1,2} = n_{1,2}\Omega_{\rm pix}/\Omega_{\rm beam}$, which assumes that the noise of pixels inside the same beams is completely correlated. This method has been attempted but the resulting errors were too large. For this reason, we finally choose to use the number of pixel n_1, n_2 as they were completely independent. The resulting error will be slightly underestimated, but they will be more similar to the real errors than with the conservative approach. However, we added a 5% statistical error to the QUIJOTE data to account for eventual calibration errors, as described in section 2.6.

The usual choices for the regions are a circle centred on the source (table 4.2 shows the list of sources analysed and their positions) with a radius 1º and a concentric annulus between radii 1.33º and 1.66º for the background, in order to get rid of eventual large-scale fluctuations and to have approximately the same area covered by the circle and by the annulus. This procedure has been applied separately for the three Stokes parameters, I, Q and U.

5.2.3 De-biasing of the Polarised Intensity

In cases of low signal-to-noise fluxes, or when placing upper limits on the polarised flux P, as it will be our case, it is necessary to de-bias the flux densities derived from the aperture photometry integration. This requirement comes from the fact that the posterior distribution of the polarised intensity P does not follow a Gaussian distribution. In fact P is a quantity that is positive by definition, and this introduces a bias into any estimate: for any true P_0 we would expect to measure on average a polarisation $P_{\rm obs} > P_0$. This can be easily understood if we write explicitly the Stokes parameters and their noises, $Q_{\rm obs} = Q_0 + N_Q$ and $U_{\rm obs} = U_0 + N_U$. The observed polarised intensity $P_{\rm obs}$ is

given by:

$$P_{\rm obs} = \sqrt{Q_{\rm obs}^2 + U_{\rm obs}^2} = \sqrt{(Q_0 + N_Q)^2 + (U_0 + N_U)^2} = \\ = \sqrt{(Q_0^2 + U_0^2) + (2Q_0N_Q + 2U_0N_U) + (N_Q^2 + N_U^2)} = \\ = \sqrt{(P_0^2) + (2Q_0N_Q + 2U_0N_U) + (N_Q^2 + N_U^2)} > P_0 \quad (5.5)$$

since the variable $(2Q_0N_Q + 2U_0N_U)$ is zero on average but $(N_Q^2 + N_U^2)$ is always positive. In order to get the debiased fluxes, $P_{\rm db}$, from the measured ones, P, we use the approach described in Plaszczynski et al. (2014). They proposed two estimators of the debiased polarised intensity, which, in the case of S/N ≥ 1, are given by:

$$P_{\rm db} = \sqrt{P^2 - b_2} \qquad \text{Asymptotic Estimator (AE)} \quad (5.6)$$

$$P_{\rm db} = P - \frac{b_2}{2P}\left(1 - \exp\frac{-P^2}{b_2}\right) \qquad \text{Modified Asymptotic Estimator (MAE)}, \quad (5.7)$$

where

$$b_2 = \frac{Q^2\sigma_U^2 + U^2\sigma_Q^2}{P^2} \quad (5.8)$$

in the case that Q and U are obtained independently and the covariance matrix between them can be neglected. The authors showed that the MAE is more reliable than the AE at lower S/N, thus it was the final choice we used in this work. Since the debiasing is a small correction, we do not take into account its error, thus the error in the final polarised intensity is just:

$$\sigma_{P_{\rm db}} = \sigma_P = \sqrt{\frac{Q^2\sigma_Q^2 + U^2\sigma_U^2}{P^2}} \quad (5.9)$$

5.2.4 Model of the SEDs in Intensity

The main emission mechanisms in intensity in our frequency range are:

1. Synchrotron emission
2. Free-free emission
3. Anomalous Microwave Emission (AME)
4. Thermal dust

5. Cosmic Microwave Background (CMB)

A brief description of the physics of these processes is presented in the introduction (see subsection 1.4.3). We use physical models for the classical processes (see Rohlfs & Wilson 1996 for an exhaustive description), and a phenomenological for the AME. Detailed information on the physics of the AME can be found for example in Ali-Haïmoud et al. (2009). Here we summarise the equations used for each model, and the free parameters used for the fit.

The flux density from synchrotron emission is modelled with a power law, parametrised by its amplitude at 1 GHz ($A^{\rm sync}_{1GHz}$) and its exponent $\beta^{\rm sync}$:

$$S_{\rm sync} = A^{\rm sync}_{1GHz}\nu^{\beta^{\rm sync}} \tag{5.10}$$

The exponent is directly related to the spectral energy distribution of the electrons, which is a power law according to radio and γ rays observations, with $\beta^{\rm sync} = 0.5(\delta + 1)$ where δ is the exponent of the energy distribution, $N(E) \propto E^{\delta}$.

The free-free emission is modelled with equation (10.33) of Rohlfs & Wilson (1996), where the numerical coefficients and the Gaunt factor have been changed according to Draine (2011). We report here the equations for the reader's convenience:

$$g_{\rm ff} = \ln\left\{\exp\left[5.960 - \frac{\sqrt{3}}{\pi}\ln(\nu\left(\frac{T_e}{10^4}\right)^{3/2}\right] + e\right\} \tag{5.11}$$

$$\tau_{\rm ff} = 5.468\cdot 10^{-2}\cdot T_e^{-1.5}\cdot\nu^{-2}\cdot {\rm EM}\cdot g_{\rm ff} \tag{5.12}$$

$$S_{\rm ff} = T_e\,(1-e^{-\tau_{ff}})\,2k_B\left(\frac{\nu\cdot 10^9}{c}\right)^2\cdot 10^{26} \tag{5.13}$$

where e is the Euler's number, the frequency is in GHz and we have introduced the Gaunt factor g_{ff}, the optical depth $\tau_{\rm ff}$, the electrons temperature T_e in Kelvin, which we keep fixed during the fit and is usually taken as the typical value of 8000 K, the emission measure[6] EM, which is the only free parameter of the fit[7]. The last equation can be identified as the radiative transfer equation, and includes the conversion factor from temperature to flux density units. The

[6]The emission measure is the integral of the square of the electrons density along the line of sight. According to Rohlfs & Wilson (1996), the typical value for the EM of an HII region is of the order of 10^6 pc $\cdot$ cm^{-6}, but in this work the EM is diluted over the full disk of the aperture photometry and takes values of the order of 10^3 pc $\cdot$ cm^{-6}.

[7]The use of only one parameter in the fit for the free-free model is a standard procedure, however the model should depend also on the electrons temperature T_e and on the solid angle subtended by the source with respect to solid angle subtended by the aperture.

choice of a single free parameter is due to the fact that the fit of a SED is quite degenerate between synchrotron and free-free, since the latter behaves like a black body spectrum for $\tau_{\rm ff} \gg 1$ and a power law with spectral index $\approx$ -0.15 for $\tau_{\rm ff} \ll 1$, and in our frequency regime usually this latter case holds. In fact, the turn-over frequency ν_0 between optically thick and optically thin regimes is given by (Rohlfs & Wilson, 1996):

$$\nu_0 = 0.3045(T_e)^{-0.643}{\rm EM}^{0.476} \tag{5.14}$$

which is around 1 GHz for values of EM$\sim 10^6$ pc·cm^{-6}.

The AME is adjusted with an empirical model, described in Bonaldi et al. (2007), which consists of a parabola in the the logarithmic space. This model depends on 3 free parameters: the maximum amplitude $A_{\rm max}^{\rm AME}$, the peak frequency $\nu_{\rm peak}^{\rm AME}$ and the slope at 60 GHz, m_{60}. The equation can be written in this form:

$$S_{\rm AME} = A_{\rm max}^{\rm AME} \exp\left[-\left(\frac{m_{60}\ln\nu_{\rm peak}^{\rm AME}}{\ln(\nu_{\rm peak}^{\rm AME}/60)}+2\right)\ln\nu + \frac{m_{60}}{2\ln(\nu_{\rm peak}^{\rm AME}/60)}(\ln\nu)^2\right] \tag{5.15}$$

We constrain the m_{60} parameter to values between 2 and 6, since values outside this range lead to spectra quite different from the standard spinning dust physical models.

The thermal dust emission is modelled as a grey body. Its equation is the one of a black body multiplied by a factor $(\nu/\nu_{\rm peak})^{\beta^{\rm dust}}$ that accounts for opacity effects, thus it depends on 3 parameters: the dust temperature $T_{\rm dust}$, the dust emissivity index $\beta^{\rm dust}$ and the optical depth at 250 μm, τ_{250}:

$$S_{\rm dust} = \tau_{250}\left(\frac{\nu}{\nu_{\rm peak}}\right)^{\beta^{\rm dust}} \frac{2h\nu^3}{c^2}\frac{1}{\exp\left(\frac{h\nu}{k_B T^{\rm dust}}\right)-1} \tag{5.16}$$

where h and k_B are the Planck and Boltzmann constants and c is the speed of light. The factor $\nu_{\rm peak}$ corresponds to the turn-over frequency and generally gives the peak of the spectrum. Its typical value is $\approx$ 1200 GHz.

The CMB emission is not modelled since its main contribution is a monopole which is eliminated with the background subtraction. Fluctuations of the CMB are not eliminated but they are negligible in comparison with the typical flux densities of the compact sources that we analysed.

Usually, we do not fit the SED with all parameters at the same time, since the simultaneous fit of the synchrotron and the free-free can lead to degeneracies in the parameters (both models follow a power law). For this reason we fit the

synchrotron only for sources that include a supernova remnant (SNR) in the aperture photometry disk, and we fit with only the free-free otherwise. Thus, the final model is:

$$S_{\rm TOTAL} = S_{\rm sync}(\beta^{\rm sync}, A^{\rm sync}_{1GHz}) + S_{\rm ff}({\rm EM}) + \\ + S_{\rm AME}(A^{\rm AME}_{\rm max}, m_{60}, \nu^{\rm AME}_{\rm peak}) + S_{\rm dust}(\tau_{250}, T^{\rm dust}, \beta^{\rm dust}) \quad (5.17)$$

which depends either on 7 in case of fitting for free-free emission or 8 parameters in case of fitting for synchrotron emission.

5.2.5 SEDs in Polarisation

The analyses of the SEDs in polarisation have been restricted only to the known polarised sources in each region, which are W44, W51 and W63, and to the frequency range 10-100 GHz (the reason for the frequency range will be explained below). The main physical mechanisms that affect the polarisation at these frequencies are the synchrotron emission and the Faraday rotation.

The synchrotron emission is in fact almost fully polarised, in case of a perfectly aligned magnetic field at the source (see subsection 1.4.3). This is far from true in reality, so the polarisation fraction does not usually reach 10%. Since the synchrotron is modelled with a power-law in intensity, and since the polarisation fraction is not expected to depend on the frequency, we can also model the polarised synchrotron emission with a power law with parameters $A^{\rm sync}_{\rm pol}$ and $\beta^{\rm sync}_{\rm pol}$. Theoretically, the spectral index in polarisation should be the same as in intensity, but, in practice, the spectral index in intensity is usually found to be flatter because the flux is contaminated by free-free emission as frequencies larger than 1 GHz. On the contrary, in polarisation the synchrotron is much less contaminated by other emission mechanisms. In fact, the free-free emission is unpolarised and the thermal dust, although polarised, is not an important component at frequencies below 100 GHz (we also exclude points above 80 GHz to avoid any possible contamination). Some AME models predict a polarisation fraction of a few percent but only upper limits have been put at the moment of the writing of this thesis. For these reasons, the spectral index in polarisation is the best estimator of the synchrotron index. In this work, we obtain $\beta^{\rm sync}_{\rm pol}$ from a linear fit in logarithmic space to the polarisation data. Points below 10 GHz are excluded from the fit since they are potentially depolarised due to Faraday rotation.

The Faraday rotation is a mechanism that affects polarised light travelling through a medium with charged particles and magnetic fields. The polarisation

plane is in fact rotated by:

$$\Delta\gamma = \frac{e^3}{2\pi c^2 m_e^2}\frac{1}{\nu^2}\int_{\mathrm{LoS}} B_{||}(z)N_e(z)dz \tag{5.18}$$

where $B_{||}$ is the component of the magnetic field parallel to the line of sight (LoS), N_e is the electron number density and m_e, e, c are the electron mass, the electron charge and speed of light, respectively. Usually, we define the Rotation Measure (RM) as:

$$\mathrm{RM} \equiv \frac{e^3}{2\pi c^4 m^2}\int_{\mathrm{LoS}} B_{||}(z)N_e(z)dz \tag{5.19}$$

and the rotation angle can be written as $\Delta\gamma = \mathrm{RM}\lambda^2$ where λ is the wavelength at which we are observing. Hence, the RM can be obtained through linear regression of the polarisation angles versus the square of the wavelength:

$$\gamma(\lambda) = RM \cdot \lambda^2 + \gamma_0 \tag{5.20}$$

γ_0 is a reference angle that corresponds to the polarisation of the light in the limit $\lambda = 0$. The effect of Faraday rotation is stronger at low frequencies, but the effect is so strong below 10 GHz that the rotation can undergo several turns, so every small inhomogeneity is amplified and the resulting polarisation is almost randomised.

5.3 W44 Field

The W44 QUIJOTE observations include a wide region along the Galactic plane between Galactic Longitudes 25° and 45° (see Fig. 4.4). It is partially masked by the satellites band on the East (declination range $-4 - 0^{\mathrm{o}}$), and it is located next to the W49 QUIJOTE field on the West. The strongest sources are two big molecular complexes (W43 and W47) and a SNR (W44).

W43 is a coherent molecular and star-forming complex, encompassing more than 20 molecular clouds with high velocity dispersions (Nguyen Luong et al., 2011), surrounded by atomic gas out to an extent of approximately 290 pc. The total mass of the complex is around $7 \cdot 10^6$ solar masses and is located around Galactic coordinates $l = 30.5^{\mathrm{o}}, b = -0.1^{\mathrm{o}}$ at a distance of 5.5 kpc from the Sun, with an angular extension of approximately 1° (Génova-Santos et al., 2017). The core of W43 harbours a well-known giant HII region powered by a particularly luminous cluster of Wolf-Rayet OB stars (Blum et al., 1999). The expected emission is practically unpolarised at low frequencies, since it is mainly a combination of free-free and AME, while the synchrotron is negligible.

W44 is a SNR with a mixed morphology characterised by a bright non-thermal shell-like radio structure and a centrally-concentrated thermal X-ray emission (Rho & Petre, 1998), surrounded by six giant molecular clouds partially interacting with it. It is located at (l, b)=$(34.7°, -0.4°)$ at a solar distance of ~ 3.1 kpc and has an angular extension of approximately 0.5°. Its spectrum should be dominated by synchrotron emission, both in intensity and polarisation.

W47 is formed by 7 molecular clouds (Paladini et al., 2003) at a distance of 9.6 kpc (Bania et al., 2012), with an angular extension of approximately 6-9 arcmin.

In this section, we will present the SEDs of the three sources described above. The data used for the calculations are those described in chapter 4, that is the QUIJOTE data between 11 GHz and 19 GHz, the WMAP data up to 94 GHz, the Planck data up to 857 GHz and the lower frequencies of DIRBE.

The data are fitted assuming that each data point is the sum of the four components described in section 5.2.4, although the synchrotron emission in W43 and W47 is ignored since it is expected to be much lower than the free-free emission. On the contrary, the free-free component has not been fitted in the W44 analysis. Figs. 5.1, 5.2 and 5.3 show the SEDs of W43, W44 and W47, respectively. The parameters obtained from these fits are presented in table 5.4.

The SED of W43 and W47 are quite similar, as expected. At low frequency the emission is dominated by free-free, while at approximately 10 GHz the contribution from the AME begins to be comparable, producing a small bump in the spectrum. At high frequencies (> 100 GHz) the emission is fully dominated by the thermal emission of the dust, whose peak is a factor $10^4 - 10^5$ larger than the peak of the AME emission. All the parameters of the fit are consistent with typical values found in literature, with the exception of the emission measure, which is almost 3 orders of magnitude lower due to the dilution over the beam, as expected since the effect of the integration over the aperture is a factor $\Omega_{\rm source}/\Omega_{\rm aperture}$. The only data point that does not agree well with the fit is the 2.36 GHz in W43 (Fig. 5.1) which has not been considered in the fit since it is an outlier (this happens also in the W49 region, see next section). This map and the Reich map at 1.42 GHz are calibrated using the full beam solid angle, thus flux densities calculated from sources with an angular extension smaller than the beam size are usually underestimated due to the presence of sidelobes. For this reason, the factors 1.45 and 1.55 are used to correct these maps, respectively (see subsection 5.1), which have been derived for point sources. However, W43 has an angular extension of approximately 1°, which probably makes the correction overestimated.

The SED of W44 instead shows a strong synchrotron component at low

Survey	Freqs (GHz)	W43 (Jy)	W44 (Jy)	W47 (Jy)
Haslam	0.41	502± 68	540± 72	246± 44
Dwingeloo	0.82	445± 18	381± 15	214± 14
Reich	1.42	388± 67	328± 63	197± 56
HartRao	2.33	571± 50	314± 37	186± 31
Urumqi	4.80	492± 13	237± 9	163± 8
QUIJOTE H1	11.23	536± 29	192± 13	174± 11
QUIJOTE H3	11.16	512± 29	203± 13	179± 12
QUIJOTE H1	12.84	574± 31	204± 14	183± 12
QUIJOTE H3	12.89	543± 31	213± 14	181± 13
QUIJOTE H2	16.75	578± 33	211± 14	189± 13
QUIJOTE H4	17.00	545± 31	207± 14	182± 13
QUIJOTE H2	18.71	593± 35	219± 15	193± 13
QUIJOTE H4	19.00	574± 33	212± 15	186± 13
WMAP	22.69	544± 14	198± 9	181± 8
Planck	28.40	534± 14	187± 9	172± 8
WMAP	32.94	519± 13	176± 8	165± 7
WMAP	40.62	478± 12	157± 7	148± 6
Planck	44.10	464± 12	151± 7	145± 6
WMAP	60.52	431± 11	141± 7	142± 6
Planck	70.40	443± 11	150± 7	151± 7
WMAP	92.99	570± 16	222± 12	219± 12
Planck	100.00	904± 30	428± 23	361± 24
Planck	143.00	1325± 44	617± 37	588± 41
Planck	217.00	6311± 229	3291± 194	2859± 211
Planck	353.00	27289± 974	13884± 836	12648± 912
Planck	545.00	103412± 3622	49722± 3043	46581± 3242
Planck	857.00	379652± 12997	167415± 10484	162994± 10658
Dirbe	1249.14	957009± 31794	376620± 24504	387635± 23417
Dirbe	2141.37	1740200± 55455	575406± 39080	616658± 33671
Dirbe	2997.92	1000310± 29146	276340± 18677	296929± 14434
Dirbe	4996.54	384874± 9636	85376± 5447	97369± 3759

TABLE 5.2— Flux densities in total intensity of the three sources in the W44 field (W43,W44,W47).

Survey	Freqs (GHz)	Q (Jy)	U (Jy)	P (Jy)	γ (°)
Urumqi	4.80	-4.92± 0.33	1.13± 0.26	5.04± 0.37	-83.50± 1.45
QUIJOTE H1	11.23	-5.16± 0.56	4.55± 0.44	6.86± 0.67	-69.32± 2.04
QUIJOTE H3	11.16	-7.85± 0.54	4.79± 0.42	9.18± 0.73	-74.31± 1.18
QUIJOTE H1	12.84	-6.09± 0.37	8.00± 0.47	10.04± 0.83	-63.63± 0.86
QUIJOTE H3	12.89	-5.42± 0.40	5.80± 0.43	7.93± 0.72	-66.53± 1.15
QUIJOTE H2	16.75	-4.95± 0.29	5.49± 0.32	7.39± 0.65	-66.01± 0.92
QUIJOTE H4	17.00	-1.62± 0.15	2.84± 0.15	3.26± 0.29	-59.84± 0.93
QUIJOTE H2	18.71	-4.26± 0.27	5.79± 0.34	7.18± 0.63	-63.17± 0.87
QUIJOTE H4	19.00	-2.63± 0.33	6.79± 0.39	7.27± 0.62	-55.58± 1.34
WMAP	22.69	-2.59± 0.13	5.72± 0.09	6.27± 0.45	-57.17± 0.28
Planck	28.40	-2.26± 0.09	5.47± 0.07	5.92± 0.42	-56.20± 0.22
WMAP	32.94	-1.67± 0.10	4.94± 0.05	5.21± 0.37	-54.36± 0.24
WMAP	40.62	-1.44± 0.09	4.46± 0.06	4.69± 0.33	-53.94± 0.27
Planck	44.10	-1.07± 0.09	4.19± 0.04	4.33± 0.30	-52.16± 0.27
WMAP	60.52	-0.44± 0.10	3.31± 0.06	3.34± 0.23	-48.83± 0.87
Planck	70.40	-0.54± 0.14	3.12± 0.04	3.17± 0.22	-49.93± 1.21
WMAP	92.99	1.58± 0.31	0.38± 0.16	1.62± 0.19	-6.75± 3.09

TABLE 5.3— Polarisation flux (Q,U,P) and polarisation angle (γ) of W44, which is the only polarised source in the W44 field. The measurements from different horns of the MFI are not consistent, especially between horn 2 and horn 4. This can be caused by systematics errors still unknown. In any case the error bars are underestimated and do not take this into account.

Parameter	W43	W44	W47
EM (pc·cm^{-6})	5324 ± 171	—	2110 ± 45
A^{ff}_{1GHz} (Jy)	488 ± 32	—	193 ± 11
A^{sync}_{1GHz} (Jy)	—	369 ± 21	—
β^{sync}	—	-0.32 ± 0.04	—
A^{AME}_{max} (Jy)	231 ± 17	62 ± 16	50 ± 5
ν^{AME}_{peak} (GHz)	19.27 ± 2.34	21.96 ± 4.76	19.96 ± 1.59
m_{60}	2.00 ± 0.00	2.78 ± 6.35	4.86 ± 2.11
T^{dust} (K)	21.57 ± 0.75	19.68 ± 0.88	19.32 ± 0.51
β^{dust}	1.73 ± 0.06	1.70 ± 0.09	1.82 ± 0.06
$\tau^{dust}_{250} \cdot 10^3$	4.55 ± 0.64	2.46 ± 0.46	2.69 ± 0.32
χ^2_{red}	7.95	3.81	1.87
β^{sync}_{pol}	—	-0.59 ± 0.01	—
A^{sync}_{pol} (Jy)	—	41 ± 2	—
χ^2_{red}	—	2.6	—
γ_0(°)	—	39.5 ± 1.4	—
RM (rad m^{-2})	—	-691 ± 204	—
χ^2_{red}	—	0.25	—

TABLE 5.4— Fit parameters for the intensity SED of W43, W44 and W47. Fit parameters of the polarisation SED of W44 and of its Faraday rotation.

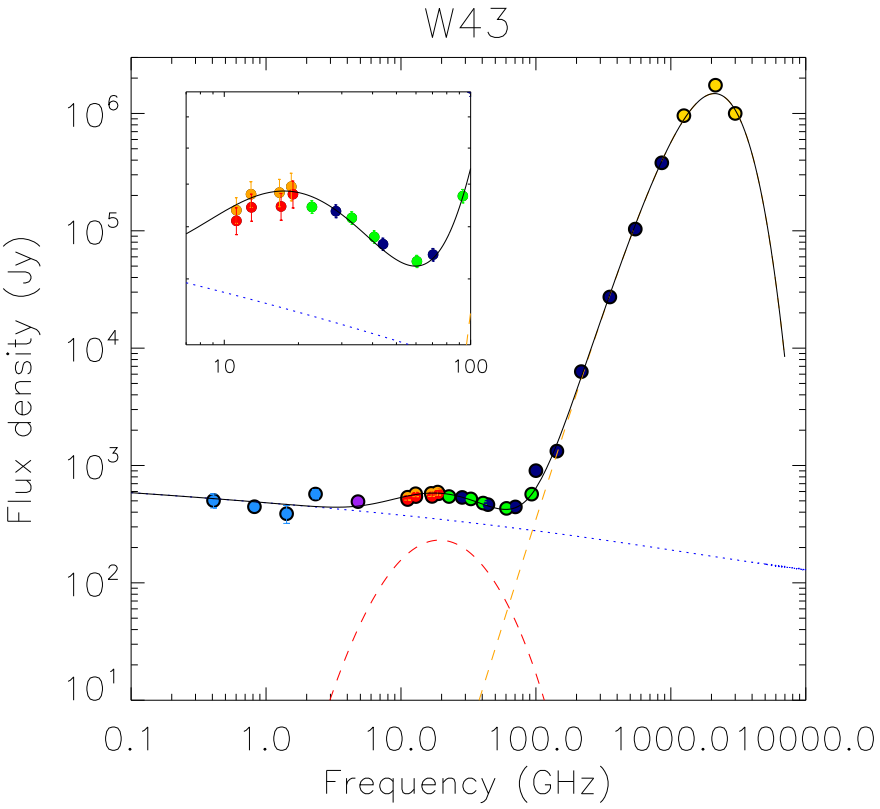

FIGURE 5.1— Spectral Energy Distribution of W43 and fit to the main components: free-free (blue), AME (red) and thermal dust (orange). QUIJOTE points are marked in orange and red to differentiate the two independent measurements at each frequency. The colours of the other points represent the different surveys: WMAP (green), Urumqi (purple), Planck (blue), and DIRBE (yellow). No synchrotron emission has been considered in the fit.

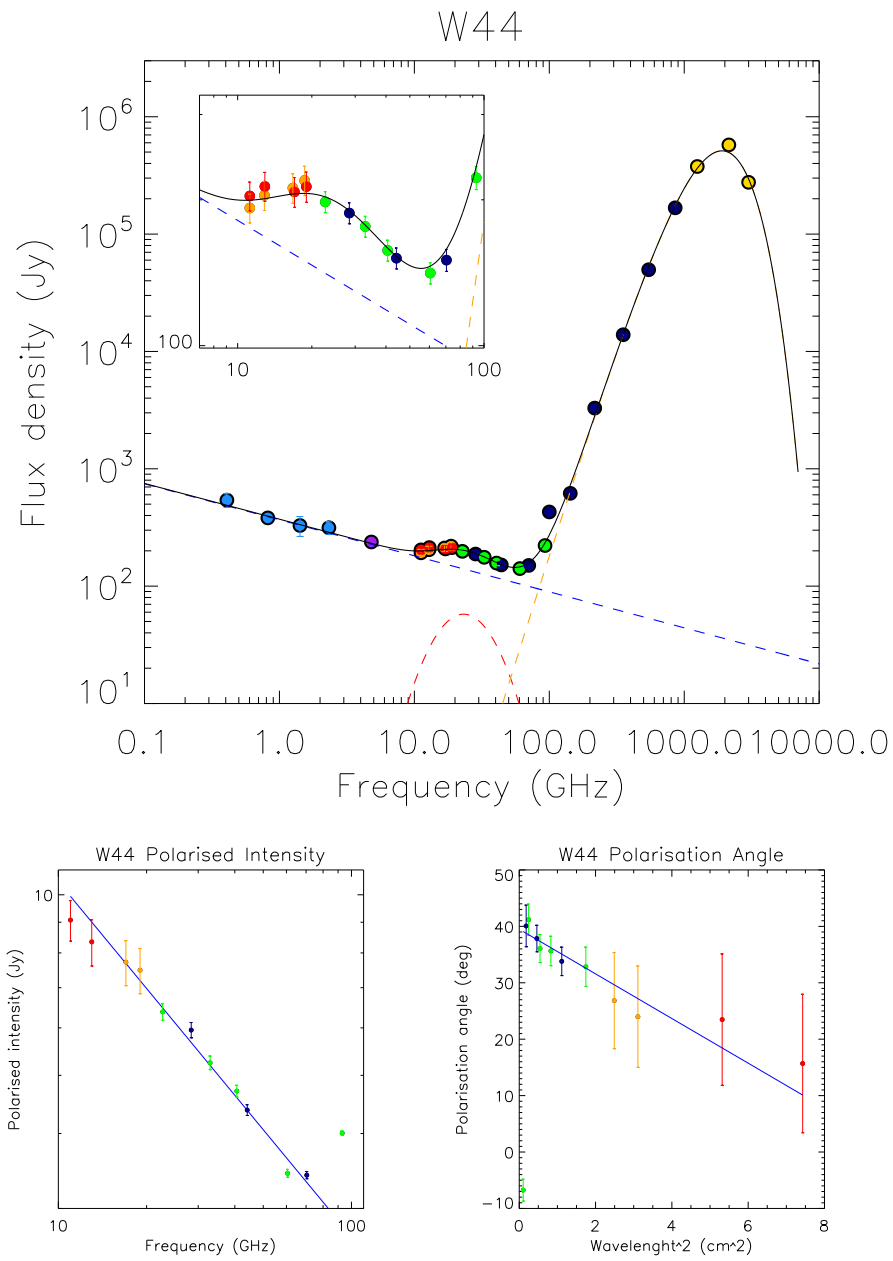

FIGURE 5.2— Top panel: Spectral Energy Distribution of W44 and fit to the main components: synchrotron (blue), AME (red) and thermal dust (orange). QUIJOTE points are marked in orange and red to differentiate the two independent measurements at each frequency. The colours of the other points represent the different surveys: WMAP (green), Urumqi (purple), Planck (blue), and DIRBE (yellow). No free-free emission has been considered in the fit. Bottom left panel: Polarisation SED and fit of the synchrotron. Bottom right panel: polarisation angle vs λ^2 and corresponding fit for the Faraday rotation model.

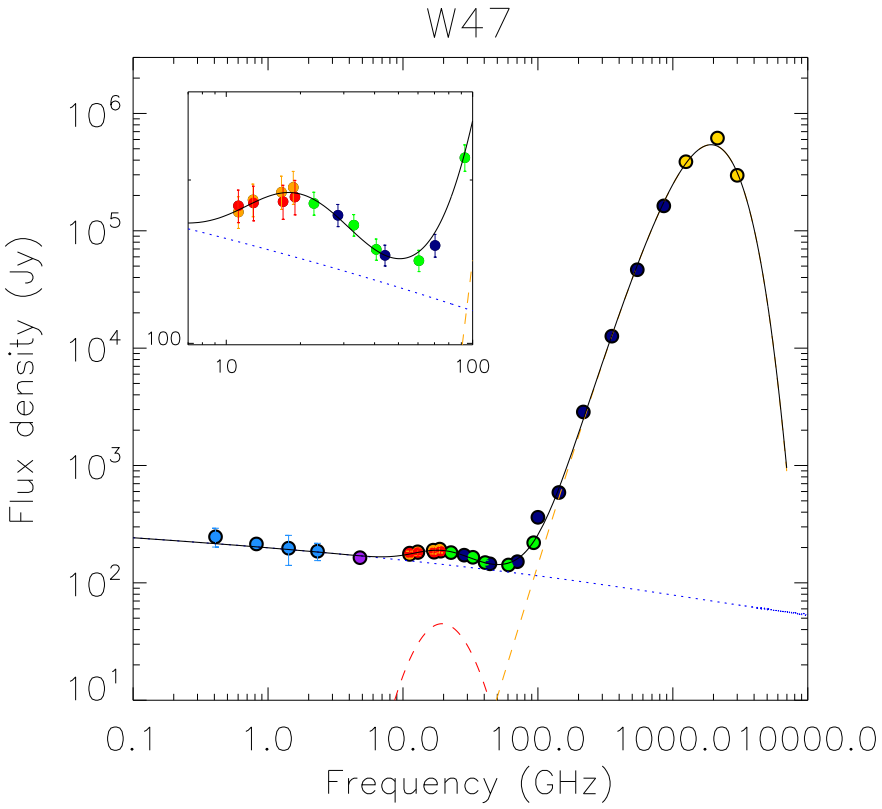

FIGURE 5.3— Spectral Energy Distribution of W47 and fit to the main components: free-free (blue), AME (red) and thermal dust (orange). QUIJOTE points are marked in orange and red to differentiate the two independent measurements at each frequency. The colours of the other points represent the different surveys: WMAP (green), Urumqi (purple), Planck (blue), and DIRBE (yellow). No synchrotron emission has been considered in the fit.

frequencies, since it is a SNR, as shown in the top panel of Fig. 5.2. The synchrotron spectral index $\beta^{\rm sync}$ is -0.32 ± 0.04, which is a flatter value than typical indexes (-0.6 or less). This is probably due to free-free emission coming from the backgrounds, since the aperture photometry disc is twice the size of the source. A better approach would be the simultaneous fit of synchrotron and free-free, but, if we do not fix the synchrotron spectral index, the fit is quite degenerate since both spectra follow a power law distribution. Hence, in order to obtain estimates of the synchrotron parameters independent of eventual free-free contamination, we fitted also the polarisation map. The fit of the data between 11 GHz and 73 GHz (points below 11 GHz are excluded because of Faraday depolarisation, and points above 73 GHz are affected by dust contamination) shows a spectral index of -0.59±0.01, which is compatible with the typical values found in literature. The polarisation amplitude at 1 GHz of 41±2 Jy, when compared with the intensity amplitude (369±21 Jy) gives a polarisation fraction of 11.1±1.1 %. Actually, this is a lower limit since the amplitude in intensity include both a synchrotron and a free-free components, but, given that the synchrotron emission is stronger than the free-free emission, the polarisation fraction cannot be much larger. Finally, the derived rotation measure is -691±204 rad/m^2, which is higher (in absolute value) than typical values along the Galactic plane, although in some specific regions it reaches -1200 rad/m^2.

5.4 W49 Field

The W49 QUIJOTE field is located next to the W44 field, between $l \sim 35^{\rm o}$ and $l \sim 55^{\rm o}$. The main sources in this field are W47[8], W49 and W51 (see Fig. 4.3.

W49 is one of the most luminous massive star-forming regions in our Galaxy. It was discovered in 1958 (Westerhout, 1958) and was shown to present a radio continuum emission characteristic of an HII region. This subregion of W49 was called W49A. Another non-thermal component was found in 1967 and was associated with a SNR called W49B (Mezger et al., 1967). A very massive star (more than 100 solar masses) was found in the central cluster of the complex (Wu et al., 2014). It is located at 11.1 kpc from the Sun inside a giant molecular cloud of $M_{\rm gas} \sim 10^6$ solar masses that extends over 100 pc.

W51 is a giant molecular cloud which hosts another of the most luminous massive star-forming regions in our Galaxy. It is a complex containing three main regions, named A, B, and C. While W51C is a SNR, the radio emission of W51A and W51B are due to approximately 20 HII regions (Ginsburg, 2017), with electron temperatures of ≈ 7500 K. W51A also hosts two luminous high-

[8]W47 is located at the edge of the map and it is not visible in all the horns of the MFI.

mass protostars (Koch et al., 2018) and is one of the most adequate sources to study the interaction of a SNR with a high-mass star forming region. W51A and B are located at a distance of $\approx 5-8\,\mathrm{kpc}$ while W51C is at $\approx 4-6\,\mathrm{kpc}$ (Zhang et al., 2017), and the total extension of the complex is $\approx 30\,\mathrm{arcmin}$ and therefore it is not possible to separate the three regions with the data analysed here.

The parameters of the fit of the SEDs of W49 and W51 are presented in table 5.7. The SED of W49 (Fig. 5.4) presents evidence of AME, free-free emission and thermal dust. The source does not show visible polarised emission.

The intensity SED of W51 (Fig. 5.5, top) does not present AME emission, nor synchrotron emission[9]. In principle, this is unexpected, since the SNR W51C is inside the aperture and is well visible in the polarisation map. The synchrotron amplitude in polarisation at 1 GHz is determined from the fit to be $29 \pm 1\,\mathrm{Jy}$, well detectable with QUIJOTE, but, if we suppose a polarisation fraction of the synchrotron of 10%, we expect an intensity contribution of 290 Jy, which is less than the 50% of the total intensity at 1 GHz. Therefore, the synchrotron emission in intensity may be over-shadowed by the free-free emission. There are no hints of AME since the fit gave two parameters (m_{60} and $\nu_{\mathrm{peak}}^{\mathrm{AME}}$) equal to their lower admissible limit (2 and 15 GHz, respectively) and an amplitude compatible with zero (at $3\,\sigma$). For this and the following reasons, the $\chi^2_{\mathrm{red}} = 12.52$ is significantly larger than 1. We note that the points from Reich and Urumqi are off the model. This could be due to calibration errors in the region, since, if we had omitted these points, we could have fitted the points at 0.41, 0.82 and 1.42 GHz with a pure synchrotron both in this source and in W49. Although this fit is quite good ($\chi^2_{\mathrm{red}} = 1.56$), and the fact that no polarised signal is detected does not suggest that this hypothesis is correct. Another possible explanation is that the turn-over frequency ν_0 of the free-free emission in this region was around 2 GHz. In this case, the synchrotron emission would dominate at frequencies below 2 GHz, while the free-free would be responsible for the majority of the emission at frequencies between 2 and 10 GHz. The turn-over frequency depends on three parameters: the EM, which is the fitted parameter, the electron temperature T_e (see Eq. 5.14) and on the dilution factor $\Omega_{\mathrm{ff}} \approx \Omega_{\mathrm{source}}/\Omega_{\mathrm{aperture}}$, which corrects the EM for the difference between the size of the source and the size of the aperture. If we do not take the Ω_{ff}, the turn-over frequency is of the order of 0.1 GHz, which is below the range of frequencies considered in this work. However, the simultaneous fit with the three free parameters of the free-free component and the two parameters of

[9] A fit with synchrotron has been attempted, but the best fit gave a spectral index of -0.16, which is indicative of free-free emission.

Survey	Freqs (GHz)	W49 (Jy)	W51 (Jy)
Haslam	0.41	222± 39	434± 59
Dwingeloo	0.82	166± 9	417± 9
Reich	1.42	132± 53	352± 63
HartRao	2.33	162± 28	557± 47
Urumqi	4.80	153± 5	481± 6
QUIJOTE H1	11.23	148± 9	380± 19
QUIJOTE H3	11.16	158± 10	—
QUIJOTE H1	12.84	159± 10	382± 19
QUIJOTE H3	12.89	165± 11	—
QUIJOTE H2	16.75	178± 11	387± 20
QUIJOTE H4	17.00	168± 11	362± 19
QUIJOTE H2	18.71	182± 12	394± 20
QUIJOTE H4	19.00	173± 11	370± 19
WMAP	22.69	162± 7	341± 6
Planck	28.40	149± 6	330± 5
WMAP	32.94	145± 6	326± 5
WMAP	40.62	135± 5	308± 5
Planck	44.10	132± 5	302± 4
WMAP	60.52	129± 5	286± 5
Planck	70.40	137± 6	284± 5
WMAP	92.99	186± 10	307± 8
Planck	100.00	298± 20	382± 14
Planck	143.00	497± 33	484± 27
Planck	217.00	2288± 165	1736± 128
Planck	353.00	9862± 704	7196± 565
Planck	545.00	35717± 2489	26659± 1989
Planck	857.00	118292± 8158	94158± 6454
Dirbe	1249.14	263712± 17896	235349± 14041
Dirbe	2141.37	411836± 25528	480184± 20435
Dirbe	2997.92	212434± 11239	356706± 9342
Dirbe	4996.54	87732± 3262	220585± 2831

TABLE 5.5— Flux densities in total intensity of two sources the W49 field (W49,W51). The W51 QUIJOTE data from horn 3 have been deleted since the source is only partially covered by the map. Horns 2 and 4 show discrepancies as in the other polarisation maps. We do not know the reason, but the errors are probably underestimated.

Survey	Freqs (GHz)	Q (Jy)	U (Jy)	P (Jy)	γ (°)
Urumqi	4.80	-3.37± 0.34	2.59± 0.19	4.24± 0.25	-71.20± 1.77
QUIJOTE H1	11.23	-3.05± 0.16	-2.11± 0.15	3.71± 0.34	72.66± 0.80
QUIJOTE H3	11.16	—	—	—	—
QUIJOTE H1	12.84	-4.74± 0.27	-1.90± 0.14	5.10± 0.45	79.06± 0.57
QUIJOTE H3	12.89	—	—	—	—
QUIJOTE H2	16.75	-5.16± 0.26	-2.17± 0.14	5.60± 0.48	78.59± 0.54
QUIJOTE H4	17.00	-3.88± 0.20	-3.11± 0.17	4.98± 0.44	70.64± 0.64
QUIJOTE H2	18.71	-5.06± 0.27	-2.32± 0.16	5.57± 0.46	77.69± 0.62
QUIJOTE H4	19.00	-6.27± 0.32	-7.76± 0.40	9.97± 0.88	64.48± 0.67
WMAP	22.69	-3.38± 0.05	-1.98± 0.03	3.91± 0.28	74.85± 0.16
Planck	28.40	-4.19± 0.05	-0.56± 0.03	4.23± 0.31	86.18± 0.17
WMAP	32.94	-3.30± 0.05	-1.34± 0.02	3.56± 0.27	78.96± 0.10
WMAP	40.62	-3.05± 0.05	-1.08± 0.02	3.23± 0.23	80.21± 0.14
Planck	44.10	-2.90± 0.04	-0.99± 0.03	3.06± 0.21	80.53± 0.27
WMAP	60.52	-2.39± 0.06	-1.02± 0.05	2.60± 0.19	78.48± 0.47
Planck	70.40	-2.69± 0.04	-0.87± 0.04	2.83± 0.20	81.07± 0.35
WMAP	92.99	0.01± 0.13	-1.16± 0.13	1.15± 0.12	44.84± 3.20

TABLE 5.6— Polarisation flux (Q,U,P) and polarisation angle of W51, which is the only polarised source in the W49 field. The W51 QUIJOTE data from horn 3 have been deleted since the source is only partially covered by the map.

Parameter	W49	W51
EM (pc·cm^{-6})	1886 ± 34	4944 ± 99
A^{ff}_{1GHz} (Jy)	173 ± 10	453 ± 26
A^{AME}_{max} (Jy)	46 ± 4	—
ν^{AME}_{peak} (GHz)	19.95 ± 1.30	—
m_{60}	5.11 ± 1.77	—
T^{dust} (K)	19.76 ± 0.52	22.03 ± 1.67
β^{dust}	1.72 ± 0.05	1.86 ± 0.17
$\tau^{dust}_{250} \cdot 10^3$	1.76 ± 0.20	1.18 ± 0.38
χ^2_{red}	1.56	12.52
β^{sync}_{pol}	—	-0.60 ± 0.01
A^{sync}_{pol} (Jy)	—	29 ± 1
χ^2_{red}	—	12
γ_0(°)	—	-8.58 ± 0.50
RM (rad m^{-2})	—	-161 ± 71
χ^2_{red}	—	10

TABLE 5.7— Fit parameters for the intensity SED of W49 and W51. Fit parameters of the polarisation SED of W51 and of its Faraday rotation.

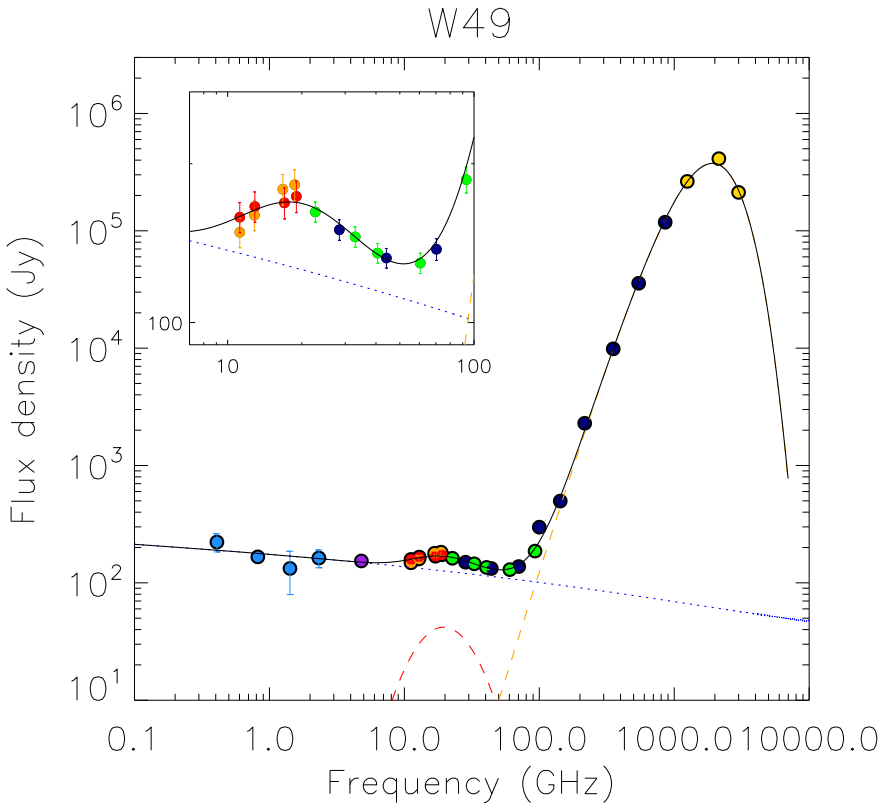

FIGURE 5.4— Spectral Energy Distribution of W49 and fit to the principal components: free-free (blue), AME (red) and thermal dust (orange). QUIJOTE points are marked in orange and red to differentiate the two independent measurements at each frequency. The colours of the other points represent the different surveys: WMAP (green), Urumqi (purple), Planck (blue), and DIRBE (yellow).

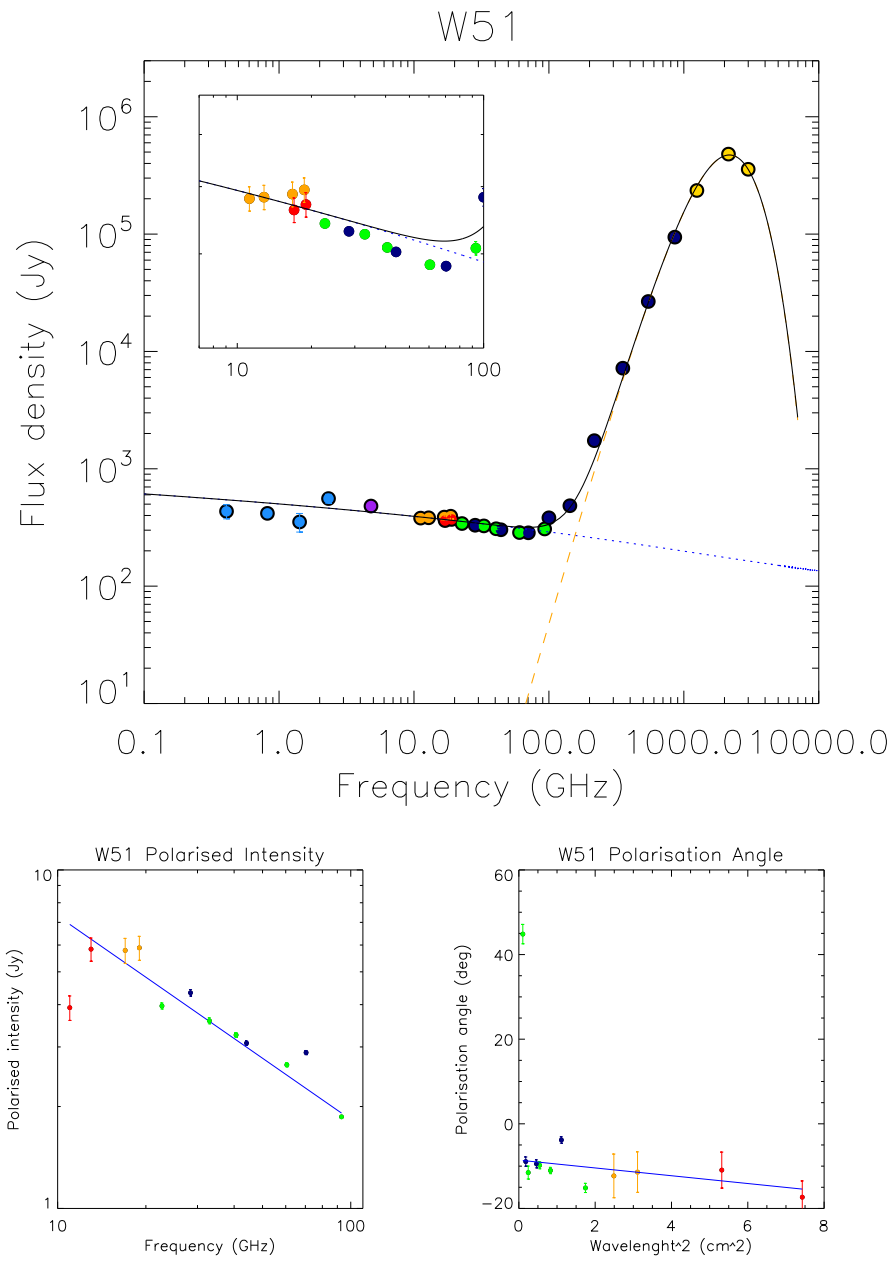

FIGURE 5.5— Spectral Energy Distribution of W51 and fit to the principal components: free-free (blue), AME (red) and thermal dust (orange). QUIJOTE points are marked in orange and red to differentiate the two independent measurements at each frequency. The colours of the other points represent the different surveys: WMAP (green), Urumqi (purple), Planck (blue), and DIRBE (yellow). Bottom left panel: Polarisation SED and fit of the synchrotron. Bottom right panel: polarisation angle vs λ^2 and corresponding fit for the Faraday rotation model.

the synchrotron is degenerate given the number of available data points below 10 GHz.

The QUIJOTE point in the polarisation SED (Fig. 5.5, bottom left panel) at 11 GHz is clearly an outlier (see also table 5.6 and compare with the Urumqi point: if the Faraday depolarisation was the cause of the low flux at 11 GHz, we will have lower fluxes at 4.8 GHz), thus it is discarded from the polarised intensity fit. Actually, polarisation data from horn 1 are less reliable than data from other horns because the polar modulator is fixed, and this causes a systematic error described in López-Caraballo (2013). Also, the data from horn 3 for this source are not available since it is located at the edge of the map (the centre of the region is W49, which had more importance when deciding the observation strategy since it hosts a stronger AME emission). Data from the horns 2 and 4 are incompatible. The reason for this is still unknown, but this inconsistency is present in the polarisation of all the polarised sources presented in this chapter, thus we think that it is a systematic effect. Also, as mentioned in subsection 5.2.2, the errors are being underestimated since we are not taking into account the correlation between pixels in the same beam. However, this effect is not sufficiently strong to explain the discrepancies between the two horns. Finally, the two Planck points at 28 GHz and 70 GHz are above the average of the fit. This can be caused by the leakage from intensity since they are the two most affected frequencies.

5.5 W63 Field

The W63 region covers two extended sources: the W63 SNR and the Cygnus X complex (see Fig. 4.2). W63 is an elliptical shaped shell-type SNR located 5.3º north of the Cygnus complex (Gao et al., 2011). The area is characterised by strong diffuse Galactic background emission, as well as filamentary structures.The filaments present unpolarised thermal emission at low frequency, which differ from the SNR that is highly polarised and the only polarised source visible in the field. Cygnus X is a massive star-forming region located at 1.4 kpc from the Sun. Its size is about 200 pc and is associated with a molecular cloud with a mass of approximately $3 \cdot 10^6$ solar masses. In addition it hosts several HII regions and a radio galaxy (Cyg A) is visible behind.

The SED of W63 (Fig. 5.6, top panel) is mainly characterised by a strong synchrotron spectrum and thermal dust emission. The fit also has hints for the presence of AME emission, but with a very low amplitude (the peak is $\sim$6 Jy). However, the spectral index of the synchrotron emission is higher than its typical values (-0.35 instead of -0.6). This is probably due to contamination from free-free emission, either from the source or from the background. The

Survey	Freqs (GHz)	W63 (Jy)
Haslam	0.41	141± 30
Dwingeloo	0.82	99± 6
Reich	1.42	92± 52
HartRao	2.33	0± 18
Urumqi	4.80	24± 5
QUIJOTE H1	11.23	43± 4
QUIJOTE H3	11.16	46± 5
QUIJOTE H1	12.84	43± 4
QUIJOTE H3	12.89	44± 4
QUIJOTE H2	16.75	42± 4
QUIJOTE H4	17.00	30± 4
QUIJOTE H2	18.71	40± 4
QUIJOTE H4	19.00	23± 3
WMAP	22.69	34± 3
Planck	28.40	31± 3
WMAP	32.94	30± 3
WMAP	40.62	28± 3
Planck	44.10	27± 3
WMAP	60.52	24± 3
Planck	70.40	22± 3
WMAP	92.99	22± 5
Planck	100.00	19± 6
Planck	143.00	33± 11
Planck	217.00	98± 44
Planck	353.00	523± 185
Planck	545.00	1795± 621
Planck	857.00	5895± 1871
Dirbe	1249.14	12732± 3836
Dirbe	2141.37	27527± 5974
Dirbe	2997.92	13112± 3465
Dirbe	4996.54	4637± 1582

TABLE 5.8— Flux densities in total intensity of W63.

Survey	Freqs (GHz)	Q (Jy)	U (Jy)	P (Jy)	γ (^{o})
Urumqi	4.80	0.92± 0.05	0.54± 0.02	1.07± 0.18	-15.32± 1.03
QUIJOTE H1	11.23	2.71± 0.15	6.64± 0.36	7.17± 0.49	-33.91± 0.58
QUIJOTE H3	11.16	3.14± 0.16	6.07± 0.33	6.83± 0.48	-31.31± 0.68
QUIJOTE H1	12.84	3.58± 0.21	5.30± 0.28	6.39± 0.44	-27.97± 0.78
QUIJOTE H3	12.89	3.84± 0.20	5.76± 0.31	6.92± 0.49	-28.16± 0.76
QUIJOTE H2	16.75	1.89± 0.11	3.67± 0.19	4.13± 0.28	-31.35± 0.69
QUIJOTE H4	17.00	0.87± 0.05	2.09± 0.12	2.27± 0.15	-33.66± 0.72
QUIJOTE H2	18.71	3.41± 0.32	3.81± 0.26	5.10± 0.35	-24.09± 1.20
QUIJOTE H4	19.00	3.00± 0.18	3.50± 0.20	4.61± 0.30	-24.71± 0.94
WMAP	22.69	2.48± 0.03	3.52± 0.06	4.31± 0.19	-27.45± 0.24
Planck	28.40	2.05± 0.03	2.94± 0.04	3.59± 0.16	-27.58± 0.23
WMAP	32.94	1.83± 0.03	2.50± 0.05	3.10± 0.13	-26.85± 0.29
WMAP	40.62	1.37± 0.02	2.19± 0.04	2.58± 0.12	-28.93± 0.26
Planck	44.10	1.47± 0.02	2.13± 0.03	2.59± 0.11	-27.74± 0.24
WMAP	60.52	0.91± 0.04	2.29± 0.07	2.47± 0.10	-34.16± 0.39
Planck	70.40	1.35± 0.04	1.25± 0.02	1.84± 0.08	-21.37± 0.46
WMAP	92.99	2.45± 0.19	0.77± 0.13	2.56± 0.16	-8.77± 1.46

TABLE 5.9— Polarisation flux (Q,U,P) and polarisation angle of W63.

Parameter	W63
A^{sync}_{1GHz} (Jy)	93 ± 2
β^{sync}	-0.35 ± 0.01
A^{AME}_{max} (Jy)	6 ± 1
ν^{AME}_{peak} (GHz)	16.58 ± 7.24
m_{60}	3.60 ± 6.56
T^{dust} (K)	19.87 ± 1.26
β^{dust}	1.88 ± 0.16
$\tau^{dust}_{250} \cdot 10^3$	0.09 ± 0.03
χ^2_{red}	0.25
β^{sync}_{pol}	-0.62 ± 0.01
A^{sync}_{pol} (Jy)	28 ± 1
χ^2_{red}	281
$\gamma_0(^o)$	-27.02 ± 0.49
RM (rad m^{-2})	-115 ± 84
χ^2_{red}	9.4

TABLE 5.10— Fit parameters for the intensity SED of W63. Fit parameters of the polarisation SED of W63 and of its Faraday rotation.

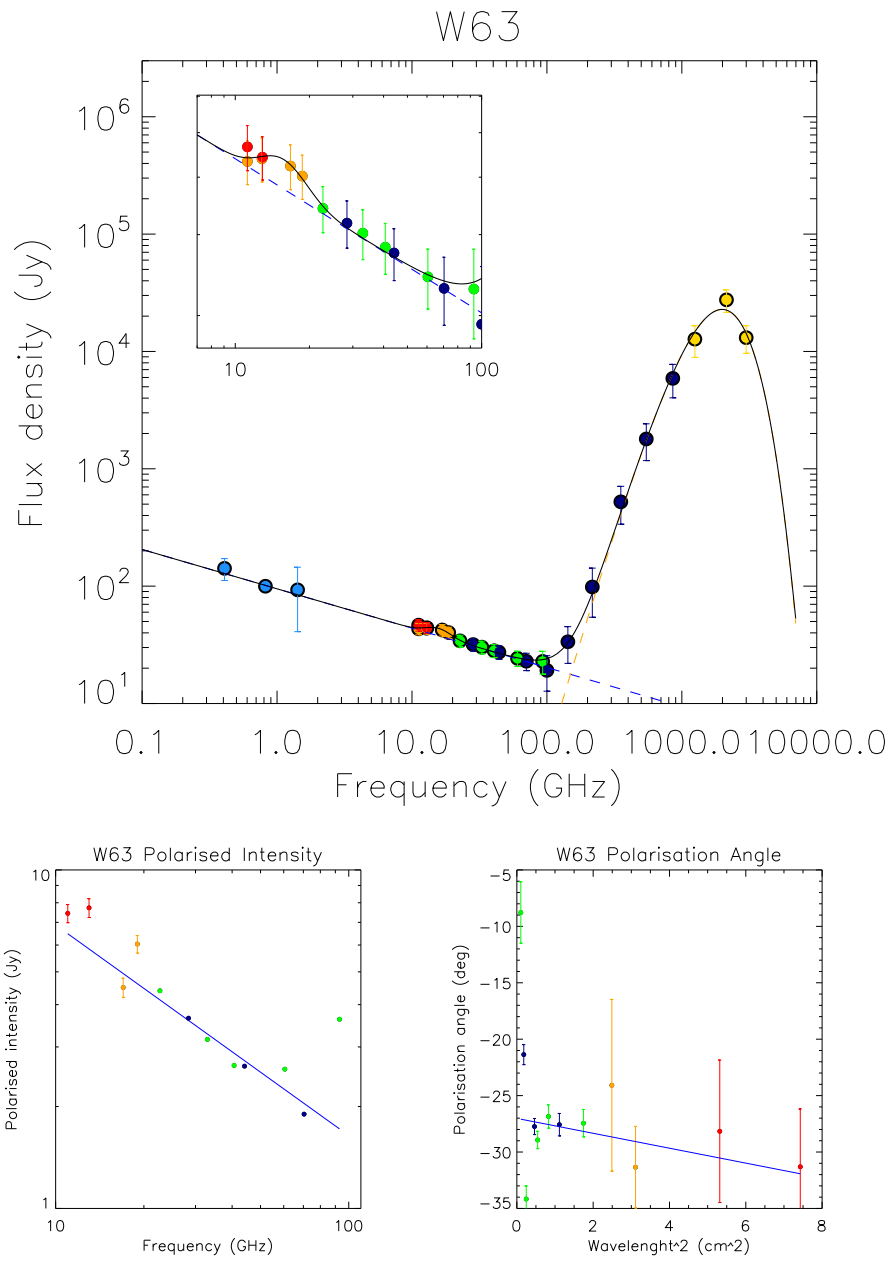

FIGURE 5.6— Spectral Energy Distribution of W63 and fit to the principal components: synchrotron (blue), AME (red) and thermal dust (orange). QUIJOTE points are marked in orange and red to differentiate the two independent measurements at each frequency. The colours of the other points represent the different surveys: WMAP (green), Planck (blue), and DIRBE (yellow). No free-free emission has been used for the fit. Bottom left panel: Polarisation SED and fit of the synchrotron. Bottom right panel: polarisation angle vs λ^2 and corresponding fit for the Faraday rotation model.

latter case is more likely since the source has an elliptical shape and this fact is not taken into account in the aperture, which is perfectly circular. We did not include the points from the Urumqi and HartRAO surveys since W63 lies outside those maps. Also we did not include the points from horn 4 of the MFI, since they are not consistent with the values from horn 2 (differences of $\approx 3\sigma$s) and we know that horn 2 had a better performance than horn 4. We also note that this inconsistency is also shown at 17 GHz in polarisation.

The fit in polarised intensity reveals a synchrotron component with $\beta_{\rm pol}^{\rm sync} = -0.62 \pm 0.01$ and a polarisation fraction of 30±2%, which is quite high and significant of strong aligned magnetic fields. However, the $\chi^2_{\rm red}$ is very large ($\approx$ 280), probably due to an underestimation of the errors and to the inconsistency of some of the QUIJOTE points: the data point at 13 GHz presents a larger flux than the one at 11 GHz, although compatible within the errors, while the data points at 17 GHz and 19 GHz are inconsistent. Finally, the points from WMAP and Planck seem to follow two different spectral distributions, with the point at 94 GHz being excluded from the fit because of contamination from polarised emission from thermal dust.

5.6 The Haze

5.6.1 Description of the Region

The region addressed in this section is one of the largest QUIJOTE fields, covering an area of 700 square degrees, and extends from the Galactic centre (visible in the maps of horn 3) to the satellite band, which separates it from the W44 field (see Fig. 4.5). It was the first region in which polarised diffuse emission was detected with the MFI. In intensity, seven sources have been identified (see table 4.2). Their flux densities and SEDs are presented in Figs. A.7-A.6. None of them presents sufficient polarisation to be distinguished from the background, so their polarisation analysis is omitted.

However, the main interest in the observations of this region is the diffuse emission. Finkbeiner (2004a), after a component separation of WMAP data, discovered an extended region around the Galactic centre characterised by a hard synchrotron spectrum. As the spectral index is directly related to the energy distribution of the electrons (see subsection 1.4.3), the origin of this amount of energy became a topic of interest, especially since the one of the first proposed explanations was dark matter (DM) annihilation processes (Finkbeiner, 2004b). Thanks to the diffuse nature of the emission it has been called "Galactic Haze". In 2010, gamma rays observations by Fermi-LAT revealed a structure around the Galactic centre made of two big lobes (the so-called "Fermi bubbles") stretching to Galactic latitudes $|b| \sim 55^{\rm o}$, that was later associated with

the Microwave Haze (Dobler, 2012b,a; Yang et al., 2014), although their extension was much larger than their microwave counterpart, which covers an area between $b \sim -35^{\circ}$ and $b \sim +35^{\circ}$. However, Carretti et al. (2013) found that the polarisation emission of the Haze at 2.3 GHz extended up to $|b| \sim 60^{\circ}$, with a total flux in intensity of ≈ 21 kJy and an average polarisation fraction of 25% at $|b| > 15^{\circ}$. In intensity, the authors measured spectral indexes which ranged between -1.3 at high Galactic latitudes and -0.7 around the Galactic plane, and attributed the higher spectral index to contamination from free-free emission, AME and thermal dust. The Planck mission also confirmed the detection of the Haze and measured a spectral index of -0.56±0.05 for the intensity (Planck Collaboration et al., 2013) and -0.54±0.16 for the polarisation of a filament located at the edge of the northern bubble (Planck Collaboration et al., 2016b).

Several mechanisms were proposed to explain the microwave Haze/Fermi bubbles emission:

1. The DM hypothesis states that the electron population responsible for the emission is produced by collisions of weakly interactive massive particles. It would be visible near the Galactic centre because the density of DM is higher than in the rest of the Galaxy and would imply that the emission of the Haze is almost proportional to the square of the DM profile.

2. Su et al. (2010) proposed an event of enhanced accretion onto the central black hole lasting $10^5 - 10^6$ years, which caused an AGN-like jet emission.

3. Cheng et al. (2011) proposed a model with periodic star capture processes from the central black hole driving hot plasma outflows.

4. Carretti et al. (2013) claims that the emission originate in a biconical star-formation-driven outflow from the gas located in a ring with diameters 100-200 pc around the Galactic centre. The details of this model can be found in Crocker et al. (2015).

At the moment of writing this thesis, the DM hypothesis is disfavoured since it does not explain the sharp edge of the Fermi bubbles (Su et al., 2010; Crocker et al., 2015) nor the polarisation at their border (Jones et al., 2012; Carretti et al., 2013). New polarisation data, especially in the low frequency regime, are fundamental to differentiate among the existing models.

5.6.2 Analysis of the Diffuse Emission

Choice of the regions

The analysis of the diffuse emission in the Haze has been done through a correlation technique. We have divided the Haze field in several regions in order to

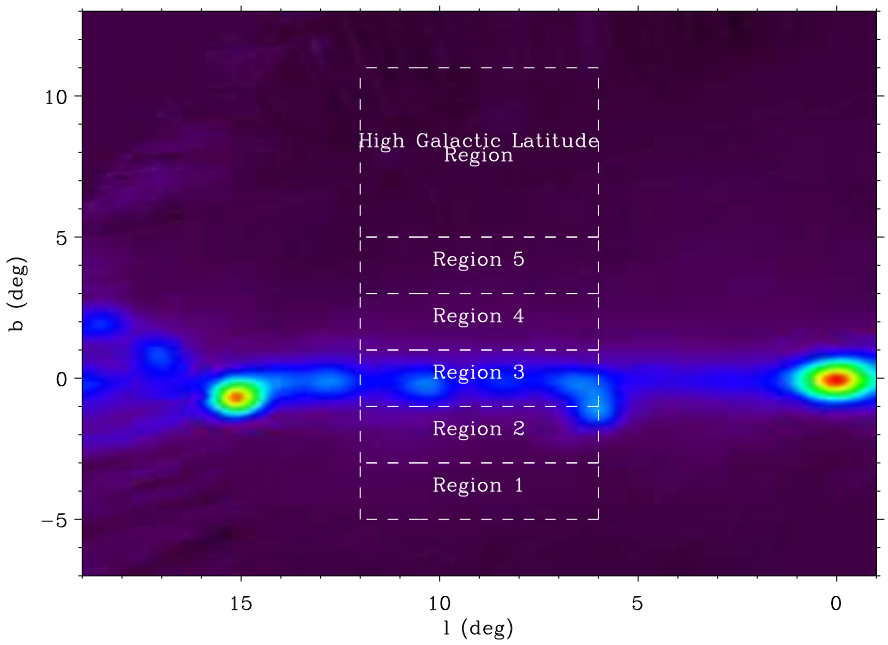

FIGURE 5.7— Intensity map of the Haze field (MFI, horn 3, 13 GHz) and regions chosen for the TT-plot analyses. Due to low S/N, all the regions above the fifth are combined in one High Galactic Latitude Region. In polarisation, we analysed two regions in order to improve the S/N: the Galactic plane region was obtained as the union of Regions 2, 3 and 4, while the High Galactic Latitude Region was merged with Region 5.

get a spectral index for each of them, assuming that it is constant in each case. The choice has been made to enhance an eventual dependence of the spectral index with the Galactic latitude, keeping the size of each region as small as possible but still guaranteeing enough S/N (which grows with the area) and a constant spectral index alongside the region. Finally, we opted for rectangles of 2° width in Galactic latitude, spanning from $b = -5^{\circ}$ to $b = 11^{\circ}$, and Galactic longitude from $l = 6^{\circ}$ to $l = 12^{\circ}$ (see Fig. 5.7). While this solution has proven to be adequate for intensity around the Galactic plane, high latitude regions have been combined in order to enhance the S/N. For polarisation only two regions have been considered: one from $b = -3^{\circ}$ to $b = 3^{\circ}$ and one from $b = 3^{\circ}$ to $b = 11^{\circ}$. The pixelisation used is $N_{\rm SIDE}$=128 (pixel size $\approx 0.5^{\circ}$) for intensity and $N_{\rm SIDE}$=64 for polarisation (pixel size $\approx 1^{\circ}$). This choice allows to have a sufficient number of points to correlate and, at the same time, it avoids the effect of the correlation between pixels induced by the smoothing of the maps.

The maps from Dwingeloo (0.82 GHz; Berkhuijsen 1972), Reich (1.42 GHz; Reich & Reich 1988) and Urumqi (4.8 GHz; Gao et al. 2011) are not used in the analysis since they do not cover the regions chosen for the analysis.

TT-plots

The Temperature vs Temperature plots (TT-plots hereafter) is a widely used technique (one of the first uses is in Turtle et al. 1962) to compute spectral indexes between pairs of frequencies in case of extended regions with low signal to noise ratios. The underlying assumption of this method (see Fuskeland et al. 2014; Turtle et al. 1962) is that we have a region of the sky observed at two different frequencies ν_1, ν_2 sufficiently small that the spectral index is spatially constant. In the case of synchrotron emission for example, the temperature[10] observed at the frequency ν_i at the pixel of coordinates (l, b) will be:

$$T(l, b; \nu_i) = T_0(l, b) \left(\frac{\nu_i}{\nu_0}\right)^{\beta} + n_i(l, b) \tag{5.21}$$

where we introduced the temperature $T_0(l, b)$ at a reference frequency ν_0, the spectral index[11] β, which is assumed to not depend on the position since the region is small, and the statistical noise of the map at the pixel, $n_i(l, b)$. If we consider again the case of two observed maps, and we take the ratio of Eq. (5.21) for $i = 1$ and $i = 2$ assuming the ideal case of zero noise, we will have:

$$\frac{T(l, b; \nu_2)}{T(l, b; \nu_1)} = \left(\frac{\nu_2}{\nu_1}\right)^{\beta} \Rightarrow \beta = \frac{\ln\left(T(l, b; \nu_1)/T(l, b; \nu_2)\right)}{\ln(\nu_1/\nu_2)} \tag{5.22}$$

Notably, the right side of the first equation in Eq. (5.22) does not depend on the location, thus there is a straight linear dependence of one data with respect to the other with slope $a = (\nu_1/\nu_2)^{\beta}$ and intercept $b = 0$:

$$T(l, b; \nu_2) = a \cdot T(l, b; \nu_1) + b \tag{5.23}$$

Different βs inside the considered region and the noise $n_i(l, b)$ are responsible for the scatter in the data, but Eq. (5.23) still holds statistically. Hence, we can retrieve the parameters a, b (and then the spectral index) with a linear

[10] We use brightness temperature, which is converted from the antenna temperature through the factor $g(\nu) = (e^x - 1)^2/(x^2 e^x)$, with $x = h\nu/kT_{\rm CMB}$.

[11] Throughout this section β is the spectral index of the temperature spectrum, while in the previous chapters and sections it represented the flux density spectrum, which was obtained through aperture photometry. In the Raylight limit, the relationship between the two is: $\beta_{\rm Temp} = \beta_{\rm Flux} - 2$.

regression of the data, taking into account that the errors in the abscissae are not negligible. The fit was done with the IDL *fitexy.pro*[12] function. This procedure first normalises the data to their standard deviation, stddev(x):

$$x' = \frac{(x - \mathrm{avg}(x))}{\mathrm{stddev}(x)} \qquad \sigma'_x = \frac{\sigma_x}{\mathrm{stddev}(x)}$$
$$y' = \frac{(y - \mathrm{avg}(y))}{\mathrm{stddev}(y)} \qquad \sigma'_y = \frac{\sigma_y}{\mathrm{stddev}(y)} \quad (5.24)$$

where σ_x is the error associated to each data point x. Then, the fit is obtained through the procedure described in Press et al. (1992).

In polarisation, Fuskeland et al. (2014) claim that the same procedure can be applied to Q and U separately, which is not true in case of Faraday rotation or any other mechanism that causes a rotation of the polarisation angle, such as a mixture of polarised components with different polarisation angles or different spectra. However, it can be applied to the polarised intensity after having debiased the data with the procedure described in subsection 5.2.3. This is the approach that we used in this work.

The main advantage of the correlation technique is that it is insensitive to the errors in the determination of the zero levels of the maps, since any eventual offsets would be absorbed in the parameter b without affecting the spectral index determination. In the case of aperture photometry of compact sources, instead, we relied on the background subtraction to remove eventual offsets that affect the whole map, given that the size of the source is small and the background can be considered almost constant at the scales of interest. However, this is not the case for diffuse emission. In particular, the QUIJOTE maps are insensitive to scales larger than the map size (20-30$^{\mathrm{o}}$). Also, Platania et al. (2003) claims that the Haslam map at 0.408 GHz has an error of its zero level of the order of 3 K, which has to be taken into account when using other methods.

Another advantage of the correlation technique is that it allows to easily identify eventual outliers: in this work, we first fit all the points in order to get a tentative β, then we remove all points that lie at more than 3 σs from the fitted model, and we finally repeat the whole process to obtain the final β.

5.6.3 Intensity Correlation Plots of the Extended Regions

The intensity correlation plots between each pair of frequencies have been calculated for each one of the chosen regions (see above). As an example we show

[12] See *http://www.harrisgeospatial.com/docs/fitexy.html* for detailed documentation.

the TT-plots pivoting around 0.408 GHz in Fig. 5.8 for the Galactic plane region. The spectral index is very stable with an average value for all frequencies of -2.18 ± 0.01, which is representative of free-free emission, however the last panel (0.408 vs 92.99 GHz) shows a flatter index of -2.11 ± 0.02, which may be caused by the presence of the thermal dust component.

For the same region, the plots pivoting around 11 GHz are shown in Fig. 5.9. The average spectral index[13] is a bit flatter ($\beta_{\rm avg} = -2.08 \pm 0.01$) since the synchrotron contribution is lower than in the case of correlating with the 0.4 GHz map, and we still note the impact of the thermal dust at 93 GHz. More interestingly, we note that the βs at frequencies between 23 GHz and 32 GHz are flatter. This is a clear evidence of AME in the region, since it shows up as a bump in the data around those frequencies, which causes the indexes calculated between these and lower frequencies to be flatter than in absence of AME. The spectral index between 13 GHz and 11 GHz is clearly an outlier, although the maps do not present outstanding features as to justify this. Probably, this effect is due to a contribution from the 1/f noise. In fact the two set of data pass through the same low-noise amplifier, which is the main responsible for this kind of systematics. One method to verify this is to check the polarisation data from the same horns: since they are much less affected by the 1/f noise (the knee-frequency in the 1/f is much lower for polarisation data) their correlation plot should not be affected, as we will see in the first panels of Figs. 5.11 and 5.12. The correlation plot between 19 GHz and 11 GHz seems reasonable, although we know (see chapter 4) that we do not have completely reliable maps of the Haze region at 19 GHz.

For the other regions, especially at $b > 5^{\rm o}$, the scatter of the points is a bit larger, especially for QUIJOTE data and in some extreme cases the correlation plots do not give any correlation. Thus, as mentioned at the beginning of this section, we considered a larger region in order to enhance the S/N. Fig. 5.10 shows the summary of the spectral indexes calculated vs 0.408 GHz and vs 11 GHz. The contribution from thermal dust becomes more evident at frequencies higher than 90 GHz. Also, we note a dependence with Galactic latitude: the further the region is from the Galactic plane, the steeper the spectrum is. This means that the synchrotron component is larger at higher Galactic latitudes than the free-free component. Since cosmological observations usually are centred in regions far from the Galactic plane to reduce the Galactic contamination, the characterisation of the synchrotron is much more important than

[13] In this average we avoided the spectral index between 11 and 13 GHz, which is an outlier (see below) and the spectral indexes above 80 GHz since they are affected by the contribution of the thermal dust.

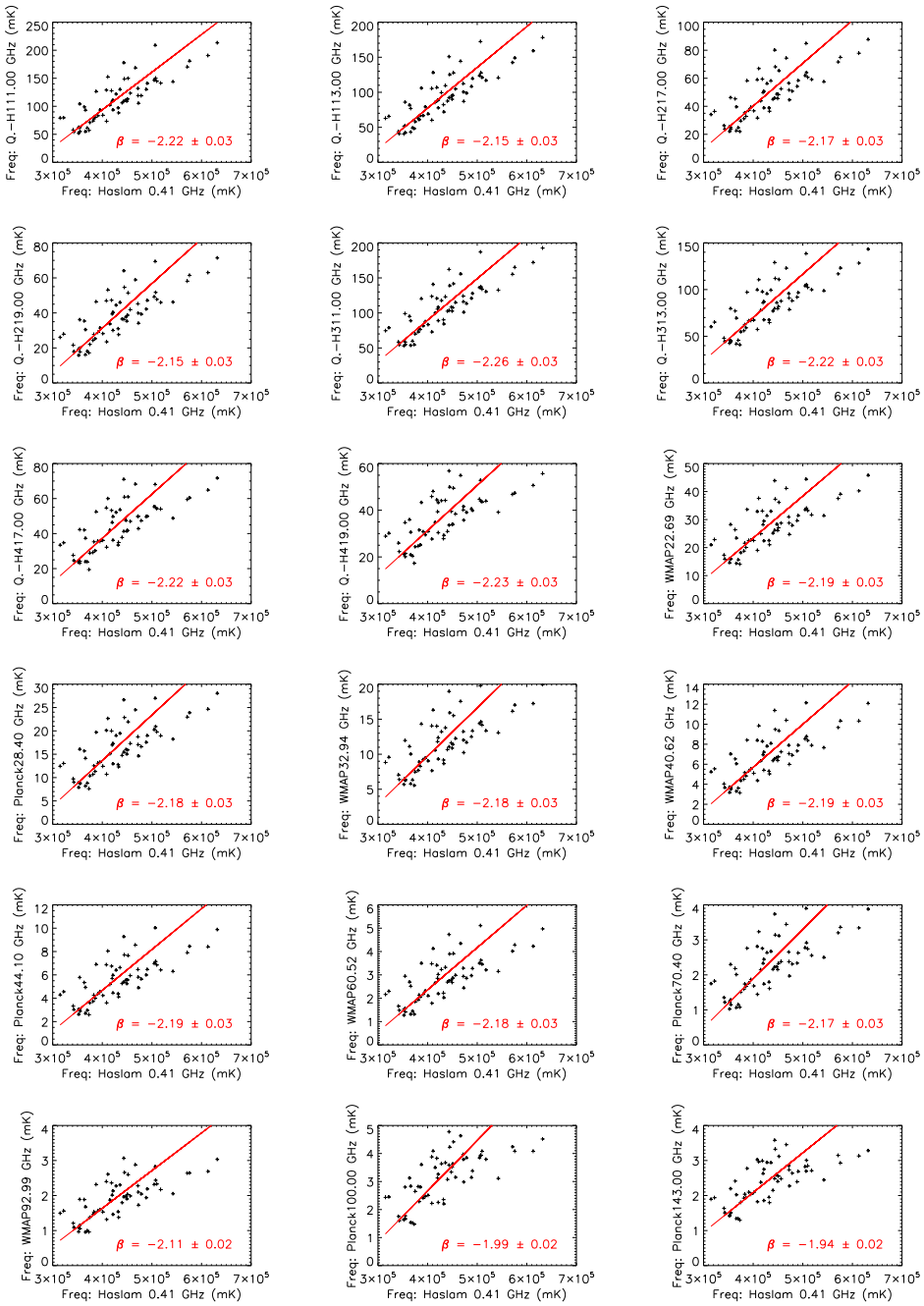

FIGURE 5.8— TT-plots of the Galactic plane "stripe" ($-1^{\circ} < b < 1^{\circ}$). Each plot shows the data of a given frequency vs the common pivot frequency 0.408 GHz from the Haslam map. All spectral indexes are compatible with free-free emission, which is the dominant emission mechanism for this region. The flattening of the spectral index in the last line is due to the impact of the thermal dust component.

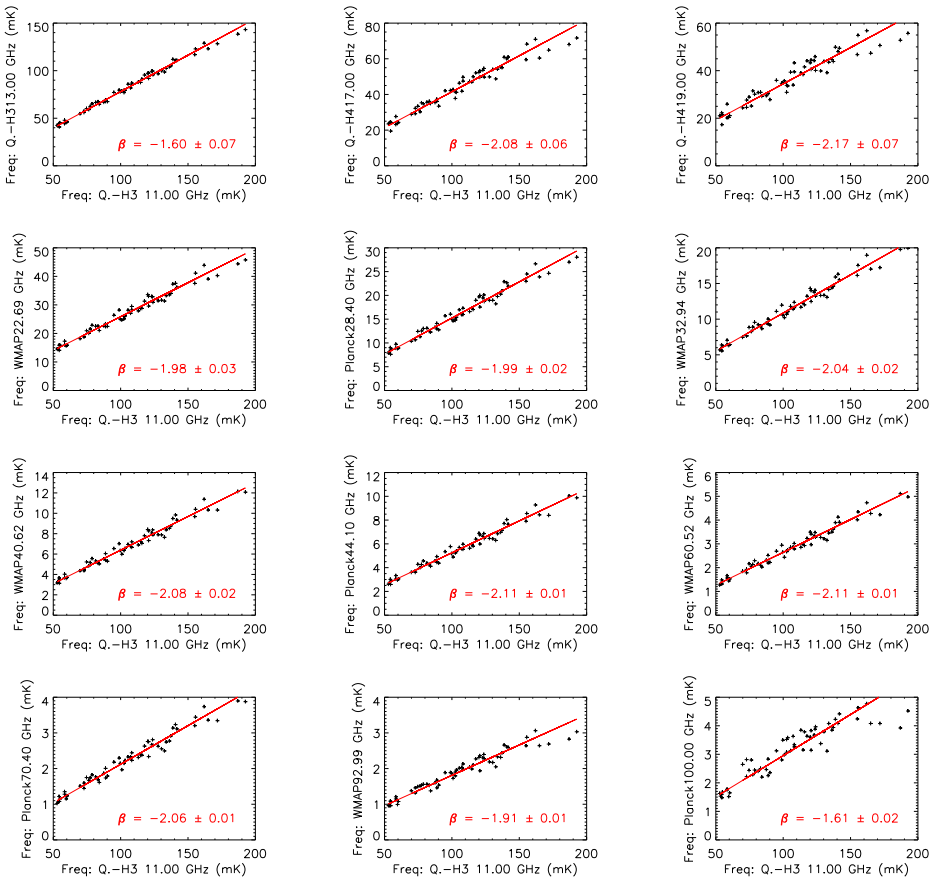

FIGURE 5.9— TT-plots of the Galactic plane "stripe" ($-1^{\circ} < b < 1^{\circ}$). Each plot shows the data of a given frequency vs the common pivot frequency 11 GHz from the MFI, horn 3. The flattening of the spectral index from the WMAP 23 GHz to the WMAP 33 GHz is an indication of AME. In all cases, the indexes obtained correlating with 11 GHz are flatter (≈ -2) than the indexes calculated with respect to 0.408 GHz. This is because the 11 GHz map traces free-free emission better than synchrotron emission. Also, in some cases the indexes could be flatter due to a possible contribution of AME. The last plot reveals, again, the contribution by thermal dust.

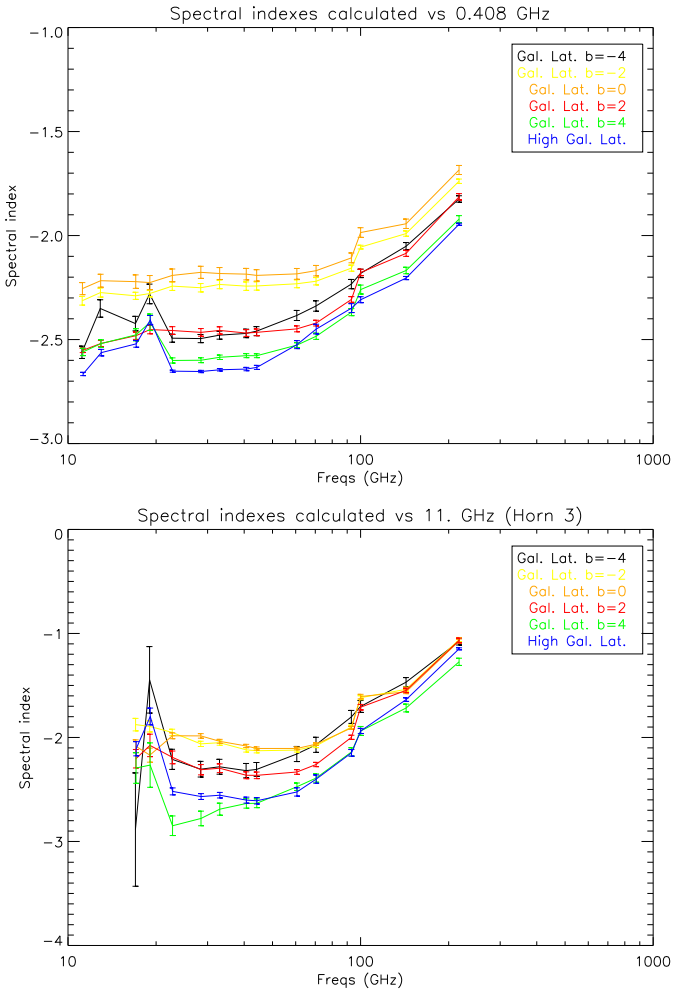

FIGURE 5.10— Spectral indexes for the stripes at constant Galactic latitude. The blue line represents the High Galactic altitude region used to increase the S/N. The frequency range covers up to 150 GHz in order to show the rising of the spectral index due to thermal dust, and confirm the results at 90 GHz from the previous plot. Top panel: each index is calculated between the frequency represented in the x-axis vs the Haslam map at 0.408 GHz. Bottom panel: each index is calculated between the frequency of the x-axis vs the QUIJOTE map at 11 GHz from MFI Horn 3. The point at 13 GHz is not shown since it is affected by the correlation of the noise in the map (the data at 11 GHz and 13 GHz pass through the same amplifier). A clear dependence with latitude is visible: the Galactic plane present free-free emission spectral indexes, while the synchrotron dominates at higher Galactic latitudes.

the free-free characterisation, at least for cosmological purposes.

5.6.4 Polarisation Correlation Plots of the Extended Regions

The polarisation correlation plots have been computed for two large regions at a smaller $N_{\rm SIDE}$ than the intensity analysis. The frequencies used ranged from 11 GHz to 93 GHz, since the low-frequency surveys do not provide information on the polarisation, while data at frequencies higher than 93 GHz are characterised by thermal dust polarisation.

Fig. 5.11 shows the correlation plots in polarised intensity for the Galactic plane region, while Fig. 5.12 shows the results for the high Galactic latitude region (see Fig. 5.7 for the definition of these regions). Although we increased the S/N thanks to the lower resolution, we still have a big scatter in both regions. The summary of the polarised intensity analysis is shown in Table 5.11. The correlation plot in intensity between 11 GHz and 13 GHz was not reliable due to the 1/f noise from the common amplifier (see above). This is not the case for polarisation, and the resulting spectral index are reasonable ($\beta_{\rm Disk} = -2.1 \pm 0.2$, $\beta_{\rm High} = -2.2 \pm 0.5$). Again, the 19 GHz maps are not completely reliable (see chapter 4), and in the high Galactic region there is no correlation between the 11 and 19 GHz maps (the plot has been removed from Fig. 5.12). If we do not take into account the index between 11 and 19 GHz, the average spectral index up to 61 GHz is $\beta_{\rm Disk,\ avg} = -2.56 \pm 0.04$ at low Galactic latitudes and $\beta_{\rm High,\ avg} = -2.62 \pm 0.07$ at high Galactic latitudes, which are both indicative of synchrotron emission and agree remarkably well with the spectral index presented in the Planck papers (Planck Collaboration et al. 2013 for intensity and Planck Collaboration et al. 2016b for polarisation). However, the indexes are steeper at frequencies between 30 and 60 GHz. This can be caused by polarised AME, which would enhance the polarised signal between 10 and 30 GHz, or by a curvature of the synchrotron spectrum after 30 GHz, or by systematic effects in some of the maps.

5.6.5 Estimation of the Polarisation Fraction of the Synchrotron and Diffuse AME

From the spectral indexes obtained above we can infer some parameters of the diffuse emission in the Haze, such as the ratio between synchrotron and free-free emission, the polarisation fraction of the synchrotron or a try to derive map of the contribution of the AME.

The idea is the following: let us suppose that the emission at frequencies below 12 GHz is given by the sum of two components: the synchrotron ($T_{11}^{\rm sync}$)

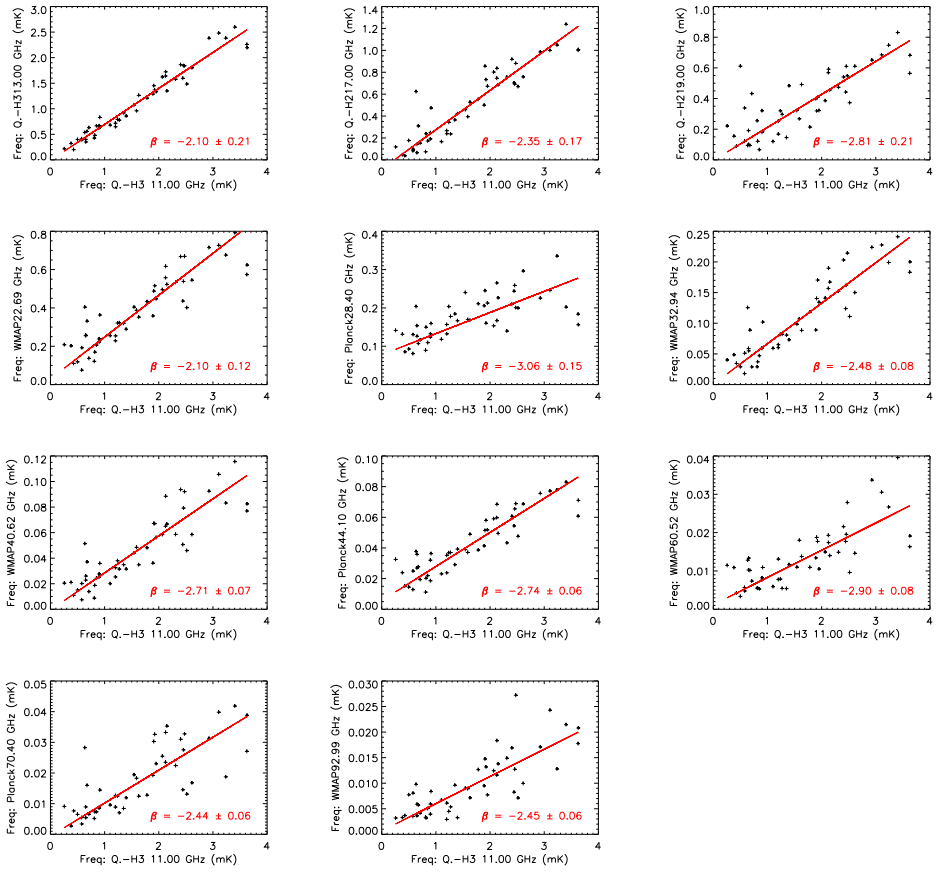

FIGURE 5.11— Polarised intensity correlation plots of the Galactic plane ($-3^{\circ} < b < 3^{\circ}$). Each plot shows the data of a frequency vs the common pivot frequency 11 GHz from the MFI, Horn 3.

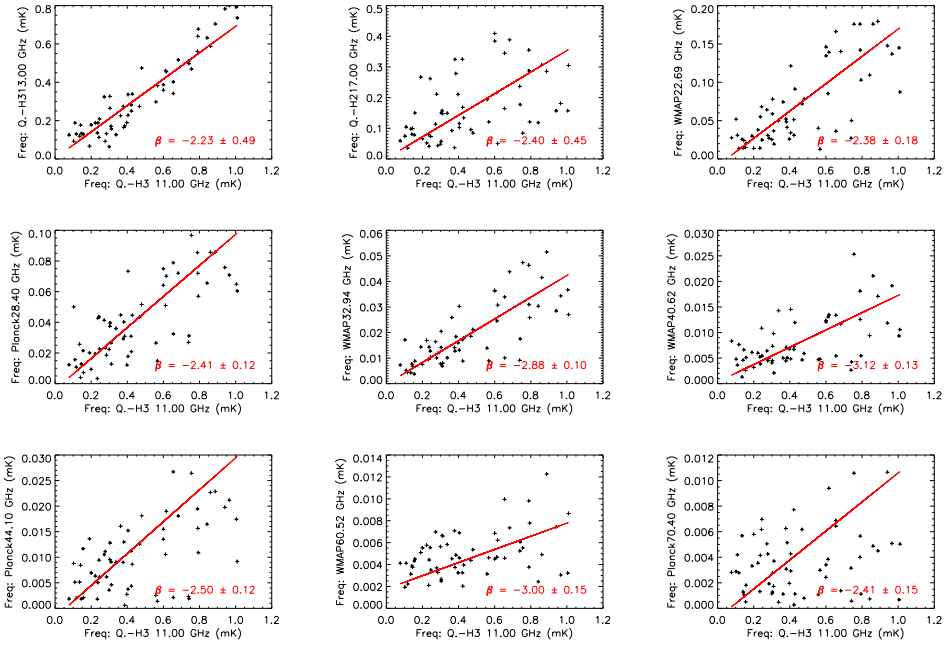

FIGURE 5.12— Polarised intensity correlation plots of the high Galactic latitude ($3^\circ < b < 11^\circ$). Each plot shows the data of a frequency vs the common pivot frequency 11 GHz from the MFI, Horn 3. The index of the correlation plot of 11 GHz versus 19 GHz is not determined, since the map is strongly affected by spurious signal that is dominating over the astrophysical signal (see chapter 4), and the corresponding plot is not shown. We also omitted the plot of the correlation between 11 and 93 GHz.

Freqs (GHz)	$\beta_{\rm pol}$ Gal. plane	$\beta_{\rm pol}$ High Gal. Lat.
12.89	-2.10 ± 0.21	-2.23 ± 0.49
16.75	-2.35 ± 0.17	-2.40 ± 0.45
22.69	-2.10 ± 0.12	-2.38 ± 0.18
28.40	-3.06 ± 0.15	-2.41 ± 0.12
32.94	-2.48 ± 0.08	-2.88 ± 0.10
40.62	-2.71 ± 0.07	-3.12 ± 0.13
44.10	-2.74 ± 0.06	-2.50 ± 0.12
60.52	-2.90 ± 0.08	-3.00 ± 0.15
70.40	-2.44 ± 0.06	-2.41 ± 0.15
92.99	-2.45 ± 0.06	-3.45 ± 0.89

TABLE 5.11— Summary of the spectral indexes measured in polarisation pivoting around the 11 GHz of MFI Horn 3. In order to improve the S/N, a pixelisation at $N_{\rm SIDE}$=64 ($\approx 1^{\rm o}$ pixel size) is used. For the same reason only two large regions are used, one covering the Galactic plane from $b = -3^{\rm o}$ to $b = 3^{\rm o}$ and one at higher Galactic latitude (from $b = 3^{\rm o}$ to $b = 11^{\rm o}$). The point at 19 GHz is not reliable for the reason explained in section 4.3. See text for details.

and the free-free, ($T_{11}^{\rm ff}$). Then, the fraction of synchrotron at 11 GHz is:

$$f_{11}^{\rm sync} = \frac{T_{11}^{\rm sync}}{T_{11}} = \frac{T_{11}^{\rm sync}}{T_{11}^{\rm sync} + T_{11}^{\rm ff}} \tag{5.25}$$

The intensity correlation plots gave us the spectral index in intensity $\beta_{\rm int}$ between 0.4 GHz and 11 GHz, which is a combination of the synchrotron spectral index $\beta_{\rm sync}$ and the free-free spectral index $\beta_{\rm ff} = -2.15$. Since the free-free emission is unpolarised, we can use the correlation plots in polarisation to estimate the spectral index of the synchrotron, assuming that it does not change with the frequency (we have not polarisation data at 0.4 GHz and they would be affected by Faraday depolarisation). Hence, the temperature at 0.4 GHz can be obtained with:

$$\begin{aligned} T_{0.4} = T_{11}\left(\frac{0.4}{11}\right)^{\beta_{\rm int}} &= T_{11}^{\rm sync}\left(\frac{0.4}{11}\right)^{\beta_{\rm sync}} + T_{11}^{\rm ff}\left(\frac{0.4}{11}\right)^{-2.15} = \\ &= T_{11}\left[f_{11}^{\rm sync}\left(\frac{0.4}{11}\right)^{\beta_{\rm sync}} + (1 - f_{11}^{\rm sync})\left(\frac{0.4}{11}\right)^{-2.15}\right] \end{aligned} \tag{5.26}$$

where we have introduced the fraction of the synchrotron with respect to the

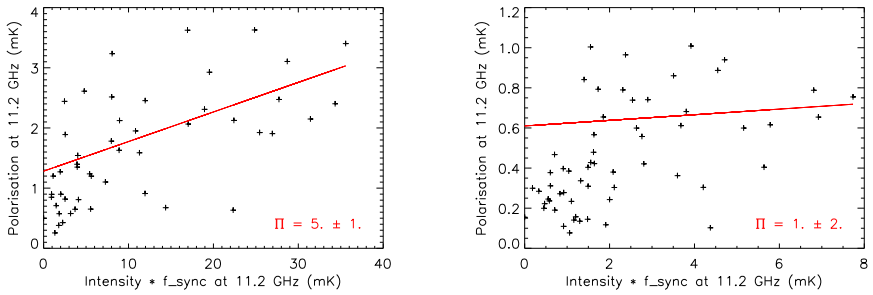

FIGURE 5.13— Polarisation data vs synchrotron intensity data for the Galactic plane region (left panel) and the High Galactic Latitude region (right panel). We retrieve a polarisation fraction of $5 \pm 1\%$ in the Galactic plane, but the fit is poor in the case of the High Galactic Latitude region.

total at 11 GHz, $f_{11}^{\rm sync}$. If we factorise the temperature at 11 GHz, we get:

$$f_{11}^{\rm sync} = \frac{\left(\frac{0.4}{11}\right)^{\beta_{\rm int}} - \left(\frac{0.4}{11}\right)^{-2.15}}{\left(\frac{0.4}{11}\right)^{\beta_{\rm sync}} - \left(\frac{0.4}{11}\right)^{-2.15}} \tag{5.27}$$

This gives a synchrotron fraction at 11 GHz of $22 \pm 11\%$ in the Galactic plane and $45 \pm 16\%$ in the High Galactic Latitude region[14].

The fraction of the synchrotron allows us a determination of its polarisation fraction $\Pi^{\rm sync}$. In fact, if all the polarised emission (P_{11}) is due to synchrotron mechanisms, we have:

$$P_{11} = P_{11}^{\rm sync} = \frac{\Pi^{\rm sync}}{100} T_{11}^{\rm sync} = \frac{\Pi^{\rm sync}}{100} f_{11}^{\rm sync} T_{11} \tag{5.28}$$

and a linear regression of P_{11} versus T_{11} will give the polarisation fraction, as shown in Fig. 5.13. We retrieve a polarisation fraction of $5 \pm 1\%$ in the Galactic plane, but the fit is poor in the case of the High Galactic Latitude region.

Finally, under the assumptions than we do not have AME contribution at 11 GHz, we can estimate the contribution of the AME at 23 GHz from the WMAP map at the same frequency. In fact, the temperature at 23 GHz, T_{23}, will be the sum of the AME contribution, $T_{23}^{\rm AME}$, the synchrotron contribution

[14] In both the regions, we used the spectral index between 11 GHz and 33 GHz in order to avoid Faraday depolarisation at low frequencies and eventual AME polarisation around 20 GHz.

and the free-free contribution, which can be extrapolated since we know the spectral indexes:

$$T_{23}^{\rm AME} = T_{23} - f_{11}^{\rm sync}\left(\frac{23}{11}\right)^{\beta_{\rm sync}} T_{11} - (1 - f_{11}^{\rm sync})\left(\frac{23}{11}\right)^{-2.15} T_{11} \qquad (5.29)$$

The map is shown in Fig. 5.14.

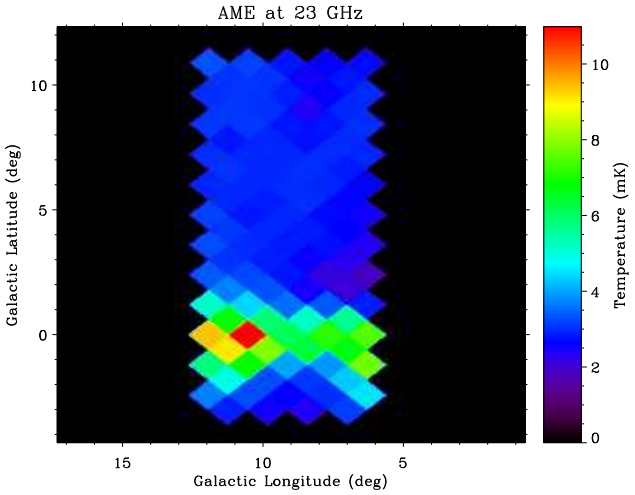

FIGURE 5.14— Map of the AME at 23 GHz obtained from the WMAP-9yr map and an extrapolation of the free-free and synchrotron emission at this frequency. See text for details.

5.7 General Discussion

Synchrotron Radiation

In intensity, the synchrotron emission has been found in four sources: the SNRs W44, W63 and W28, and the HII region LPH96-008.786-0.034. HII regions are not expected to emit synchrotron radiation, thus we suspect that this contribution is mainly coming from the background. The spectral indexes of these regions range between -0.32 in W44 and -0.43 in LPH96-008.786-0.034, which are flatter than the typical indexes expected in our Galaxy. This is due to contamination from free-free emission, which is characterised by a spectral index of ≈ -0.15 at frequencies higher than $\nu_0 \approx 1$ GHz. The regions W51 and W33, although containing SNRs, present indeed a spectral index typical of free-free emission, which is easily explained since they also contain giant molecular clouds rich in HII regions.

In polarisation, only three sources have been detected in the QUIJOTE maps: W44, W51 and W63. Their spectral indexes are -0.59±0.01, -0.60±0.01 and -0.62±0.01, respectively. This confirms the synchrotron radiation as the main polarised emission mechanism.

Free-Free Emission

The free-free emission was modelled in all the sources apart from the SNRs W44, W63 and W28. We estimated EMs of the order of $\approx 10^3$ pc· cm^{-6}, more specifically between 868 pc· cm^{-6} in W33 and 5324 pc· cm^{-6} in W43, which are very different than the typical values that can be found in literature ($\approx 10^6$ pc· cm^{-6}) but reasonable taking into account the dilution factor of the source in the beam ($\Omega_{\rm source}/\Omega_{\rm beam} \approx 10^3$ in most cases). We try to introduce this effect in 3 sources: M16, M17 and W31, using the undiluted EM'=EM·$\Omega_{\rm beam}/\Omega_{\rm source}$, which consequently changes the turn-over frequency accordingly to Eq. (5.14). In particular, M17 presents the strongest diluted EM, of the order of $25{\cdot}10^3$ pc· cm^{-6}. On the contrary, the source LPH96-008.786-0.034 is dominated by synchrotron emission but presents the lowest amplitude (EM=349 pc· cm^{-6}) of free-free emission.

We showed that the free-free emission is the dominant mechanism at the MFI frequencies, especially at 11 GHz, and that its distribution is concentrated on the Galactic plane. In fact, the 78% of the emission at $|b| < 3^{\rm o}$ is due to free-free (the synchrotron fraction is 78%), while at $b \sim 9^{\rm o}$ it is already only the 55%).

Anomalous Microwave Emission

AME has been detected in all the regions apart from W51 and M17. The frequency of the peak of this emission mechanism ranges between 16.6 and 31.9 GHz, with an average value of 24.3 GHz, which is compatible with values found in the literature (Planck Collaboration et al., 2014a). However, there is a small dependence with the Galactic longitude: the peak frequency of the regions in the Haze field is 27.5 GHz in average, while it is 19.5 GHz outside. This can suggest that part of this emission comes from the background and not from the analysed sources, since this corresponds to a scale of tenths of degrees, which is much larger than the objects that were considered. The maximum amplitude seems to follow this hypothesis since, excluding W43 ($A_{\rm peak}^{\rm AME} = 231 \pm 17$ Jy) and W63 ($A_{\rm peak}^{\rm AME} = 6 \pm 16$ Jy), its scatter is small (typical values around 50 or 60 Jy). The low value of the AME amplitude in W63 can also be explained in this context since it is the furthest region from the Galactic plane, at $b = 5.31^{\rm o}$.

Thermal Dust Emission

The emission from the thermal dust is found in all the regions and it is the dominant emission mechanism at frequencies higher than 90 GHz. Excluding the case of M8, the dust parameters are very stable: the temperature ranges between 19.17 K and 22.81 K with an average value of 20.5±1.2 K, while its spectral index is found to be between 1.70 and 1.89. We tried to relate the integrated flux of the dust model to the integrated flux of the AME, in order to find a linear relationship between them and to have an additional confirmation that the main AME component is actually the spinning dust. Unfortunately, the ratio $S^{\rm AME}_{\rm integral}/S^{\rm dust}_{\rm integral}$ had a scatter too large (standard deviation of $6.31 \cdot 10^{-5}$ against a median of $2.06{\cdot}10^{-6}$) to confirm this relationship, so no conclusion can be derived. A study with many more than 13 sources is needed to check this result.

Haze Diffuse Emission

The analysis presented in this work showed the spectral behaviour of some regions at constant Galactic latitude. We found that, in intensity, the spectral indexes are typical of free-free at low b and decrease at higher latitudes, presenting a major synchrotron component. In polarisation, we confirmed the same indexes that Planck measured in a filament at the edge of the Fermi bubble ($\beta \approx -2.54$ in temperature, see Planck Collaboration et al. 2016b). However, with QUIJOTE we cannot observe the same region since it is masked by the satellites band, nor can we observe the other border of the Fermi bubbles because of the location and elevation limits of the telescope. Moreover, in future a more refined component separation method will be needed to disentangle the free-free emission, the "normal" synchrotron emission and the harder Haze spectrum. For these reasons, we cannot advocate for neither exclude one of the proposed models to explain the Haze emission.

6

Conclusions

This thesis presents some of the technical and scientific results of the Multi-Frequency Instrument of the QUIJOTE-CMB Experiment during its first five years of observations. These are the results and scientific objectives that have been achieved in this work:

- A simple code for the MFI map-making was implemented. This has been used to make an overall characterisation of the MFI during the commissioning phase in terms of: noise levels, focal plane geometry, first estimation of the beams.

- The response of the gain calibrator (internal diode) was characterised. A code to compute its value avoiding transient effects was implemented.

- The optics of the MFI+QT1 was characterised in intensity through Cas A and geostationary satellites observations. For this purpose, a code to make maps of the MFI in local coordinates centred in the sources was implemented to correct the effect of Earth rotation. The main beams showed an optimal behaviour: the ellipticity is > 0.92 for all horns and frequencies and the beam efficiency is > 0.90.

- The near sidelobes were detected and mapped through observations of geostationary satellites. A map of the far sidelobes of the Sun in horn 1 was also made combining several observations in nominal mode. Both maps required an ad hoc recalibration and an ad hoc map-making method. These results agree with the simulations. The near sidelobes are found at a level of -40 dB in horns 1 and 3, and at the level of -25 dB in horns 2

and 4. The far sidelobes are detected in horn 1 to a level of -70 dB, which is unprecedented for a microwave experiment.

- A software to map the polarisation beam of horn 1 of the MFI through the use of the Müller matrices was implemented. This method used the new configuration of the MFI (implemented in April 2014 for the first horn and in December 2015 for the others) and can be used to characterise the other horns when enough data are accumulated. The intensity-to-polarisation leakage level for the horn 1 has been estimated below 1%.

- The window functions of each horn and frequency for the MFI+QT1 optics were computed. This can be used in future to correct the angular power spectrum of the foregrounds maps of the MFI, which will be necessary to correct the angular power spectrum of the CMB obtained with the TGI and FGI.

- The maps of four QUIJOTE Galactic fields (W44, W49, W63, Haze) were produced both in intensity and polarisation. Their final sensitivity is of the order of 500 μK/beam in intensity and 30-120 μK/beam in polarisation, which is consistent with the nominal sensitivities, given the integration time of each map. Then, the maps were smoothed to 1-degree resolution and the polarised intensity maps were debiased.

- The point sources (beam size $< 1^{\rm o}$) in each of these regions were analysed, their fluxes were calculated with the aperture photometry technique and their SEDs were modelled. AME evidence was found in all the sources apart from W51 and M17, and its peak frequency is found between 20 GHz and 30 GHz. At frequencies below 10 GHz, HII regions show a strong free-free spectrum, while SNRs are dominated by synchrotron emission. The spectral index is better characterised from polarisation data, and it is -0.6 for all the polarised sources. W31, W33 and LPH96-008.786-0.034 present both free-free and synchrotron emission. Dust properties (temperature and spectral index) are found to be almost independent of the source ($T \approx 20.5 \pm 1.2$ K, β between 1.70 and 1.89).

- The diffuse emission of the Haze region has been analysed through the correlation technique. In intensity, the average spectral index is -2.18 ± 0.01 on the Galactic plane, which is indicative of free-free emission. The indexes are flatter between 11 and 30 GHz in all cases, which is indicative of a diffuse AME component. In polarisation, the main emission mechanism is synchrotron, with a spectral index of -2.56 ± 0.04 at low Galactic latitudes and -2.62 ± 0.07 at $b > 3^{\rm o}$.

While the characterisation of the optics of the MFI in intensity can be considered finished, the characterisation in polarisation of the horns 2, 3 and 4 will need more data with the new configuration of the MFI. New data will also allow a better characterisation of the Haze emission, and a new observation strategy will be of fundamental importance to disentangle the different proposed emission mechanisms.

A

SEDs of Compact Sources in the Haze Field

This appendix contains all the tables and figures of the compact sources detected with the MFI in the Haze region (see section 5.6.1).

Survey	Freqs (GHz)	M8 (Jy)	M16 (Jy)	M17 (Jy)
Haslam	0.41	377± 82	108± 39	409± 71
Dwingeloo	0.82	—	—	—
Reich	1.42	—	44± 52	789± 88
HartRao	2.33	406± 56	135± 43	976± 74
Urumqi	4.80	—	140± 16	782± 18
QUIJOTE H1	11.23	340± 26	129± 18	752± 41
QUIJOTE H3	11.16	289± 23	100± 15	701± 39
QUIJOTE H1	12.84	335± 31	155± 19	794± 44
QUIJOTE H3	12.89	274± 23	71± 15	679± 38
QUIJOTE H2	16.75	295± 24	132± 17	704± 40
QUIJOTE H4	17.00	223± 19	103± 17	582± 34
QUIJOTE H2	18.71	297± 24	136± 18	712± 41
QUIJOTE H4	19.00	198± 18	-3± 19	553± 34
WMAP	22.69	277± 17	126± 14	634± 18
Planck	28.40	271± 16	129± 14	609± 18
WMAP	32.94	268± 15	129± 13	608± 17
WMAP	40.62	253± 14	124± 13	583± 15
Planck	44.10	247± 13	119± 12	575± 15
WMAP	60.52	235± 13	112± 12	564± 14
Planck	70.40	237± 14	101± 13	561± 15
WMAP	92.99	258± 20	106± 18	619± 22
Planck	100.00	274± 42	248± 36	803± 44
Planck	143.00	401± 57	369± 49	951± 62
Planck	217.00	1271± 306	1863± 268	3388± 330
Planck	353.00	4557± 1298	7635± 1167	13734± 1427
Planck	545.00	15205± 4924	27605± 4512	51938± 5380
Planck	857.00	55794± 17719	95455± 16526	190694± 19146
Dirbe	1249.14	161404± 42678	231893± 39791	468827± 45565
Dirbe	2141.37	378744± 69411	432419± 63408	898965± 73825
Dirbe	2997.92	290539± 34021	186385± 29052	632792± 35619
Dirbe	4996.54	182620± 10324	76248± 9644	427227± 10834

TABLE A.1— Intensity fluxes of M8, M16 and M17.

Survey	Freqs (GHz)	W28 (Jy)	W31 (Jy)	W33 (Jy)
Haslam	0.41	700± 90	325± 62	424± 68
Dwingeloo	0.82	—	—	—
Reich	1.42	—	184± 78	385± 74
HartRao	2.33	473± 45	261± 40	285± 43
Urumqi	4.80	—	308± 15	250± 23
QUIJOTE H1	11.23	274± 21	258± 18	263± 25
QUIJOTE H3	11.16	235± 18	232± 17	254± 25
QUIJOTE H1	12.84	316± 25	296± 21	286± 27
QUIJOTE H3	12.89	229± 18	244± 17	266± 26
QUIJOTE H2	16.75	247± 19	265± 19	288± 26
QUIJOTE H4	17.00	188± 15	224± 17	265± 24
QUIJOTE H2	18.71	260± 20	275± 19	301± 27
QUIJOTE H4	19.00	178± 15	219± 17	271± 24
WMAP	22.69	216± 13	250± 12	264± 21
Planck	28.40	217± 13	241± 12	258± 20
WMAP	32.94	205± 13	232± 11	244± 20
WMAP	40.62	194± 12	212± 10	228± 18
Planck	44.10	188± 12	203± 10	223± 18
WMAP	60.52	176± 11	198± 9	217± 18
Planck	70.40	184± 12	209± 10	231± 18
WMAP	92.99	242± 16	290± 15	335± 24
Planck	100.00	449± 34	538± 33	651± 43
Planck	143.00	627± 39	740± 44	893± 59
Planck	217.00	3375± 230	3748± 238	4700± 289
Planck	353.00	14467± 950	16017± 1027	20793± 1246
Planck	545.00	55137± 3620	61955± 3915	80400± 4717
Planck	857.00	198045± 13090	229877± 14042	286196± 16886
Dirbe	1249.14	483009± 31432	570395± 33498	676506± 40564
Dirbe	2141.37	815468± 50836	967322± 53799	1100590± 67875
Dirbe	2997.92	411595± 25210	511564± 25993	544125± 34997
Dirbe	4996.54	154004± 9163	180641± 7744	177403± 13361

TABLE A.2— Intensity fluxes of W28, W31 and W33).

Survey	Freqs (GHz)	LPH (Jy)
Haslam	0.41	587± 82
Dwingeloo	0.82	—
Reich	1.42	—
HartRao	2.33	338± 44
Urumqi	4.80	—
QUIJOTE H1	11.23	210± 21
QUIJOTE H3	11.16	190± 19
QUIJOTE H1	12.84	234± 24
QUIJOTE H3	12.89	193± 19
QUIJOTE H2	16.75	202± 21
QUIJOTE H4	17.00	174± 18
QUIJOTE H2	18.71	204± 21
QUIJOTE H4	19.00	169± 17
WMAP	22.69	177± 17
Planck	28.40	174± 16
WMAP	32.94	164± 15
WMAP	40.62	150± 14
Planck	44.10	144± 14
WMAP	60.52	139± 13
Planck	70.40	145± 14
WMAP	92.99	206± 20
Planck	100.00	431± 38
Planck	143.00	555± 52
Planck	217.00	3074± 267
Planck	353.00	13000± 1161
Planck	545.00	49364± 4463
Planck	857.00	174621± 16283
Dirbe	1249.14	420939± 39794
Dirbe	2141.37	679015± 67250
Dirbe	2997.92	332890± 35210
Dirbe	4996.54	109236± 12610

TABLE A.3— Intensity flux density of LPH96-008.786-0.034.

Parameter	M8	M16	M17
EM (pc·cm^{-6})	3664 ± 47	4327 ± 152	24805 ± 428
A^{ff}_{1GHz} (Jy)	336 ± 19	130 ± 7	717 ± 33
A^{sync}_{1GHz} (Jy)	—	—	—
β^{sync}	—	—	—
A^{AME}_{max} (Jy)	44 ± 5	32 ± 6	50 ± 0
ν^{AME}_{peak} (GHz)	28.69 ± 2.45	31.87 ± 4.20	30.00 ± 0.00
m_{60}	4.58 ± 3.26	3.88 ± 3.67	2.00 ± 0.00
T^{dust} (K)	27.26 ± 2.22	19.17 ± 1.09	22.81 ± 2.00
β^{dust}	1.48 ± 0.12	1.89 ± 0.12	1.70 ± 0.16
$\tau^{dust}_{250} \cdot 10^3$	0.40 ± 0.12	1.73 ± 0.43	1.97 ± 0.71
χ^2_{red}	0.61	1.13	6.68

TABLE A.4— Fit parameters for the intensity SED of M8, M16 and M17

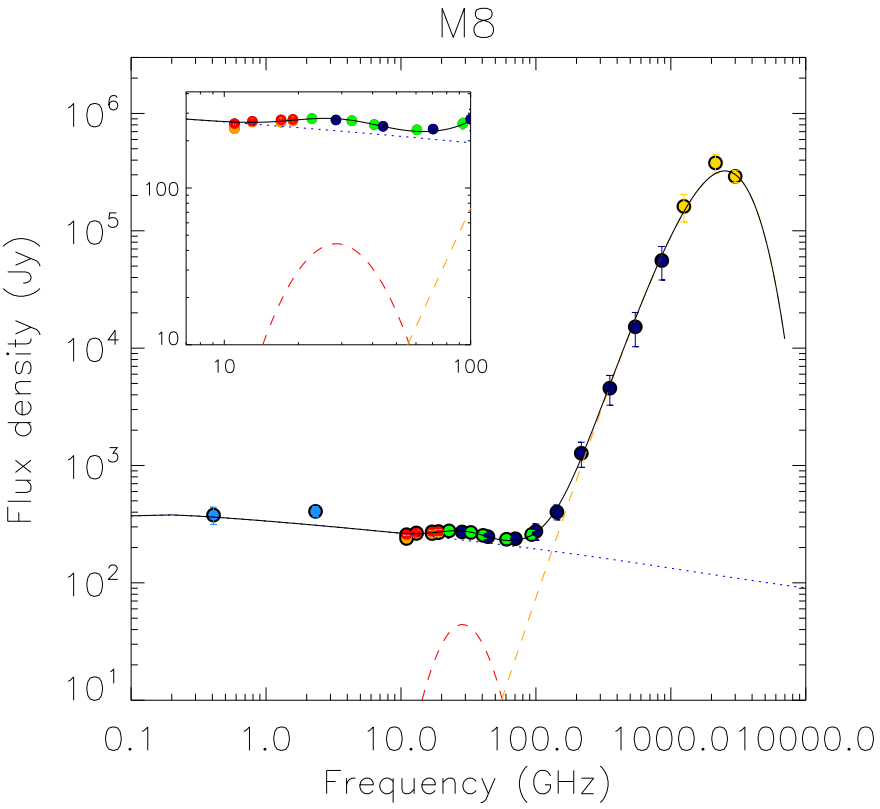

FIGURE A.1— Spectral Energy Distribution of M8 and fit to the principal components: free-free (light blue), synchrotron (blue), thermal dust (orange) and AME (red). QUIJOTE points are marked in orange and red to differentiate the two independent measurements at each frequency. The colors of the other points represent the different surveys: WMAP (green), Planck (blue), and DIRBE (yellow).

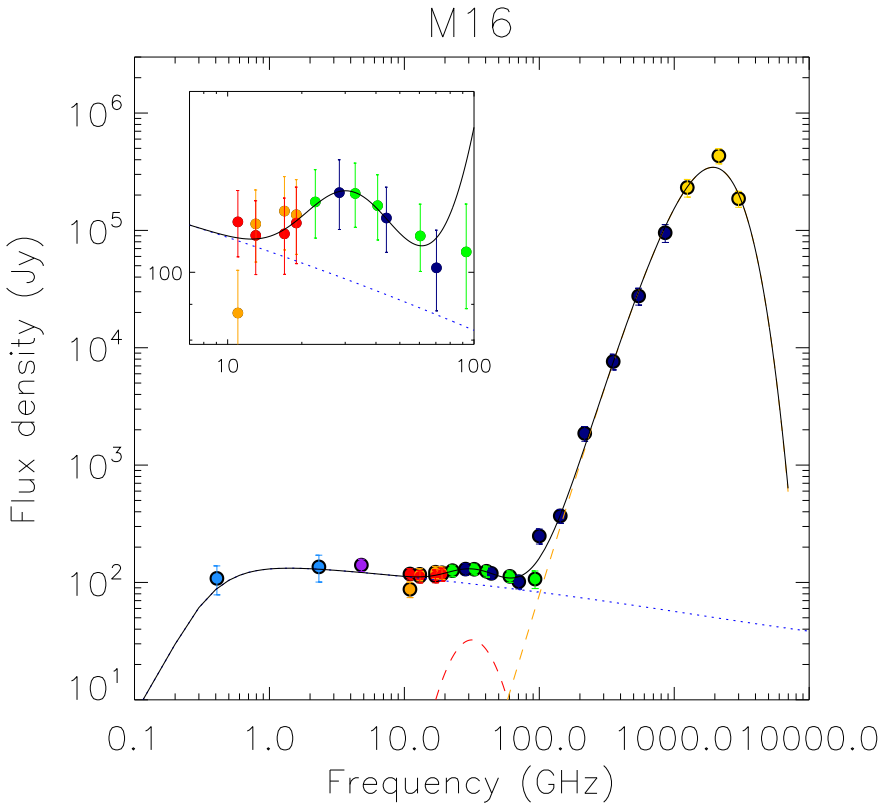

FIGURE A.2— Spectral Energy Distribution of M16 and fit to the principal components: free-free (light blue), synchrotron (blue), thermal dust (orange) and AME (red). QUIJOTE points are marked in orange and red to differentiate the two independent measurements at each frequency. The colors of the other points represent the different surveys: Urumqi (purple), WMAP (green), Planck (blue), and DIRBE (yellow). In this and two other sources (M17 and W31) we fix the turn-over frequency of the free-free to justify the low flux at 0.4 GHz.

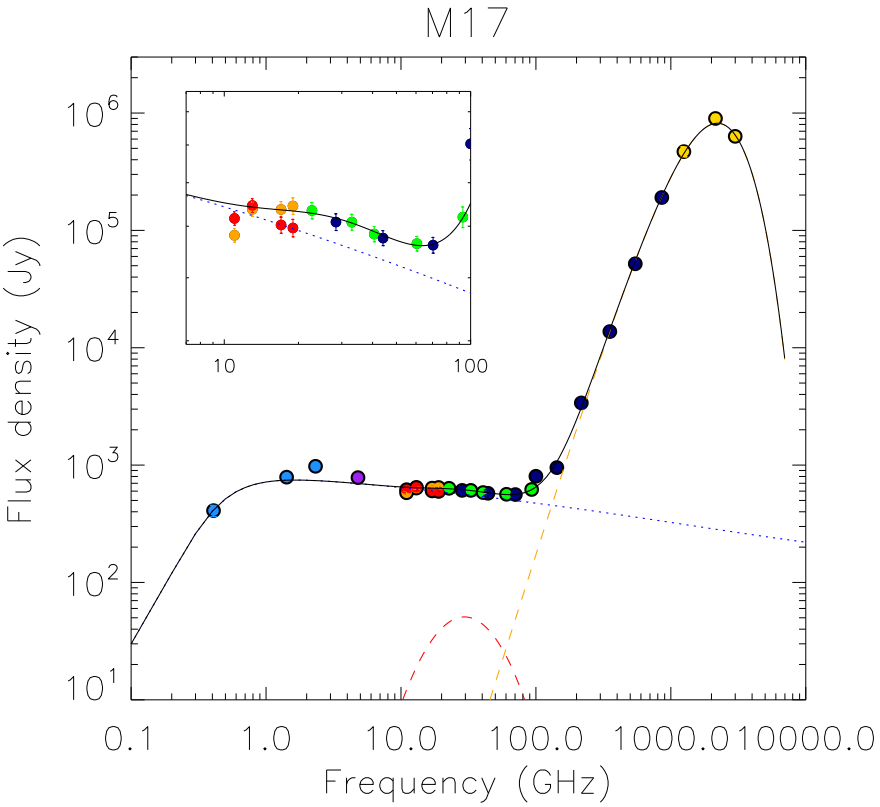

FIGURE A.3— Spectral Energy Distribution of M17 and fit to the principal components: free-free (light blue), synchrotron (blue), thermal dust (orange) and AME (red). QUIJOTE points are marked in orange and red to differentiate the two independent measurements at each frequency. The colors of the other points represent the different surveys: Urumqi (purple), WMAP (green), Planck (blue), and DIRBE (yellow). In this and two other sources (M16 and W31) we fix the turn-over frequency of the free-free to justify the low flux at 0.4 GHz.

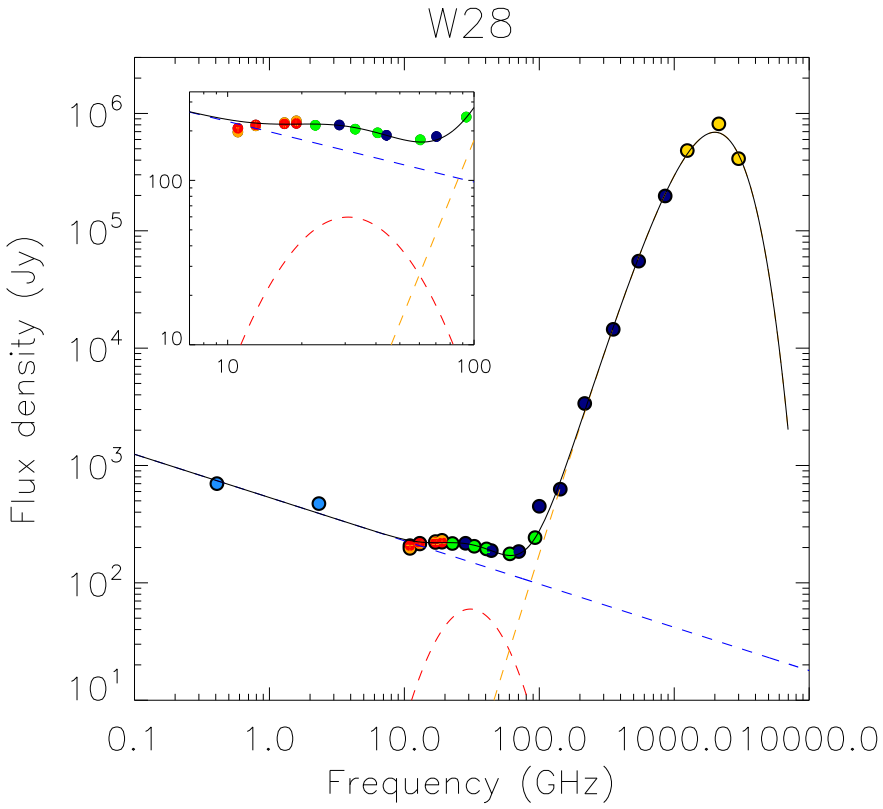

FIGURE A.4— Spectral Energy Distribution of W28 and fit to the principal components: free-free (light blue), synchrotron (blue), thermal dust (orange) and AME (red). QUIJOTE points are marked in orange and red to differentiate the two independent measurements at each frequency. The colors of the other points represent the different surveys: WMAP (green), Planck (blue), and DIRBE (yellow).

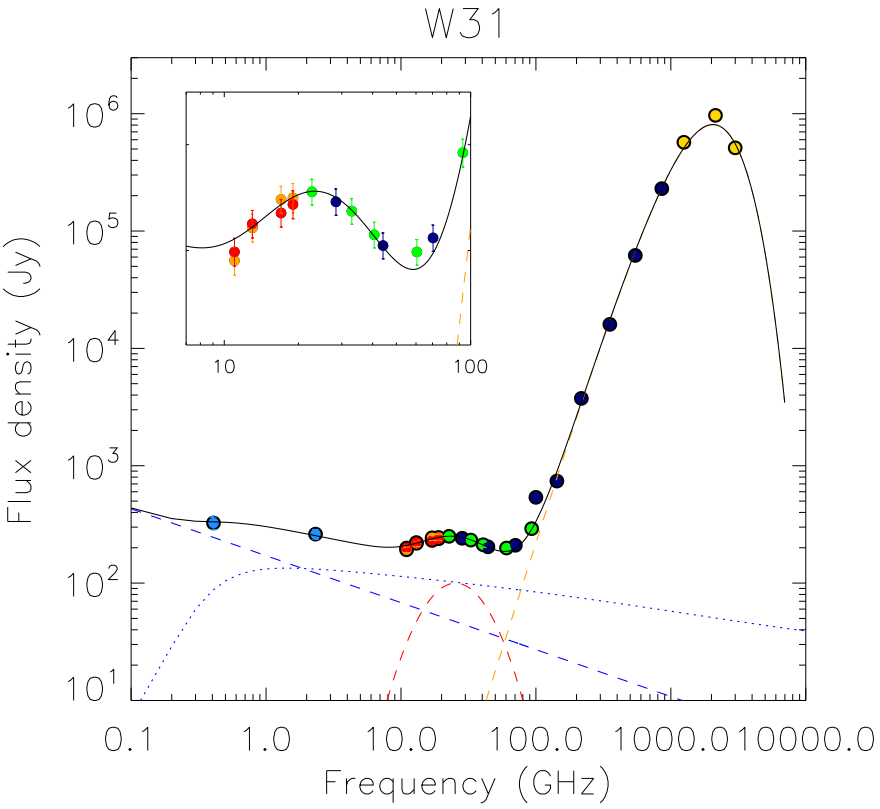

FIGURE A.5— Spectral Energy Distribution of W31 and fit to the principal components: free-free (light blue), synchrotron (blue), thermal dust (orange) and AME (red). QUIJOTE points are marked in orange and red to differentiate the two independent measurements at each frequency. The colors of the other points represent the different surveys: WMAP (green), Planck (blue), and DIRBE (yellow). In this and two other sources (M16 and M17) we fix the turn-over frequency of the free-free to justify the low flux at 0.4 GHz.

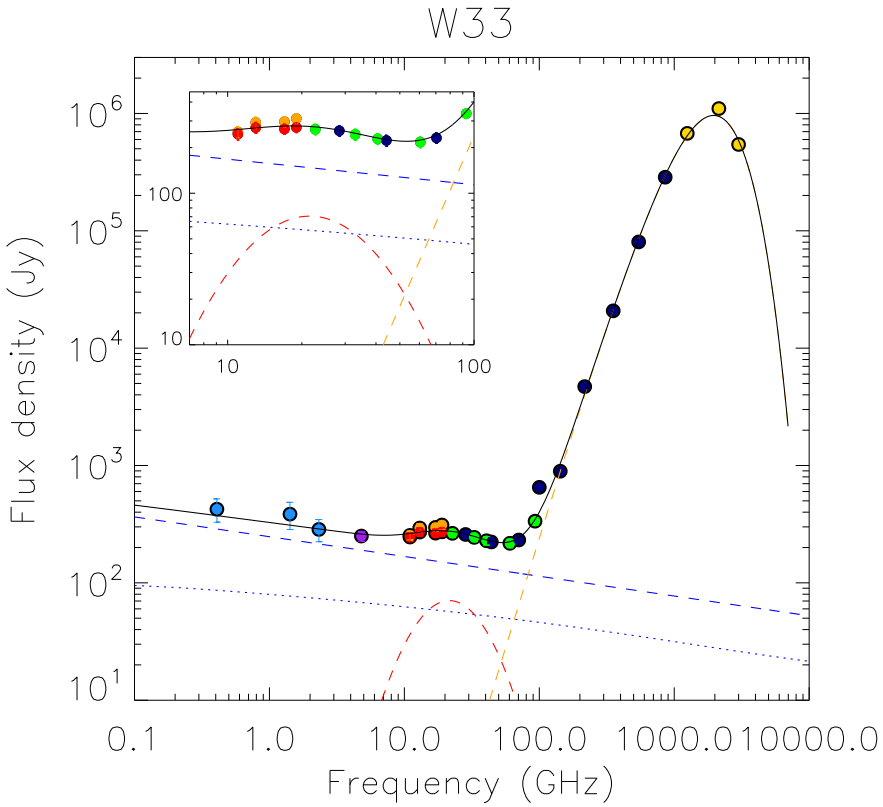

FIGURE A.6— Spectral Energy Distribution of W33 and fit to the principal components: free-free (light blue), synchrotron (blue), thermal dust (orange) and AME (red). QUIJOTE points are marked in orange and red to differentiate the two independent measurements at each frequency. The colors of the other points represent the different surveys: Urumqi (purple), WMAP (green), Planck (blue), and DIRBE (yellow).

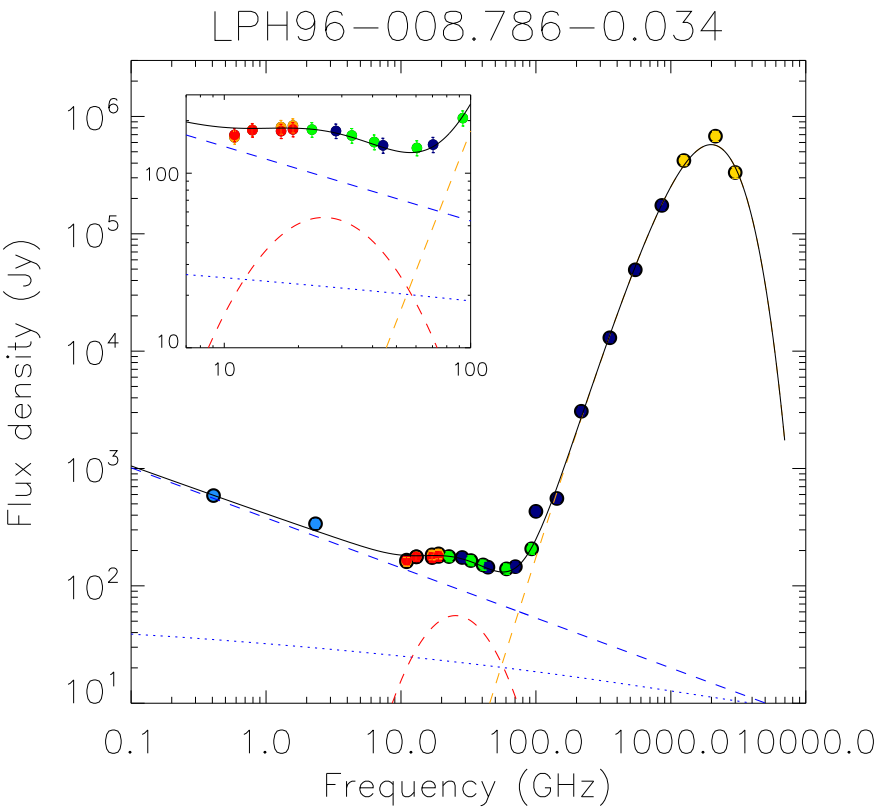

FIGURE A.7— Spectral Energy Distribution of LPH96-008.786-0.034 and fit to the principal components: free-free (light blue), synchrotron (blue), thermal dust (orange) and AME (red). QUIJOTE points are marked in orange and red to differentiate the two independent measurements at each frequency. The colors of the other points represent the different surveys: WMAP (green), Planck (blue), and DIRBE (yellow).

Parameter	W28	W31	W33
EM (pc·cm^{-6})	—	4398 ± 261	868 ± 137
A^{ff}_{1GHz} (Jy)	—	131 ± 10	79 ± 16
A^{sync}_{1GHz} (Jy)	533 ± 32	171 ± 32	247 ± 56
β^{sync}	-0.37 ± 0.03	-0.40 ± -0.00	-0.17 ± 0.08
A^{AME}_{max} (Jy)	59 ± 22	99 ± 14	70 ± 28
ν^{AME}_{peak} (GHz)	31.27 ± 4.64	25.66 ± 4.99	21.70 ± 2.71
m_{60}	2.28 ± 2.73	2.83 ± 2.52	2.97 ± 2.81
T^{dust} (K)	20.23 ± 1.03	21.08 ± 0.93	19.66 ± 0.83
β^{dust}	1.78 ± 0.10	1.71 ± 0.08	1.83 ± 0.09
$\tau^{dust}_{250} \cdot 10^3$	2.81 ± 0.60	2.81 ± 0.52	4.39 ± 0.78
χ^2_{red}	4.81	4.55	3.16

TABLE A.5— Fit parameters for the intensity SED of W28, W31 and W33

Parameter	LPH96 − 008.786 − 0.034
EM (pc·cm^{-6})	349 ± 93
A^{ff}_{1GHz} (Jy)	32 ± 11
A^{sync}_{1GHz} (Jy)	379 ± 29
β^{sync}	-0.43 ± 0.05
A^{AME}_{max} (Jy)	55 ± 22
ν^{AME}_{peak} (GHz)	25.65 ± 3.90
m_{60}	2.48 ± 2.36
T^{dust} (K)	20.44 ± 1.15
β^{dust}	1.71 ± 0.10
$\tau^{dust}_{250} \cdot 10^3$	2.31 ± 0.53
χ^2_{red}	2.57

TABLE A.6— Fit parameters for the intensity SED of LPH96-008.786-0.034

B

Acronyms and Abbreviations

AME	Anomalous Microwave Emission
ATM	Atmosphere (a code to calculate the atmospheric temperature at radio frequencies)
BEM	Back-End Module
BICEP	Background Imaging of Cosmic Extragalactic Polarization
BTOD	Binned Time Orederd Data
CMB	Cosmic Microwave Background
COBE	COsmic Background Explorer
COSMOSOMAS	COSMOlogical Structures On Medium Angular Scales
CST	Computer Simulation Technology
CTOD	Calibrated Time Ordered Data
DICOM	Departamento de Ingeniería de las COMunicaciones (University of Cantabria)
DIRBE	Diffuse InfraRed Background Explorer
DRAO	Dominion Radio Astrophysical Observatory
EM	Emission Measure
FEM	Front-End Module
FFT	Fast Fourier Transform
FGI	Forty GigaHeatz Instrument
FWHM	Full-Width Half Maximum
HartRAO	Hartebeesthoek Radio Astronomy Observatory
HBB	Hot Big Bang
HFI	High Frequency Instrument (PLANCK experiment)
HK	House Keeping
IAC	Instituto de Astrofísica de Canarias
JK	Jack-Knife

LFI	Low Frequency Instrument (PLANCK experiment)
LNA	Low Noise Amplifier
LoS	Line of Sight
MAE	Modified Asymptothic Estimator
MFI	Multi-Frequency Instrument
MMIC	Monolithic Microwave Integrated Circuit
NET	Noise-Equivalent Temperature
OMT	Ortho-Mode Transducer
PM	Pointing Model
PSF	Point Spread Function
PWV	Precipitable Water vapour
QT1	QUIJOTE Telescope 1
QT2	QUIJOTE Telescope 2
QUIET	Q/U Imaging ExperimenT
QUIJOTE	Q-U-I JOint TEnerife
RH	Relative Humidity
RM	Rotation Measure
RMS	Root Mean Square
S/N	Signal to Noise ratio
SED	Spectral Energy Distribution
SNR	SuperNova Remnant
TGI	Thirty GigaHeatz Instrument
TOD	Time Ordered Data
VSA	Very Small Array
WMAP	Wilkinson Microwave Anisotropy Probe
ΛCDM	Cosmological constant (Λ) with Cold Dark Matter

Bibliography

Albrecht, A., & Steinhardt, P. J. 1988, Cosmology for Grand Unified Theories with Radiatively-Induced Symmetry Breaking 497

Ali-Haïmoud, Y., Hirata, C. M., & Dickinson, C. 2009, MNRAS, 395, 1055

Bania, T. M., Anderson, L. D., & Balser, D. S. 2012, ApJ, 759, 96

Battistelli, E. S., et al. 2012, MNRAS, 423, 1293

Battistelli, E. S., Rebolo, R., Rubiño-Martín, J. A., Hildebrandt, S. R., Watson, R. A., Gutiérrez, C., & Hoyland, R. J. 2006, ApJL, 645, L141

Battye, R. A., Browne, I. W. A., Peel, M. W., Jackson, N. J., & Dickinson, C. 2011, MNRAS, 413, 132

Bennett, C. L., et al. 2013, ApJS, 208, 20

Berkhuijsen, E. M. 1972, A&AS, 5, 263

Bersanelli, M., et al. 2010, A&A, 520, A4

BICEP2 and Keck Array Collaborations, et al. 2015, ApJ, 806, 206

BICEP2 Collaboration, et al. 2014, Physical Review Letters, 112, 241101

BICEP2 Collaboration, et al. 2016, Physical Review Letters, 116, 031302

BICEP2/Keck Collaboration, et al. 2015, Physical Review Letters, 114, 101301

Bischoff, C., et al. 2013, ApJ, 768, 9

Blum, R. D., Damineli, A., & Conti, P. S. 1999, AJ, 117, 1392

Bonaldi, A., Ricciardi, S., Leach, S., Stivoli, F., Baccigalupi, C., & de Zotti, G. 2007, MNRAS, 382, 1791

Carretti, E., et al. 2013, Nature, 493, 66

Castro-Almazán, J. A., Muñoz-Tuñón, C., García-Lorenzo, B. n., Pérez-Jordán, G., Varela, A. M., & Romero, I. 2016, in , 99100P

Challinor, A. 2013, in IAU Symposium, Vol. 288, Astrophysics from Antarctica, ed. M. G. Burton, X. Cui, & N. F. H. Tothill, 42

Chandrasekhar, S. 1960, Radiative transfer (Dover Publications)

Cheng, K.-S., Chernyshov, D. O., Dogiel, V. A., Ko, C.-M., & Ip, W.-H. 2011, ApJL, 731, L17

Crocker, R. M., Bicknell, G. V., Taylor, A. M., & Carretti, E. 2015, ApJ, 808, 107

Dobler, G. 2012a, ApJ, 750, 17

Dobler, G. 2012b, ApJL, 760, L8

Draine, B. T. 2011, Physics of the Interstellar and Intergalactic Medium (Princeton University Press)

Draine, B. T., & Lazarian, A. 1999, ApJ, 512, 740

Durrer, R. 2008, The Cosmic Microwave Background (Cambridge University Press)

Finkbeiner, D. P. 2004a, ApJ, 614, 186

Finkbeiner, D. P. 2004b, in Bulletin of the American Astronomical Society, Vol. 36, American Astronomical Society Meeting Abstracts, 1478

Fixsen, D. J., Cheng, E. S., Gales, J. M., Mather, J. C., Shafer, R. A., & Wright, E. L. 1996, ApJ, 473, 576

Fuskeland, U., Wehus, I. K., Eriksen, H. K., & Næss, S. K. 2014, ApJ, 790, 104

Gamow, G. 1946, Physical Review, 70, 572

Gao, X. Y., Han, J. L., Reich, W., Reich, P., Sun, X. H., & Xiao, L. 2011, A&A, 529, A159

García-Lorenzo, B., Eff-Darwich, A., Castro-Almazán, J., Pinilla-Alonso, N., Muñoz-Tuñón, C., & Rodríguez-Espinosa, J. M. 2010, MNRAS, 405, 2683

Génova-Santos, R. 2013, QUIJOTE MFI Data Files Formats and Organization, Technical report, IAC

Génova-Santos, R. 2015a, QUIJOTE MFI Amplitude Calibration, Technical report, IAC

Génova-Santos, R. 2015b, QUIJOTE MFI Calibration Strategy, Technical report, IAC

Génova-Santos, R., & Hoyland, R. J. 2014, QUIJOTE MFI Bandpass Characterization, Technical report, IAC

Génova-Santos, R., et al. 2017, MNRAS, 464, 4107

Génova-Santos, R., et al. 2015a, in Highlights of Spanish Astrophysics VIII, ed. A. J. Cenarro, F. Figueras, C. Hernández-Monteagudo, J. Trujillo Bueno, & L. Valdivielso, 207

Génova-Santos, R., et al. 2015b, MNRAS, 452, 4169

Ginsburg, A. 2017, arXiv:1702.06627

Górski, K. M., Hivon, E., Banday, A. J., Wandelt, B. D., Hansen, F. K., Reinecke, M., & Bartelmann, M. 2005, ApJ, 622, 759

Guth, A. H. 1981, Phys. Rev. D, 23, 347

Hafez, Y. A., et al. 2008, MNRAS, 388, 1775

Han, J. L., Reich, W., Sun, X. H., Gao, X. Y., Xiao, L., Shi, W. B., Reich, P., & Wielebinski, R. 2013, in International Journal of Modern Physics Conference Series, Vol. 23, International Journal of Modern Physics Conference Series, 82

Harper, S. 2016, Ph.D. thesis, University of Manchester

Haslam, C. G. T., Klein, U., Salter, C. J., Stoffel, H., Wilson, W. E., Cleary, M. N., Cooke, D. J., & Thomasson, P. 1981, A&A, 100, 209

Haslam, C. G. T., Salter, C. J., Stoffel, H., & Wilson, W. E. 1982, A&AS, 47, 1

Ho, C., Slobin, S., Kantak, A., & Asmar, S. 2008, Interplanetary Network Progress Report, 175, 1

Hu, W., & White, M. 1997, New Astron., 2, 323

Hubble, E. 1929, Proceedings of the National Academy of Science, 15, 168

Irfan, M. O., et al. 2015, MNRAS, 448, 3572

Jonas, J. L., Baart, E. E., & Nicolson, G. D. 1998, MNRAS, 297, 977

Jones, D. I., Crocker, R. M., Reich, W., Ott, J., & Aharonian, F. A. 2012, ApJL, 747, L12

Kamionkowski, M., Kosowsky, A., & Stebbins, A. 1997, Phys. Rev. D, 55, 7368

Keihänen, E., Keskitalo, R., Kurki-Suonio, H., Poutanen, T., & Sirviö, A.-S. 2010, A&A, 510, A57

Keihänen, E., Kurki-Suonio, H., Poutanen, T., Maino, D., & Burigana, C. 2004, A&A, 428, 287

Keller, C. U., & Krucker, S. 2004, in Astrophysics and Space Science Library, Vol. 314, Astrophysics and Space Science Library, ed. D. E. Gary & C. U. Keller

Koch, P. M., Tang, Y.-W., Ho, P. T. P., Yen, H.-W., Su, Y.-N., & Takakuwa, S. 2018, The Astrophysical Journal, 855, 39

Kovalevsky, J. 2002, Modern Astrometry (Springer)

Krachmalnicoff, N., Baccigalupi, C., Aumont, J., Bersanelli, M., & Mennella, A. 2016, A&A, 588, A65

Kraus, J. D. 1966, Radio astronomy (McGraw-Hill)

Kurki-Suonio, H., Keihänen, E., Keskitalo, R., Poutanen, T., Sirviö, A.-S., Maino, D., & Burigana, C. 2009, A&A, 506, 1511

Lamarre, J.-M., et al. 2010, A&A, 520, A9

Leitch, E. M., et al. 2002, Nature, 420, 763

Linde, A. D. 1982, Physics Letters B, 108, 389

Ling, H., Chou, R.-C., & Lee, S.-W., 37

Lo, G., & Lonc, W. P. 1986, American Journal of Physics, 54, 843

López-Caraballo, C. H. 2013, Ph.D. thesis, Instituto de Astrofsica de Canarias, Univerisdad de La Laguna

López-Caraballo, C. H., Rubiño-Martín, J. A., Rebolo, R., & Génova-Santos, R. 2011, ApJ, 729, 25

Lyth, D. H. 1997, Physical Review Letters, 78, 1861

Mather, J. C., et al. 1990, ApJL, 354, L37

Mezger, P. G., Schraml, J., & Terzian, Y. 1967, AJ, 72, 817

Monsalve, R. 2012, Ph.D. thesis, University of Miami

Monsalve, R. A. 2010, in Proc. SPIE, Vol. 7741, Millimeter, Submillimeter, and Far-Infrared Detectors and Instrumentation for Astronomy V, 77412M

Nguyen Luong, Q., et al. 2011, A&A, 529, A41

O'Dea, D., Challinor, A., & Johnson, B. R. 2007, MNRAS, 376, 1767

Page, L. 2000, astro-ph/0012214

Page, L., et al. 2003, ApJS, 148, 39

Paladini, R., Burigana, C., Davies, R. D., Maino, D., Bersanelli, M., Cappellini, B., Platania, P., & Smoot, G. 2003, A&A, 397, 213

Peláez-Santos, A. E. 2013, Master's thesis, Instituto de Astrofsica de Canarias, Univerisdad de La Laguna

Penzias, A. A., & Wilson, R. W. 1965, ApJ, 142, 419

Pérez-de-Taoro, M. R., et al. 2014, in Proc. SPIE, Vol. 9145, Ground-based and Airborne Telescopes V, 91454T

Planck Collaboration, et al. 2016a, A&A, 594, A10

Planck Collaboration, et al. 2016b, A&A, 594, A25

Planck Collaboration, et al. 2014a, A&A, 565, A103

Planck Collaboration, et al. 2013, A&A, 554, A139

Planck Collaboration, et al. 2016c, A&A, 594, A13

Planck Collaboration, et al. 2015, A&A, 576, A107

Planck Collaboration, et al. 2014b, A&A, 571, A4

Plaszczynski, S., Montier, L., Levrier, F., & Tristram, M. 2014, MNRAS, 439, 4048

Platania, P., Burigana, C., Maino, D., Caserini, E., Bersanelli, M., Cappellini, B., & Mennella, A. 2003, A&A, 410, 847

Press, W. H., Teukolsky, S. A., Vetterling, W. T., & Flannery, B. P. 1992, Numerical Recipes in C (2Nd Ed.): The Art of Scientific Computing (Cambridge University Press)

Reich, P., & Reich, W. 1988, A&AS, 74, 7

Reich, W. 1982, A&AS, 48, 219

Remazeilles, M., Dickinson, C., Banday, A. J., Bigot-Sazy, M.-A., & Ghosh, T. 2015, MNRAS, 451, 4311

Rho, J., & Petre, R. 1998, ApJL, 503, L167

Rohlfs, K., & Wilson, T. L. 1996, Tools of Radio Astronomy (Springer-Verlag)

Rubiño-Martin, J. A. 2002, Ph.D. thesis, Instituto de Astrofsica de Canarias, Univerisdad de La Laguna

Rubiño-Martín, J. A., et al. 2017, in Highlights on Spanish Astrophysics IX, ed. S. Arribas, A. Alonso-Herrero, F. Figueras, C. Hernández-Monteagudo, A. Sánchez-Lavega, & S. Pérez-Hoyos, 99

Rubiño-Martín, J. A., et al. 2012, in Proc. SPIE, Vol. 8444, Ground-based and Airborne Telescopes IV, 84442Y

Rubiño-Martin, J., Rebolo, R., & Mediavilla, E. 2009, The Cosmic Microwave Background: From Quantum Fluctuations to the Present Universe, Canary Islands Winter School of Astrophysics (Cambridge University Press)

Schlegel, D. J., Finkbeiner, D. P., & Davis, M. 1998a, ApJ, 500, 525

Schlegel, D. J., Finkbeiner, D. P., & Davis, M. 1998b, ApJ, 500, 525

Shimabukuro, F. I., & Stacey, J. M. 1968, ApJ, 152, 777

Su, M., Slatyer, T. R., & Finkbeiner, D. P. 2010, ApJ, 724, 1044

Sun, X. H., Han, J. L., Reich, W., Reich, P., Shi, W. B., Wielebinski, R., & Fürst, E. 2007, A&A, 463, 993

The Polarbear Collaboration: P. A. R. Ade, et al. 2014, ApJ, 794, 171

Tramonte, D. 2013, Master's thesis, Università degli Studi di Padova

Trujillo-Bueno, J., Moreno-Insertis, F., & Sanchez Martinez, F. 2002, Astrophysical Spectropolarimetry 368

Tucci, M., Martínez-González, E., Toffolatti, L., González-Nuevo, J., & De Zotti, G. 2004, MNRAS, 349, 1267

Tucci, M., & Toffolatti, L. 2012, Advances in Astronomy, 2012, 624987

Turtle, A. J., Pugh, J. F., Kenderdine, S., & Pauliny-Toth, I. I. K. 1962, MNRAS, 124, 297

Vignaga, R. 2012, Master's thesis, Università degli Studi di Padova

Wallace, P. T. 2008, in Proc. SPIE, Vol. 7019, Advanced Software and Control for Astronomy II, 701908

Watson, R. A., Rebolo, R., Rubiño-Martín, J. A., Hildebrandt, S., Gutiérrez, C. M., Fernández-Cerezo, S., Hoyland, R. J., & Battistelli, E. S. 2005, ApJL, 624, L89

Weiland, J. L., et al. 2011, ApJS, 192, 19

Westerhout, G. 1958, Bulletin Astronomical Institute of the Netherlands, 14, 215

Wu, S.-W., Bik, A., Henning, T., Pasquali, A., Brandner, W., & Stolte, A. 2014, A&A, 568, L13

Yang, R.-z., Aharonian, F., & Crocker, R. 2014, A&A, 567, A19

Zaldarriaga, M., & Seljak, U. 1997, Phys. Rev. D, 55, 1830

Zhang, M. F., Tian, W. W., Leahy, D. A., Zhu, H., Cui, X. H., & Shan, S. S. 2017, The Astrophysical Journal, 849, 147